Doctoral Dissertation

A Study on Broadband Transitions of Waveguide and Planar-Line in Multi-layer Substrate at Sub-Terahertz Band

(サブテラヘルツ帯における多層基板内平面線路と導波管の広帯域変換器に関する研究)

CHATCHAI CHOKCHAI

Department of Electrical and Mechanical Engineering

Nagoya Institute of Technology

Supervisor: PROF. KUNIO SAKAKIBARA

Abstract

Recent advancements in millimeter wave (mmWave) and terahertz wave (THz wave) technologies have garnered significant interest due to their wide bandwidth, high transmission quality, and potential for enhancing wireless communications. However, challenges such as signal attenuation, obstruction by obstacles, and limited coverage due to short wavelengths persist. To address these limitations, a terahertz (THz) wireless link operating at 300 GHz has been proposed to provide short-range, high-speed wireless services. Significant strides have also been made in THz detection, imaging, and localization applications. Additionally, the application of fifth-generation (5G) technology in robotic surgery and cancer treatment has been explored, along with the use of THz-wave-based sensing technology in the biomedical field. Moreover, advancements in millimeter wave band technology for sixth-generation (6G) communications have enabled data rates of up to 100 Gbps. To meet the growing demand for higher data transmission speeds, developments in interfaces for connection and signal modulation techniques have been pursued. Various antennas and radio frequency (RF) circuits are being developed in the sub-terahertz band, yet the insertion loss of connecting transmission lines remains a serious issue. Therefore, integrating antennas within the dielectric substrate on which the RF chips are mounted is advantageous. Multilayer substrates are generally used to mount IC chips, allowing space for a large number of signal lines, control lines, and power supply lines.

System-in-package (SiP) technology, which integrates all electronic components into a single package, is experiencing rapid growth to meet the demand for cost-effective and compact radio frequency (RF) modules. Similarly, antenna-in-package (AiP) technology, which integrates antennas and RF transceivers, offers advantages such as reduced delay, high speed, miniaturization, and cost-effectiveness. AiP exhibits significant potential in millimeter-wave bands due to their short wavelengths. The interconnection aspect of the antenna-in-package is critical in influencing RF circuit performance. Proposed approaches, including transitions implemented within packages, have the potential to achieve wide bandwidths, particularly in multi-layer substrate packages. Various functions can be provided to the antennas with the feeding circuits. By applying a beam-forming circuit to the antenna, multi-beam, and beam-scanning functions can be performed. It is effective to locate the feeding circuit on the back of the antenna to realize a compact RF module. Various circuits connecting the transmission lines in different layers have been developed. A microstrip line (MSL) is

popular for composing array antennas, and design techniques for various microstrip array antennas have already been established. However, a microstrip line is typically located on the top plane of the multi-layer substrate due to its open structure. A substrate-integrated waveguide (SIW) has become popular as a replacement for a solid waveguide in a substrate. An SIW is generally a low-loss transmission line and can be formed in any layer of the multi-layer substrate due to its closed structure, in contrast to the MSL. An SIW is useful for feeding circuits on the back of microstrip antennas. Transitions play a pivotal role in various applications. Planar microstrip-to-waveguide transitions are commonly employed in waveguide connections between integrated circuits (ICs) and horns and in the measurement of transmission lines without the need for probe stations.

This study presents a broadband planar-line-to-waveguide transition in multi-layer dielectric substrates within the terahertz-wave band. The design technique focuses on wideband and low-loss transitions in the sub-terahertz band, providing a comprehensive solution for addressing feeding circuits from IC chips to array antennas. Three main objectives were identified and developed: broad-wall-inserted planar-line-to-waveguide transitions (including single-end and differential-line-to-waveguide transitions), narrow-wall-inserted planar-line-to-waveguide transitions, and SIW-to-SIW transitions in multi-layer substrates. The proposed transitions feature eight copper patterns with a conductivity (σ) of 5.8×10^7 S/m, and a copper plate thickness of 15 μm with a variation of less than ± 7 μm. A seven-layer dielectric substrate, HL972LF-LD (Mitsubishi Gas Chemical Company, Inc.), with a dielectric constant (ε_r) of 3.5 and a loss tangent ($\tan \delta$) of 0.003, was used. Three prepreg layers with copper were placed on both sides of the center core layer, forming seven dielectric layers. The thicknesses of the core and prepreg substrates were 100 μm and 30 μm, respectively. The thickness variation of the core layer is less than ± 15 μm, and the variations of the prepreg layers are less than ± 10 μm.

The broad-wall-inserted planar-line-to-waveguide transition is crucial for linking planar transmission lines to waveguides, optimizing power transmission, and minimizing loss. These transitions, designed for both differential and single-ended lines, mitigate loss and achieve wideband performance. While single-ended transitions use grounded suspended coplanar waveguide (GSCPW) and grounded coplanar waveguide (GCPW), and differential transitions use GCPW. These transitions are analyzed through electromagnetic simulations and validated experimentally within the WR-3 band (220 GHz-320 GHz). Corrugation structures are introduced to extend the bandwidth of GSCPW-to-waveguide transitions in a multi-layer dielectric substrate, enhancing transmission characteristics. The proposed transition achieves

bandwidths of S_{11} below −10 dB and S_{21} higher than −3 dB, measuring 58.9 GHz and 52.8 GHz, respectively, with corrugations increasing bandwidth by up to 12.2%. Additionally, a GCPW-to-waveguide transition covering the 250-290 GHz band uses a GCPW line and double rectangular stacked patch, achieving a bandwidth of S_{11} below −10 dB of 49.0 GHz. A broadband waveguide-to-differential-line transition with a triple-stacked patch is proposed for the 300 GHz band, involving differential signal lines, and optimized via hole arrangements to prevent electric field leakage and enhance transmission. The measured result shows a bandwidth of S_{11} below −10 dB exceeding 100 GHz and bandwidths of S_{21} higher than −3 dB, measuring 63 GHz.

The narrow-wall-inserted planar-line-to-waveguide transition is crucial for compact transitions, enabling direct connections to waveguide-fed antennas placed closer than $\lambda/2$ apart. This design is ideal for closely arranged waveguides in an array or multi-beam antennas linked to a 2D beam-scanning system. When the microstrip line is positioned on the narrow wall, the probe becomes orthogonal to the E-plane, resulting in limited coupling. To address limited coupling, a modified V-shaped patch replaces the rectangular patch. A broadband tapered GCPW-to-waveguide transition was designed for the 270 GHz band within multi-layer substrates, meticulously crafted to meet the fabrication constraints of the metal pattern and via-hole arrangement specific to the sub-terahertz band. The broadband operation was achieved through a combination of stacked patches and multiple resonance techniques within the cavity. Excitation of the modified V-shaped patch was realized through a tapered GCPW feed line inserted from the narrow wall of the waveguide, transforming the mode from a single-end line to a waveguide and fostering strong coupling between the signal line and the radiating patch. Simulation results indicated a bandwidth of reflections below –10 dB measuring 63.25 GHz (22.7%). The measured bandwidth of reflections below –10 dB extended to 71.50 GHz (26.1%), with an insertion loss of 2.5 dB at the design frequency of 270 GHz. Furthermore, the measured result shows a bandwidth of transmission coefficient higher than −3 dB, measuring 48.60 GHz.

In addition, Substrate integrated waveguide (SIW) is a promising choice for developing millimeter and terahertz wave circuits and components due to its low loss, easy fabrication, cost-effectiveness, and design versatility. It accommodates active and nonlinear elements like surface-mounted MMICs, broadening its applications. However, integrating SIW with structurally different components can cause loss and mismatches, making transitions crucial for achieving impedance and field matching between SIW and planar circuits. In this context, a broadband transition has been developed to connect two SIWs formed in different layers of a multi-layer substrate, facilitating the connection between an SIW-fed Rotman lens and an

SIW slot array antenna at the 270 GHz band. The transition design was constrained by the fabrication limitations of the metal pattern and via-hole arrangement in the sub-terahertz frequency band. Broadband operation was achieved by combining techniques such as coupled patches, aperture coupling, and a back-short structure. Performance evaluations of the transition were conducted through both simulations and measurements, utilizing waveguide measurements for evaluation. Simulations of the multi-layer SIW-to-SIW transition showed a reflection coefficient bandwidth of less than −10 dB at 73.8 GHz, with a transmission loss of 0.7 dB at the center frequency of 270 GHz. A WG-to-SIW-to-SIW transition with a back-to-back configuration was designed, fabricated, and measured in the sub-terahertz band. The measured results transmission coefficient for a single multi-layer WG-to-SIW-to-SIW transition was −1.8 dB at 270 GHz. Furthermore, the measured result shows a bandwidth of transmission coefficient higher than −3 dB, measuring 57.4 GHz. The measured results revealed a reflection coefficient bandwidth below −10 dB of 64.0 GHz (22.8%), spanning from 248.0 GHz to 312.0 GHz.

This dissertation comprises six chapters. Chapter 1 describes the background and motivation of the study, while Chapter 2 explains the basic theories behind transmission lines and transitions. Chapter 3 presents a broadband broad-wall-inserted planar-line-to-waveguide transition designed for sub-terahertz frequencies within multi-layer substrates. Chapter 4 introduces a broadband tapered GCPW-to-waveguide transition designed for the 270 GHz band within multi-layer substrates. Chapter 5 discusses a broadband transition between two SIWs formed in different layers of a multi-layer substrate at the 270 GHz band. The performances and contributions of the proposed transitions and techniques are concluded in Chapter 6.

Table of Contents

Abstract i

Table of Contents v

List of Figure viii

List of Table xvi

Chapter 1 Introduction 1

1.1 Research Background 1

1.2 Motivation 7

1.3 Scope and Objectives 9

1.4 Dissertation Structure and Contributions 10

References 13

Chapter 2 Theories of Transmission Line and Transition 15

2.1 Transmission Lines 15

2.1.1 Rectangular Waveguide 15

2.1.2 Microstrip Line 21

2.1.3 Coplanar Waveguide 24

2.1.4 Grounded Coplanar Waveguide 27

2.1.5 Grounded Suspended Coplanar Waveguide 30

2.1.6 Coupling Strip Line 32

2.1.7 Differential Line 35

2.1.8 Substrate Integrated Waveguide 36

2.2 Corrugation Waveguide and Corrugation Structure 43

2.2.1 The Corrugation Structure 46

2.3 Microstrip-to-Waveguide Transition 50

2.3.1 Probe Transition with Back-Short 50

2.3.2 Planar Proximity Coupling Transition 52
2.3.3 Coplanar Waveguide-to-Rectangular Waveguide Transition 54
2.3.4 Narrow-Wall Connected Microstrip-to-Waveguide Transition 56
2.4 Substrate Integrated Waveguide-to-Waveguide Transition 60
References 64
Chapter 3 Broad-Wall-Inserted Planar-Line-to-Waveguide Transition in Multi-layer Substrates 67
3.1 GSCPW-to-Waveguide Transition in Multi-layer Substrates 67
3.1.1 Configuration of the GSCPW-to-Waveguide Transition 67
3.1.2 Study Parameters of the GSCPW-to-Waveguide Transition 69
3.2 GCPW-to-Waveguide Transition in Multi-layer Substrates 74
3.2.1 Configuration of the GCPW-to-Waveguide transition 74
3.2.2 Study Parameters of the GCPW-to-Waveguide Transition 77
3.3 Waveguide-to-Differential-Line Transition in Multi-layer Substrates 82
3.3.1 Configuration of the Waveguide-to-Differential-Line Transition 82
3.3.2 Parametric Analysis of the Waveguide-to-Differential-Line Transition 88
3.4 Experimental Performances 96
3.4.1 Fabrication and Measurement Setup 96
3.4.2 Measurement Results of the GSCPW-to-Waveguide Transition 98
3.4.3 Measurement Results of the GCPW-to-Waveguide Transition 99
3.4.4 Measurement Results of the Waveguide-to-Differential-Line Transition 102
3.5 Summary 107
References 108
Chapter 4 Narrow-Wall-Inserted Planar-Line-to-Waveguide Transition in Multi-layer Substrates 111
4.1 Configuration of the Narrow-Wall-Inserted planar-line-to-Waveguide Transition 111
4.2 Simulation Results and Discussion 118

4.3 Experimental Performances 124
4.4 Summary 130
References 131
Chapter 5 SIW-to-SIW Transition in Multi-layer Substrates 134
5.1 SIW-to-SIW Transition 134
5.1.1 Configuration of SIW-to-SIW Transition 134
5.1.2 Study Parameters of SIW-to-SIW Transition 137
5.2 Structure Design for Waveguide Measurement 142
5.2.1 WG-to-SIW Transition 142
5.2.2 WG-to-SIW-to-SIW Transition 144
5.2.3 Back-to-Back Transition 145
5.3 Fabrication and Experimental Performances 146
5.3.1 Fabrication 146
5.3.2 Measurement 148
5.4 Summary 152
References 153
Chapter 6 Conclusion and Contribution 155
Acknowledgment 158
Publication List 159

List of Figure

Figure 1.1 Millimeter wave in the spectrum band 2

Figure 1.2 Future expectation applications for the 300 GHz frequency band 3

Figure 1.3 Variation of array antennas suitable for millimeter-wave and sub-terahertz band 4

Figure 1.4 Several application scenarios for beam-scanning antennas 5

Figure 1.5 Schematic view of a typical planar phased array antenna with circuit and feeding network for beam-scanning 6

Figure 1.6 Organizations of the dissertations 10

Figure 2.1 Rectangular waveguide. 17

Figure 2.2 Field lines for the lowest order TE mode (TE_{10}) 21

Figure 2.3 Microstrip line. 22

Figure 2.4 Equivalent geometry of quasi-TEM microstrip line, where the dielectric substrate has been replaced with a homogeneous medium of effective relative permittivity, ε_e 23

Figure 2.5 Coplanar waveguide (CPW) 24

Figure 2.6 Various CPW structures 26

Figure 2.7 Grounded coplanar waveguide configuration. 28

Figure 2.8 Ideal suspended coplanar waveguide structure. 31

Figure 2.9 Schematic diagram of the transformation steps for solving C_1. 31

Figure 2.10 Strip line cross-section 32

Figure 2.11 Fringe capacitance at the corners of the strip in a stripline transmission line. .. 33

Figure 2.12 Even and odd modes in coupled strip lines 34

Figure 2.13 Types of coupled strip lines 35

Figure 2.14 A perspective view of a conventional DL 36

Figure 2.15 Perspective views of the balanced lines. 36

Figure 2.16 Evolution of SIW structure 38

Figure 2.17 The TE_{10} mode surface current distribution of a conventional rectangular waveguide with metallic holes on the thin side walls 38

Figure 2.18 Physical structure of the substrate-integrated waveguide transmission line 39

Figure 2.19 Substrate-integrated waveguide fundamental design parameters 40

Figure 2.20 Cross section of the different versions of the compact SIW structures: (a) substrate-integrated folded waveguide; (b) half-mode substrate-integrated waveguide; (c) substrate-integrated ridge waveguide; (d) substrate-integrated slab waveguide 41

Figure 2.21 Some popular transitions between planar transmission line and substrate-integrated waveguide 42

Figure 2.22 Schematic drawing of the corrugation waveguide 45

Figure 2.23 Equivalent LC parallel circuit of the corrugation structure 47

Figure 2.24 The configuration of the corrugation structure 49

Figure 2.25 Probe transition with back-short 50

Figure 2.26 Detailed configuration of probe transition with back-short 51

Figure 2.27 Magnetic and electric field lines 51

Figure 2.28 Planar proximity coupling transition 53

Figure 2.29 Detailed configuration of planar proximity coupling transition 53

Figure 2.30 Electric field lines of each mode in planar proximity coupling transition 54

Figure 2.31 Overall picture of the new CPW-to-rectangular waveguide transition 55

Figure 2.32 Cross-sectional views of the new CPW-to-rectangular waveguide Transition . 55

Figure 2.33 Modes of the CPW (a) CPW mode (b) CSL mode 56

Figure 2.34 Configuration of transition 57

Figure 2.35 Detail Configuration of transition 58

Figure 2.36 Current distributions on patch element 59

Figure 2.37 The transition between rectangular waveguide and SIW. 61

Figure 2.38 E-plane SIW in multilayer substrate configuration 62

Figure 2.39 Electric field distributions in E-plane SIW 62

Figure 2.40 Leakage loss in E-plane SIW 63

Figure 3.1 Configuration of the GSCPW-to-waveguide transition (a) 3D overview and (b) Top views of each layer with the parameters 68

Figure 3.2 Simulation results of scattering parameters of the GSCPW-to-waveguide transition 68

Figure 3.3 Configuration of the GSCPW-to-waveguide transition with corrugation structures (a) 3D overview and (b) Top views of each layer with the parameters 69

Figure 3.4 Reflection characteristics of the GSCPW-to-waveguide transition with corrugation structures depend on d_1 (a) reflection coefficient and (b) transmission coefficient 70

Figure 3.5 The electric field of the transition (a) without corrugation at 275 GHz, (b) without corrugation at 285.2 GHz and (c) with corrugation at 285.2 GHz 71

Figure 3.6 Reflection characteristics of the GSCPW-to-waveguide transition with corrugation structures depending on L_P 72

Figure 3.7 Reflection characteristics of the GSCPW-to-waveguide transition with corrugation structures depending on W_P 72

Figure 3.8 Simulation results of the transition with and without corrugation structures ... 73

Figure 3.9 Configuration of the GCPW-to-waveguide transition (a) 3D overview and (b) Top views of each layer with the parameters 75

Figure 3.10 Scattering parameters of the GCPW-to-waveguide transition without corrugation structure 75

Figure 3.11 Configuration of the GCPW-to-waveguide transition with corrugation structure (a) 3D overview, (b) Transmission mode, and (c) Top views and geometrical parameters on layer n (n = 1, 2, …, 8) 76

Figure 3.12 Scattering parameters of the GCPW-to-waveguide transition with corrugation structures depending on d_1 (a) reflection coefficient (b) transmission coefficient 77

Figure 3.13 Scattering parameters of the GCPW-to-waveguide transition with corrugation structures depending on d_2 (a) reflection coefficient (b) transmission coefficient 78

Figure 3.14 Simulated electric field of the transition on the XZ-plane and YZ-plane of the waveguide center at 282.8 GHz (a) $d_2 = 0$ μm, (b) $d_2 = 40$ μm 79

Figure 3.15 Reflection characteristics of the GCPW-to-waveguide transition with corrugation structures depending on L_{P1} 80

Figure 3.16 Reflection characteristics of the GCPW-to-waveguide transition with corrugation structures depending on L_{P2} 80

Figure 3.17 Comparison of simulated reflection and transmission coefficients of the GCPW-to-waveguide transitions 81

Figure 3.18 Configuration of the waveguide-to-differential-line transition 83

Figure 3.19 Top views of each layer with the parameters for the waveguide-to-differential-line transition 84

Figure 3.20 Cross-sectional view with transmission mode of the waveguide-to-differential-line transition 85

Figure 3.21 Simulated electric field distribution on the metal layer n (n = 1, 2, …, 8) of the waveguide-to-differential-line transition at 250 GHz. 86

Figure 3.22 Via-hole arrangement (a) with center via-hole L1–L8 (b) with two via-holes L2–L8 87

Figure 3.23 Reflection characteristics of the waveguide-to-differential-line transition with center via-hole L1–L8 depending on R_{P2} 88

Figure 3.24 Reflection characteristics of the waveguide-to-differential-line transition with center via-hole L1–L8 depending on R_{P4} 89

Figure 3.25 Reflection characteristics of the waveguide-to-differential-line transition with center via-hole L1–L8 depending on R_{P5} 89

Figure 3.26 Reflection characteristics of the waveguide-to-differential-line transition with center via-hole L1–L8 depending on R_{L2} 90

Figure 3.27 Reflection characteristics of the waveguide-to-differential-line transition with center via-hole L1–L8 depending on R_{L4} 91

Figure 3.28 Reflection characteristics of the waveguide-to-differential-line transition with center via-hole L1–L8 depending on R_{L5} 91

Figure 3.29 Reflection characteristics of the waveguide-to-differential-line transition with center via-hole L1–L8 depending on R_{L7} 92

Figure 3.30 Comparison of the scattering characteristics of transition with center via-hole L1-L8 and with two via-holes L2-L8 92

Figure 3.31 Simulated electric field distribution of the proposed transition at 305 GHz (a) Electric field distribution on the YZ-plane of the waveguide center (b) Electric field distribution of the transition from L5–L8 of the multi-layer substrates with center via-hole L1–L8 (c) Electric field distribution of the transition from L5–L8 of the multi-layer substrates with two via-holes L2–L8 93

Figure 3.32 Experimental setup of the broad-wall-inserted planar-line-to-waveguide (a) top view (b) side view 97

Figure 3.33 Fabricated the GSCPW-to-waveguide transition (DUT) with various lengths of the transmission line and an enlarged view 99

Figure 3.34 Simulated and measured scattering parameter results of the GSCPW-to-waveguide transition 99

Figure 3.35 Fabricated the GCPW-to-waveguide transition (DUT) with various lengths of the transmission line and an enlarged view 101

Figure 3.36 Simulated and measured scattering parameter results of the GCPW-to-waveguide transition 101

Figure 3.37 Fabricated DUT for different lengths of the transmission line and an enlarged view of the waveguide-to-differential-line transition (left) 102

Figure 3.38 Measured transmission of the fabricated waveguide-to-differential-line transition with four different line lengths 103

Figure 3.39 Transmission characteristics at each correction process of the waveguide-to-differential-line transition 103

Figure 3.40 Simulated and measured scattering parameter results of the waveguide-to-differential-line transition 104

Figure 4.1 Configuration of the narrow-wall-inserted planar-line-to-waveguide transition 112

Figure 4.2 Cross-sectional view and mode transformation of the transition 113

Figure 4.3 Current distribution on the modified V-shaped patch and tapered GCPW 114

Figure 4.4 Top views of each layer with the parameters for the narrow-wall-inserted planar-line-to-waveguide transition 115

Figure 4.5 Simulated current vector distribution on the GCPW feed line and modified V-shaped patch at 275 GHz 116

Figure 4.6 Simulated electric field distribution on Layer 1 to Layer 4 of the transition at 275 GHz 117

Figure 4.7 Comparison of reflection characteristics of the transition with and without tapered GCPW 118

Figure 4.8 Reflection characteristics of the narrow-wall-inserted planar-line-to-waveguide transition depending on L 119

Figure 4.9 Reflection characteristics of the narrow-wall-inserted planar-line-to-waveguide transition depending on W 119

Figure 4.10 Reflection characteristics of the narrow-wall-inserted planar-line-to-waveguide transition depending on ρ 120

Figure 4.11 Reflection characteristics of the narrow-wall-inserted planar-line-to-waveguide transition depending on θ 120

Figure 4.12 Reflection characteristics of the narrow-wall-inserted planar-line-to-waveguide transition depending on W_{p3} 121

Figure 4.13 Reflection characteristics of the narrow-wall-inserted planar-line-to-waveguide transition depending on W_{p4} 122

Figure 4.14 Experimental setup of the narrow-wall-inserted planar-line-to-waveguide transition with the waveguide jig in the WR-3 band 124

Figure 4.15 Fabricated substrates (DUT) for different lengths of the transmission line 125

Figure 4.16 Measured transmission coefficients of the fabricated transition with four different line lengths..... 126

Figure 4.17 Loss and transmission characteristics at each correction process of the fabricated transition..... 126

Figure 4.18 Measured and simulated reflection and transmission coefficients of the narrow-wall-inserted planar-line-to-waveguide transition 127

Figure 5.1 The geometry of the SIW-to-SIW Transition..... 135

Figure 5.2 Cross-sectional view (a) mode transformation of the transition (b) simulated electric field distribution of the transition on the *xz*-plane at 270 GHz. 135

Figure 5.3 Top views of each layer with the parameters for the SIW-to-SIW transition... 137

Figure 5.4 Reflection characteristics of the SIW-to-SIW transition depending on L_P 138

Figure 5.5 Reflection characteristics of the SIW-to-SIW transition depending on D_{L5} 138

Figure 5.6 Reflection characteristics of the SIW-to-SIW transition depending on D_{L2} 139

Figure 5.7 Reflection characteristics of the SIW-to-SIW transition depending on L_{S4} 139

Figure 5.8 Configuration of the WG-to-SIW transition (a) 3D overview and (b) Top views of each layer with the parameters 143

Figure 5.9 Comparison simulation results of each transition..... 143

Figure 5.10 Configuration of the WG-to-SIW-to-SIW transition (a) 3D overview, (b) Cross-sectional view, and (c) Top views of each layer with the parameters 145

Figure 5.11 Configuration of the back-to-back transition in cross-sectional view..... 145

Figure 5.12 Fabricated DUTs for different lengths of the SIW and an enlarged view 147

Figure 5.13 Fabricated jig and an enlarged view of the jig..... 147

Figure 5.14 Experimental setup of the proposed transition with the waveguide jig in the WR-3 band (220–330 GHz)..... 148

Figure 5.15 Measured transmission coefficients of the DUTs with four different SIW length . 149

Figure 5.16 Loss and transmission characteristics at each correction process of the fabricated transition 149

Figure 5.17 Measured and simulated reflection and transmission coefficients of the WG-to-SIW-to-SIW transition. 150

List of Table

Table 3.1 Optimized Parameters of the waveguide-to-differential-line transition 95

Table 3.2 Fabrication accuracies of the multi-layer substrates. 97

Table 3.3 Comparison of waveguide-to-microstrip transition 106

Table 4.1 Optimized parameters of the narrow-wall-inserted planar-line-to-waveguide transition 123

Table 4.2 Comparison of the planar-line-to-waveguide transition 129

Table 5.1 Optimized parameters of the SIW-to-SIW transition 140

Table 5.2 Comparison of the SIW-to-SIW transition 141

Table 5.3 Optimized parameters of the WG-to-SIW transition 144

Table 5.4 Fabrication accuracies of the multi-layer substrate 146

Chapter 1

Introduction

1.1 Research Background

In contemporary society, wireless communication systems play a pivotal role in people's daily lives, with their prevalence steadily increasing annually owing to their user-friendly convenience. These systems facilitate various functions such as video communication, access to entertainment media, security, and healthcare services. However, the escalating demands for data transmission speed and quality necessitate continual advancements in communication technology. Consequently, each decade witnesses the emergence of new communication technologies that offer enhanced services. Notably, the data rates of wireless communications have undergone a remarkable surge, with reported maximum rates exceeding 100 Gb/s. This trajectory suggests that wireless communication data rates are poised to rival those of wired communications in the near future. A significant catalyst for this rapid increase is the expansion of available frequency bands, achieved through the utilization of higher carrier frequencies. Consequently, developing higher frequencies is paramount in enhancing data rates. Nevertheless, this expansion introduces a slew of new design challenges and constraints for system designers. In particular, as frequency increases, component sizes decrease, enabling more compact systems and streamlined integration. However, this presents a formidable challenge in contemporary communication environments characterized by the imperative for higher data rates, accommodating numerous concurrent users, and ensuring low latency. These challenges are particularly pronounced in applications necessitating real-time data transmission.

The introduction of the 5th generation (5G) marks a significant advancement in communication network systems. Anticipated as a pivotal upgrade, 5G networks are poised to deliver superior evolutionary services, leveraging existing systems and technologies to achieve optimal performance compared to their predecessors. The Federal Communication Commission (FCC) has allocated frequency bands for 5G within the millimeter-wave range, specifically ranging from 24 GHz to 47 GHz. This allocation aims to harness the high-frequency spectrum to enhance bandwidth, capacity, and reliability in wireless broadband services, thereby augmenting current telecommunications infrastructure. While the full realization of 5G's potential will unfold over several years, its overarching objective is to address

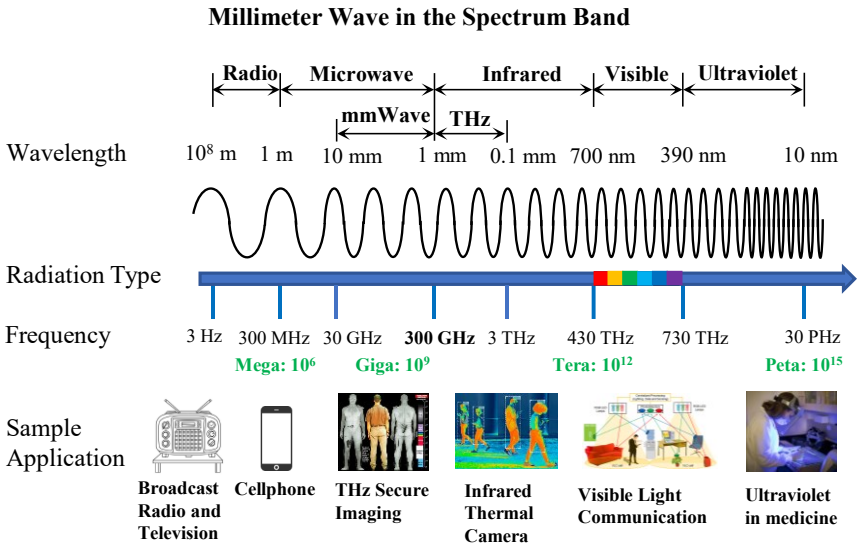

Figure 1.1 Millimeter wave in the spectrum band.

the escalating demands for information and communication services. These demands encompass accommodating a burgeoning array of internet-connected devices, facilitating ultra-low latency critical for near-real-time communications, and delivering accelerated speeds to support emerging technologies. Consequently, wireless communication systems are confronted with mounting requisites for heightened data rates and concurrent user capacities. In light of its expansive data capacity and minimal latency, recent efforts have commenced to explore prospective solutions extending beyond 5G, encompassing both 5th-generation mobile communications (6G). These endeavors are particularly geared towards addressing the imperative for short-range, high-speed data transmission in wireless communication contexts. Consequently, the demand for millimeter waves (mm waves) and terahertz waves (THz waves) is rapidly escalating, driven by the burgeoning need for high-definition (HD) digital video and associated multimedia entertainment services.

The standard IEEE designation encompasses the frequency band, including the millimeter wave within the spectrum ranging from 30 GHz to 300 GHz, as depicted in Fig. 1.1. In response to the evolving demands in communication technologies, there has been a pronounced surge in interest in millimeter-wave (mm-wave) and terahertz-wave (THz-wave) based wireless communication and sensing technologies. Mm-wave and THz radiation are characterized by wavelengths falling within the range of 3 mm to 30 μm [1]. This spectral region occupies the space between microwaves and infrared frequencies, spanning from 30 GHz to 3 THz, and is anticipated to be fully realized by the year 2030.

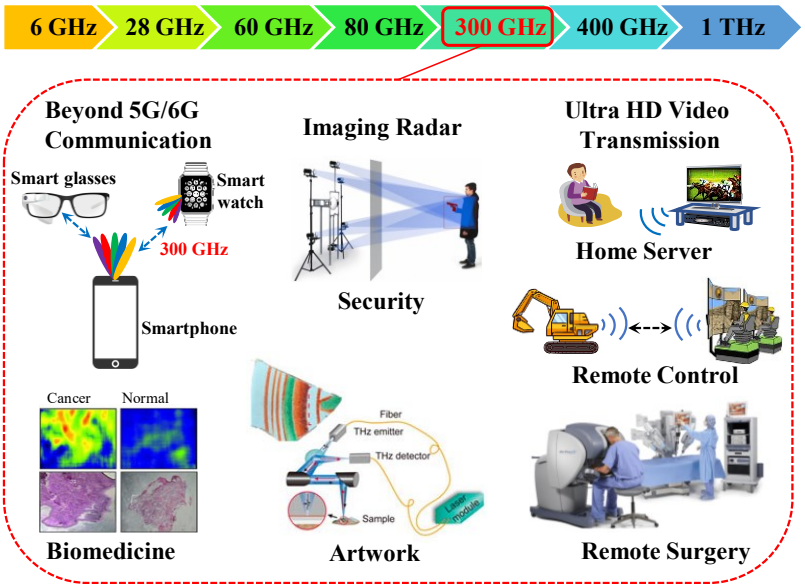

Figure 1.2 Future expectation applications for the 300 GHz frequency band.

Recent advancements in millimeter wave (mmWave) and terahertz wave (THz wave) technologies have garnered significant attention owing to their broad bandwidth and potential for enhancing wireless communications with high data transmission quality. Fig. 1.2 illustrates anticipated future applications in the terahertz and 300 GHz bands. THz radiation exhibits numerous properties that render it promising for applications in biomedicine [2]. Moreover, exploration into the utilization of fifth-generation (5G) technology in areas such as robotic surgery and cancer treatment has been undertaken [3], along with the investigation of THz-wave-based sensing technologies in the biomedical domain [4]. These technologies also hold promise for delivering high-definition (HD) digital video and related multimedia entertainment services [5], as well as facilitating remote machine control [6]. Furthermore, significant progress has been achieved in THz detection, security inspection, and imaging [7]-[10]. Advancements in millimeter wave band technology for sixth-generation (6G) communications have facilitated data rates of up to 100 Gbps [11]. Concurrently, the development of ultrafast optoelectronics and low-scale semiconductor technology has propelled rapid advancements in terahertz spectroscopy, garnering increasing attention for related research and applications.

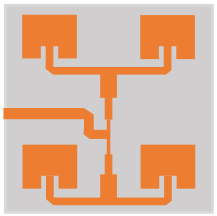

Microstrip patch antenna array

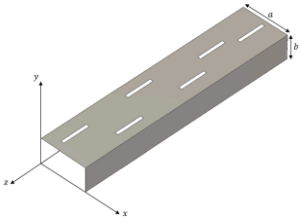

Slot waveguide antenna

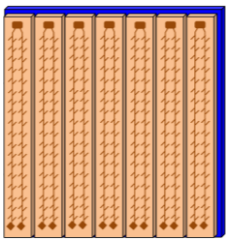

Microstrip comb-line antenna [13]

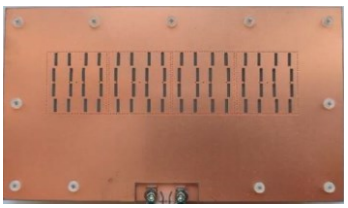

Planar slotted SIW cavity antenna array [14]

Figure 1.3 Variation of array antennas suitable for millimeter-wave and sub-terahertz band.

Given their short wavelengths falling within the range of 0.1 mm to 10 mm, both mm-wave and THz wave technologies offer the advantage of miniaturization in antenna and circuit design, dictated by the wavelength ratio. Consequently, antenna designs for mm-wave and THz waves exhibit directional properties even at such diminutive wavelengths. However, it is noteworthy that both mm waves and THz waves are subject to significant free-space propagation loss (FSPL) and atmospheric attenuation [12], necessitating antennas with high gain and efficiency. The frequency range of 300 GHz, spanning from 220 GHz to 320 GHz, presents promising prospects for achieving short-range, high data rates in wireless communications. Accordingly, the development of high-gain antenna technology is anticipated to be closely linked with the terahertz band. Fig. 1.3 showcases various developed antennas tailored for millimeter wave formats, including microstrip patch antenna array, slotted waveguide antennas, Microstrip comb-line antenna [13], and Planar slotted SIW cavity antenna array [14]. Microstrip patch antennas, characterized by their narrow-bandwidth resonance and thin planar structure utilizing printed circuit boards (PCBs), are among the established designs for millimeter wave operation. However, in the terahertz frequency band, the challenge of transmission loss becomes pronounced, impeding the attainment of high gain. Conversely, waveguide slot array antennas, leveraging waveguides for transmission lines, offer reduced transmission loss, rendering them well-suited for achieving high signal reception.

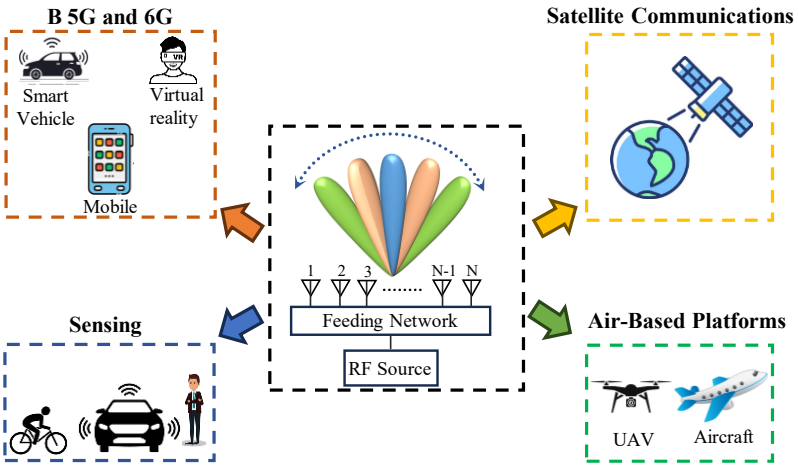

Figure 1.4 Several application scenarios for beam-scanning antennas.

Similarly, the development of circuits tailored for mm-wave and THz wave frequencies is imperative. System-in-package (SiP) technology, which consolidates all electronic components within a single package, has witnessed rapid growth in addressing the escalating demand for cost-effective and compact radio frequency (RF) modules. Likewise, antenna-in-package (AiP) technology, integrating antennas and RF transceivers, offers a range of advantages such as reduced delay, enhanced speed, miniaturization, and cost-effectiveness. AiP holds particular promise in millimeter-wave bands owing to their short wavelengths. The interconnection aspect within antenna-in-package configurations plays a pivotal role in shaping RF circuit performance. Proposed methodologies, including transitions embedded within packages, harbor the potential to achieve wide bandwidths, especially within multi-layer substrate packages. Consequently, the seamless connection between the circuit and the antenna necessitates the utilization of a feeding network and transitions.

Phased array antennas, composed of two or more antenna elements fed coherently with controllable phase shifters to achieve desired pattern performance such as beam scanning and shaping, represent a pivotal technology for modern communications and sensing systems. Endowed with numerous advantages, phased array antennas can attain high gain, low sidelobe levels (SLL), flexible beam scanning, and high tracking accuracy. The versatility of beam-scanning phased array antennas renders them applicable across various domains, as depicted in Fig. 1.4. The evolution Beyond fifth generation (B5G) and sixth generation (6G) communications underscore the significance of phased array antennas in meeting future demands. Moreover, the emergence of highly integrated phased array antennas, capable of global coverage with beam-scanning capabilities, holds great promise in SATCOM,

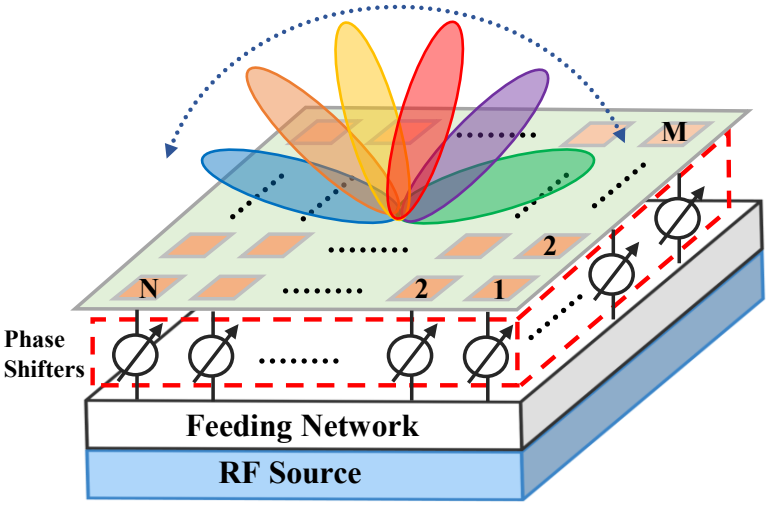

Figure 1.5 Schematic view of a typical planar phased array antenna with circuit and feeding network for beam-scanning.

particularly for medium earth orbit (MEO) and low earth orbit (LEO) SATCOM applications. Another critical application lies in sensing-based automotive radar and anti-collision radar systems. Furthermore, phased array antennas find utility in airborne platforms such as unmanned aerial vehicles (UAVs) and aircraft, facilitating functions like synthetic aperture radar and more [15].

With a diverse array of applications, it becomes imperative to design antennas and network feeders appropriately. A schematic depiction of a typical planar phased array antenna, complete with circuitry and a feeding network for beam scanning, is presented in Fig 1.5. The transitions of transmission lines assume critical importance in connecting planar transmission lines to waveguides, aiming to optimize power transmission while minimizing loss. Effective waveguide transitions from both differential and single-ended lines are indispensable. This entails the inclusion of substrate integrated waveguide (SIW) technology, which boasts low transmission loss tailored to specific applications. Differential lines play a vital role in linking differential circuits with rectangular waveguides, owing to their inherent advantages in mitigating interference. Consequently, the evolution of both single-ended and differential-line-to-waveguide transitions has ensued. Furthermore, advancements have been made in the development of SIW transitions for the feeding network.

1.2 Motivation

As the antenna and its feeding circuit represent pivotal components of the phased array antenna, their transmission performance significantly impacts antenna characteristics such as gain and beam directionality. It is imperative to note that a low loss feeding network plays a crucial role in enhancing the transmission performance of the phased array antenna. Presently, feeding network technologies encounter challenges related to high loss, particularly in millimeter-wave bands. These losses stem from transmission line utilization in circuit implementation and circuit insertion loss. The motivation behind this research lies in developing low-loss and broadband transitions in multi-layer substrates for feeding circuits, aiming to mitigate the limitations inherent in existing systems.

The broad-wall-inserted planar-line-to-waveguide transition is pivotal for linking planar transmission lines to waveguides, aiming to optimize power transmission while minimizing loss. Waveguide transitions from both differential and single-ended lines must be meticulously designed to mitigate loss and achieve wideband performance, tailored to the specific application at hand. Differential lines play a crucial role in connecting differential circuits with rectangular waveguides, capitalizing on their inherent advantages in mitigating interference. Consequently, both single-ended and differential-line-to-waveguide transitions have undergone evolution to cater to the requirements of feeding networks. Commonly utilized transmission lines such as microstrip lines, coplanar waveguides (CPW), and grounded coplanar waveguides (GCPW) are deployed on the top metal planes of multi-layer substrates to establish connections with integrated circuits (ICs). Depending on the circuit configuration of the applications, both differential and single-ended lines can be employed for IC connections.

The narrow-wall-inserted planar-line-to-waveguide transition is crucial for applications requiring multiple compact transitions. This transition involves inserting signal lines through the narrow wall of the waveguide, enabling exceptionally compact transitions. Such a configuration facilitates direct connections to waveguide-fed antennas placed closer than $\lambda/2$ apart. In scenarios where waveguides are arranged closely, as in the case of array antennas or multi-beam antennas, the broad walls are positioned side-by-side. These waveguides are linked to a cylindrical lens and horn array for a 2D beam-scanning system. When the microstrip line is positioned on the narrow wall, the microstrip line probe becomes orthogonal to the E-plane, resulting in limited coupling. To address this limitation, a modified V-shaped patch element has been developed to replace the rectangular patch. The modified V-shaped patch element aligns the current on the signal line orthogonally with the polarization of the TE_{10} mode.

Substrate integrated waveguide (SIW) emerges as a promising choice for developing circuits and components operating within the millimeter and terahertz wave bands. Its benefits encompass low loss, facile fabrication, cost-effectiveness, and design versatility. Furthermore, SIW fabrication technology seamlessly accommodates active and nonlinear elements, such as surface-mounted monolithic microwave integrated circuits (MMICs), thereby significantly broadening its potential applications. Notwithstanding these advantages, integrating SIW with other components exhibiting structural disparities can precipitate challenges related to loss and mismatches. Consequently, transitions assume a critical role in achieving impedance and field matching between SIW and planar circuits. In this context, a broadband transition has been developed to connect two SIWs formed in different layers of a multi-layer substrate, facilitating the connection between an SIW-fed Rotman lens and an SIW slot array antenna.

In the beam-scanning phased array antenna, the connections between the circuit and other components, such as array elements and the IC chip, assume a crucial role in facilitating wideband and low-loss transmission from the IC chip to radiation elements. In millimeter-wave applications, the array elements, feeding network, and IC chip are interconnected through waveguides. However, due to the potential application of various transmission line technologies in the beam-scanning phased array antenna, the development of transition techniques between waveguides and transmission lines becomes critically necessary.

Ultimately, the utilization of low-loss transmission lines in the beamforming network, along with the implementation of wideband transitions, becomes imperative to augment the performance of phased array antennas. This dissertation endeavors to investigate straightforward yet efficient techniques for designing transmission lines, beam-scanning networks, and transitions tailored for multi-beam array antennas operating within the millimeter-wave and sub-terahertz bands.

1.3 Scope and Objectives

This doctoral dissertation, titled "A Study on Broadband Transitions of Waveguide and Planar-Line in Multi-layer Substrate at Sub-Terahertz Band," presents analytical, numerical, and experimental investigations of planar-line-to-waveguide transitions. The study primarily focuses on techniques to achieve broadband and low-loss performance, as well as extensive research aimed at producing wideband transitions for feeding networks in the sub-terahertz band.

The main objectives of this study revolve around developing broadband and low-loss performance planar-line-to-waveguide transitions in multi-layer substrates. There are three objectives in this study:

- The broadband broad-wall-inserted planar-line-to-waveguide transitions in the multi-layer substrate will be designed. Both single-ended and differential-line-to-waveguide transitions have evolved to meet the requirements of feeding networks. In the case of single-ended line-to-waveguide transitions, grounded coplanar waveguides (GCPW) and grounded suspended coplanar waveguides (GSCPW) are utilized as transmission lines. Implementations such as the double patch and corrugation structures are employed to enhance transmission loss and bandwidth. In differential-line-to-waveguide transitions, a triple circular stacked patch configuration is adopted to improve bandwidth.
- A broadband narrow-wall-inserted planar-line-to-waveguide transition within a multi-layer substrate will be developed. Grounded coplanar waveguide (GCPW) serves as the chosen transmission line. Techniques such as implementing the modified V-shaped patch element and the double patch are employed to improve bandwidth. Evolutionary advancements in GCPW-to-waveguide transitions have been made to meet the demands of establishing direct connections to waveguide-fed antennas positioned closer than $\lambda/2$ apart.
- A broadband transition between two substrate integrated waveguides (SIWs) formed in different layers of a multi-layer substrate within the sub-terahertz band will develop. The design of the transition was constrained by fabrication limitations related to metal patterns and via-hole arrangement within the sub-terahertz band. Broadband operation was achieved through a combination of techniques, including coupled patch, aperture coupling, and a back-short structure.

Generally, this dissertation aims to present novel technologies for the development of broadband and low-loss planar-line-to-waveguide transitions in multi-layer substrates within the sub-terahertz band.

1.4 Dissertation Structure and Contribution

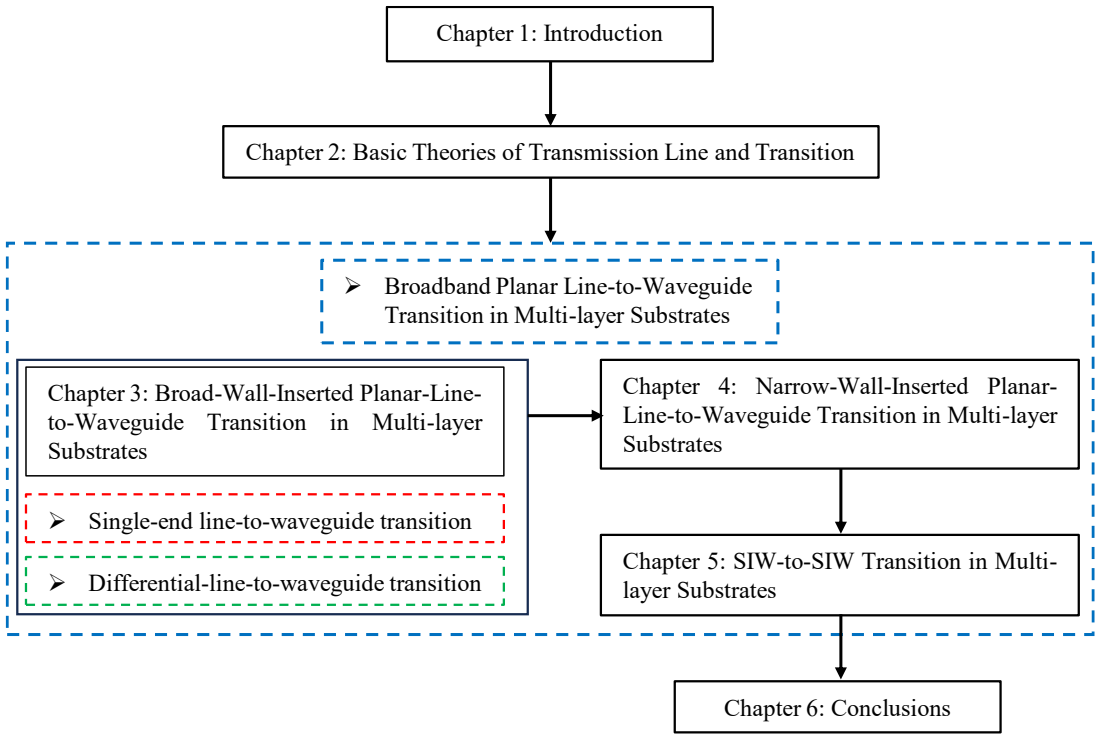

Figure 1.6 Organizations of the dissertations.

Fig 1.6 illustrates the organization of the dissertation, beginning with Chapter 1 which discusses the background, applications, and requirements of transitions for feeding networks in the sub-terahertz band. The discussion further encompasses the research scope and technologies for wideband transitions. Chapter 2 provides background information on transmission lines and conventional transition techniques, including their features and potential state-of-the-art characteristics. This chapter furnishes the foundational knowledge necessary for selecting appropriate technologies to design the transitions presented in Chapters 3, 4, and 5.

Chapter 3 presents a broadband broad-wall-inserted planar-line-to-waveguide transition designed for sub-terahertz frequencies within multi-layer substrates. It encompasses both single-end line-to-waveguide and differential-line-to-waveguide transitions. The single-end

line-to-waveguide transition employs grounded suspended coplanar waveguide (GSCPW) and grounded coplanar waveguide (GCPW) configurations for feeding, while the differential-line-to-waveguide transition utilizes GCPW. In the case of single-ended line-to-waveguide transitions, grounded coplanar waveguides (GCPW) and grounded suspended coplanar waveguides (GSCPW) are utilized as transmission lines. For GCPW-to-waveguide transition, implementations such as the patch and corrugation structures are employed to enhance transmission loss and bandwidth. While GCPW-to-waveguide transition, implementations such as the double patch and corrugation structures are employed to enhance transmission loss and bandwidth. In differential-line-to-waveguide transitions, a triple circular stacked patch configuration is adopted to improve bandwidth. The characteristics of these transitions are analyzed through electromagnetic simulations employing the finite element method and validated through experimental measurements within the WR-3 band (220 GHz-320 GHz). The measured performances substantiate the feasibility of the multi-layer broad-wall-inserted planar-line-to-waveguide transition, indicating its suitability for practical sub-terahertz systems. The contributions from this chapter have been published in two international conferences and a journal paper.

- C. Chokchai, H. A. Diawuo, Y. Sugimoto, K. Sakakibara and N. Kikuma, “Bandwidth Extension of GSCPW-to-Waveguide Transition in Multi-Layer Dielectric Substrate by Corrugation Structures in THz Band,” 2022 International Symposium on Antennas and Propagation (ISAP), Sydney, Australia, 2022, pp. 559-560, doi: 10.1109/ISAP53582.2022.9998582.
- C. Chokchai, Y. Sugimoto, K. Sakakibara and N. Kikuma, “Broadband GCPW-to-Waveguide Transition in Multi-Layer Dielectric Substrate with Double Patch and Corrugation Structures in 275 GHz Band,” 2023 IEEE International Symposium on Antennas And Propagation (ISAP), Kuala Lumpur, Malaysia, 2023, pp. 1-2, doi: 10.1109/ISAP57493.2023.10389096.
- C. Chokchai, Y. Sugimoto, K. Sakakibara, H. A. Diawuo and N. Kikuma, “Broadband Waveguide-to-Differential-Line Transition in Multi-Layer Substrates With Triple Stacked Patch in 300 GHz Band,” in IEEE Access, vol. 12, pp. 49804-49816, 2024, doi: 10.1109/ACCESS.2024.3384606.

Chapter 4 proposed a broadband tapered GCPW-to-waveguide transition for the 270 GHz band in multi-layer substrates. The transition was designed within the fabrication constraints of the metal pattern and via-hole arrangement at the sub-terahertz band. The transition features

a single-ended line placed on the top layer of multi-layer dielectric substrates, with a modified V-shaped patch element located in Layer 2. Rectangular patches 1 and 2 were mounted on layers 3 and 4, respectively. A via-hole arrangement surrounds a tapered grounded coplanar waveguide. Moreover, double lines of via-hole are strategically arranged to prevent leakage of the parallel plate mode within the substrates. Broadband operation is achieved by combining stacked patches and multiple resonance techniques within the cavity. The modified V-shaped and double-stacked rectangular patches facilitate multiple resonances, while the arrangement of apertures and via-holes contributes to cavity formation. Notably, the design effectively addresses fabrication limitations in the sub-terahertz band. This technique has been introduced and contributed to a journal paper.

- C. Chokchai, Y. Sugimoto, K. Sakakibara, M. Yamazaki, H. A. Diawuo and N. Kikuma, “Broadband GCPW-to-Waveguide Transition in Multi-layer Dielectric Substrates with Modified V-shaped and Double Patch in 270 GHz Band,” in IEEE Journal of microwave.

Chapter 5 describes a broadband transition between two SIW formed in different layers of a multi-layer substrate at the 270 GHz band. The transition design was constrained by the fabrication limitations of the metal pattern and via-hole arrangement in the sub-terahertz frequency band. The broadband operation achieved by combining techniques was coupled patch, aperture coupling, and a back-short structure. The proposed transition's principle was investigated through parameter studies conducted via electromagnetic simulations using the finite element method. Performance evaluations of the transition were conducted through both simulations and measurements, with waveguide measurements employed for evaluation. A WG-to-SIW-to-SIW transition with a back-to-back structure was designed, fabricated, and measured. Especially, the design effectively achieves the fabrication constraints in the sub-terahertz band.

Finally, conclusions of the dissertation and contributions of this work are provided in chapter 6.

References

[1] J. True, C. Xi, N. Jessurun, K. Ahi, and N. Asadizanjani, "Review of THz-based semiconductor assurance", *Optical Engineering*, vol. 60, no 6, pp. 060901-1 - 060901-52, 2021. doi:10.1117/1.OE.60.6.060901.

[2] H. Tabata, "Application of Terahertz Wave Technology in the Biomedical Field," *IEEE Trans. Terahertz Sci. Technol*., vol. 5, no. 6, pp. 1146-1153, Nov. 2015.

[3] K. Pandav, A. G. Te, N. Tomer, S. S. Nair, A. K. Tewari, "Leveraging 5G Technology for Robotic Surgery and Cancer Care," *Cancer Rep. (Hoboken)*, vol. 5, no. 8, e1595, Aug. 2022, doi: 10.1002/cnr2.1595.

[4] M. Gezimati, and G. Singh, "Terahertz Imaging and Sensing for Healthcare: Current Status and Future Perspectives," *IEEE Access*, vol. 11, pp. 18590-18619, 2023, doi: 10.1109/ACCESS.2023.3247196.

[5] Y. Takaku, Y. Kaieda, T. Yu, and K. Sakaguchi, "Proof-of-concept of uncompressed 4K video transmission from drone through mmWave," *in Proc. IEEE 17th Annu. Consum. Commun. Netw. Conf. (CCNC)*, 2020, pp. 1–6.

[6] S. Dadhich, U. Bodin, and U. Andersson, "Key challenges in automation of earth-moving machines," Automation in Construction, vol 68, pp. 212-222, 2016, doi: 10.1016/j.autcon.2016.05.009.

[7] R. Appleby and R. N. Anderton, "Millimeter-wave and submillimeter wave imaging for security and surveillance," *Proc. IEEE*, vol. 95, no. 8, pp. 1683–1690, Aug. 2007.

[8] X. Fu, Y. Liu, Q. Chen, Y. Fu, and T. J. Cui, "Applications of Terahertz Spectroscopy in the Detection and Recognition of Substances" *Front. Phys*, vol. 10, pp. 1-16, 2022, doi: 10.3389/fphy.2022.869537.

[9] G. Tzydynzhapov, P. Gusikhin, V. Muravev, A. Dremin, Y. Nefyodov and I. Kukushkin, "New Real-Time Sub-Terahertz Security Body Scanner," *Int. J. Infrared Millimeter Waves*, vol 41, pp. 632–641, 2020, doi: 10.1007/s10762-020-00683-5.

[10] E. Abraham, A. Younus, J.C. Delagnes, and P. Mounaix, "Non-invasive investigation of art paintings by terahertz imaging," Appl Phys A, vol. 100, pp. 585-590, 2010, doi: 10.1007/s00339-010-5642-z.

[11] W. Jiang, B. Han, M. A. Habibi, and H. D. Schotten, "The road towards 6G: A comprehensive survey," IEEE Open J. Commun. Soc., vol. 2, pp. 334–366, 2021.

[12] Milda Tamosiunaite, Stasys Tamosiunas, Mindaugas Zilinskas and Gintaras Valusis, "Atmospheric Attenuation of the Terahertz Wireless Networks," Broadband Communications Networks, Chapter 9, Sep. 2018.

[13] K. Sakakibara, "High-Gain Millimeter-Wave Planar Array Antennas with Traveling-Wave Excitation", *Radar Technology. InTech*, pp. 319-340, Jan. 01, 2010. doi: 10.5772/7186.

[14] W. Ma, W. Cao, C. Wang, S. Shi, and B. Zhang, "Planar High-Gain Millimeter-Wave Slotted SIW Cavity Antenna Array with Low Sidelobe and Grating Lobe Levels," *Int. J. Antennas Propag.*, vol 2022, pp. 1-9, 2022, doi: 10.1155/2022/8431611.

[15] M. Li, S. -L. Chen, Y. Liu and Y. J. Guo, "Wide-Angle Beam Scanning Phased Array Antennas: A Review," *in IEEE Open J. Antennas Propag.*, vol. 4, pp. 695-712, 2023, doi: 10.1109/OJAP.2023.3296636.

Chapter 2

Theories of Transmission Line and Transition

This chapter provides a brief background of feeding technologies including rectangular waveguides, microstrip lines, coplanar waveguides, differential lines, and substrate integrated waveguide (SIW). The explanations in this chapter will cover the overview of transition technology followed by probe transition with back-shot, planar proximity coupling transition, coplanar waveguide-to-rectangular waveguide transition, and narrow-wall connected planar-line-to-waveguide transition. All the previously developed concepts and applications are presented to achieve better performance. This chapter looks to cover the necessary information required to understand the contributions presented in the designs of Chapters 3, 4, and 5.

2.1 Transmission Lines

This section introduces some of the most commonly used transmission lines. Their advantages and disadvantages are discussed. Field distributions and propagation characteristics of different types of transmission lines are introduced by equations and boundary condition.

2.1.1 Rectangular Waveguide

Rectangular waveguides were one of the earliest types of transmission lines used to transport microwave signals and are still used today for many applications. A large variety of components such as couplers, detectors, isolators, attenuators, and slotted lines are commercially available for various standard waveguide bands from 1 GHz to over 220 GHz. Because of the recent trend toward miniaturization and integration, a lot of microwave circuitry is currently fabricated using planar transmission lines, such as microstrip or strip line, rather than waveguide. There is, however, still a need for waveguides in many applications such as high-power systems, millimeter wave systems, and in some precision test applications.

The hollow rectangular waveguide can propagate TM and TE modes, but not TEM waves, since only one conductor is present. TM and TE modes of a rectangular waveguide have cutoff frequencies below which propagation is not possible, similar to the TM and TE modes of the parallel plate guide [1], [2].

The geometry of a rectangular waveguide is shown in Fig. 2.1, where it is assumed that the guide is filled with a material of permittivity $\varepsilon_r$and permeability μ. It is standard convention to have the longest side of the waveguide along the *x*-axis, so that $a > b$.

The TE modes are characterized by fields with $E_z = 0$, while $H_z \neq 0$.

$$H_x = \frac{-j\beta}{k_c^2}\frac{\partial H_z}{\partial x}, \tag{2.1a}$$

$$H_y = \frac{-j\beta}{k_c^2}\frac{\partial H_z}{\partial y}, \tag{2.1b}$$

$$E_x = \frac{-j\omega\mu}{k_c^2}\frac{\partial H_z}{\partial y}, \tag{2.1c}$$

$$E_y = \frac{-j\omega\mu}{k_c^2}\frac{\partial H_z}{\partial x}. \tag{2.1d}$$

In this case, cutoff wavenumber $k_c \neq 0$, and the propagation constant $\beta = \sqrt{k^2 - k_c^2}$ is generally a function of frequency and the geometry of the line or guide. To apply equation (2.1), one must first find Hz from the Helmholtz wave equation,

$$\left(\frac{\partial^2}{\partial x^2} + \frac{\partial^2}{\partial y^2} + \frac{\partial^2}{\partial z^2} + k^2\right) H_z = 0, \tag{2.2}$$

which, since $H_z(x, y, z) = h_z(x, y)e^{-j\beta z}$, can be reduced to a two-dimensional wave equation for h_z;

$$\left(\frac{\partial^2}{\partial x^2} + \frac{\partial^2}{\partial y^2} + k_c^2\right) h_z = 0, \tag{2.3}$$

since $k_c^2 = k^2 - \beta.$

The TE wave impedance can be found as

$$Z_{TE} = \frac{E_x}{H_y} = \frac{-E_y}{H_x} = \frac{\omega\mu}{\beta} = \frac{k\eta}{\beta}. \tag{2.4}$$

The partial equation (2.3) can be solved by the method of separation of variables by letting.

$$h_z(x,y) = X(x)Y(y) \tag{2.5}$$

and substituting into equation (2.3) to obtain

$$\frac{1}{X}\frac{d^2X}{dx^2} + \frac{1}{Y}\frac{d^2Y}{dy^2} + k_c^2 = 0 \tag{2.6}$$

Then, by the usual separation of variables argument, each of the term in equation (2.6) must be equal to a constant, so separation constants k_x and k_y are defined, such that

$$\frac{d^2X}{dx^2} + k_x^2 X = 0 \tag{2.7a}$$

$$\frac{d^2Y}{dy^2} + k_y^2 Y = 0 \tag{2.7b}$$

And $$k_x^2 + k_y^2 = k_c^2. \tag{2.8}$$

The general solution for h_z can be written as

$$h_z(x,y) = (A\cos k_x x + B\sin k_x x)(C\cos k_y y + D\sin k_y y) \tag{2.9}$$

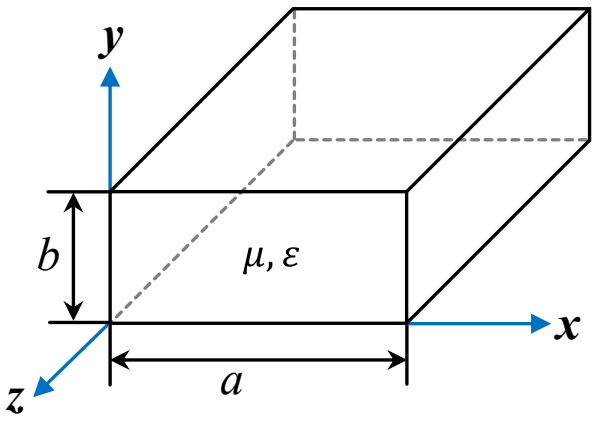

Figure 2.1 Rectangular waveguide.

To evaluate the constant in equation (2.9) we must apply the boundary conditions on the electric field components tangential to the waveguide walls. That is,

$$e_x(x,y)=0, \qquad \text{at } y=0,b, \tag{2.10a}$$

$$e_y(x,y)=0, \qquad \text{at } x=0,a, \tag{2.10b}$$

We must first use equation (2.1c) and equation (2.1d) to find e_x and e_y from h_z:

$$e_x=\frac{-j\omega\mu}{k_c^2}k_y(A\cos k_x x+B\sin k_x x)(-C\cos k_y y+D\sin k_y y) \tag{2.11a}$$

$$e_y=\frac{-j\omega\mu}{k_c^2}k_x(-A\cos k_x x+B\sin k_x x)(C\cos k_y y+D\sin k_y y) \tag{2.11b}$$

Then from equation (2.10a) and equation (2.11a), we see that $D = 0$, and $k_y = n\pi/b$ for n = 0,1,2, ... From equation (2.10b) and equation (2.11b) we have that $B = 0$, and $k_x = m\pi/a$ for m = 0,1,2, ... The final solution for H_z is then

$$H_Z(x,y,z)=A_{mn}\cos\frac{m\pi x}{a}\cos\frac{n\pi y}{b}e^{-j\beta z}, \tag{2.12}$$

where, A_{mn} is an arbitrary amplitude constant composed of the remaining constant A and C of equation (2.9).

The transverse field components of the TE_{mn} mode can be found using equation (2.1) and equation (2.12):

$$E_x=\frac{j\omega\mu n\pi}{k_c^2 b}A_{mn}\cos\frac{m\pi x}{a}\sin\frac{n\pi y}{b}e^{-j\beta z}, \tag{2.13a}$$

$$E_y=\frac{-j\omega\mu m\pi}{k_c^2 a}A_{mn}\sin\frac{m\pi x}{a}\cos\frac{n\pi y}{b}e^{-j\beta z}, \tag{2.13b}$$

$$H_x=\frac{j\beta m\pi}{k_c^2 a}A_{mn}\sin\frac{m\pi x}{a}\cos\frac{n\pi y}{b}e^{-j\beta z}, \tag{2.13c}$$

$$H_y = \frac{j\beta n\pi}{k_c^2 b} A_{mn} \cos\frac{m\pi x}{a} \sin\frac{n\pi y}{b} e^{-j\beta z} \tag{2.13d}$$

The propagation constant is

$$\beta = \sqrt{k^2 - k_c^2} = \sqrt{k^2 - \left(\frac{m\pi}{a}\right)^2 - \left(\frac{n\pi}{b}\right)^2}, \tag{2.14}$$

which is seen to be real, corresponding to a propagation mode, when

$$k > k_c = \sqrt{\left(\frac{m\pi}{a}\right)^2 - \left(\frac{n\pi}{b}\right)^2}$$

Each mode (combination of m and n) thus has a cutoff frequency $f_{c_{mn}}$ given by

$$f_{c_{mn}} = \frac{k_c}{2\pi\sqrt{\mu\varepsilon}} = \frac{1}{2\pi\sqrt{\mu\varepsilon}} \sqrt{\left(\frac{m\pi}{a}\right)^2 + \left(\frac{n\pi}{b}\right)^2} \tag{2.15}$$

The mode with the lowest cutoff frequency is called the dominant mode; since we have assumed $a > b$, the lowest f_c occurs for the TE_{10} ($m = 1$, $n = 0$) mode:

$$f_{c_{10}} = \frac{1}{2a\sqrt{\mu\varepsilon}} \tag{2.16}$$

At a given operating frequency f, only those modes having $f_c < f$ will propagate; modes with $f_c > f$ will lead to an imaginary β (or real α), meaning that all field components will decay exponentially away from the source of excitation. Such modes are referred to as cutoff, or evanescent, modes.

From equation (2.4) the wave impedance that relates the transverse electric and magnetic fields is

$$Z_{TE} = \frac{E_x}{H_y} = \frac{-E_y}{H_x} = \frac{k\eta}{\beta}, \tag{2.17}$$

when, $\eta = \sqrt{\mu/\varepsilon}$ is the intrinsic impedance of the material filled the waveguide.

The guide wavelength is defined as the distance between two equal phase planes along the waveguide and is equal to

$$\lambda_g = \frac{2\pi}{\beta} > \frac{2\pi}{k} = \lambda, \tag{2.18}$$

which is thus greater than λ, the wavelength of a plane wave in the filling medium. The phase velocity is

$$v_p = \frac{\omega}{\beta} > \frac{\omega}{k} = 1/\sqrt{\mu\varepsilon}, \tag{2.19}$$

which is greater than $1/\sqrt{\mu\varepsilon}$, the speed of light (plane wave) in the filling material.

In most applications, the operating frequency and guide dimensions are chosen so that only the dominant TE_{10} mode will propagate. Because of the practical importance of the TE_{10} mode.

Specializing equation (2.12) and equation (2.13) to the $m = 1$, $n = 0$ case gives the following results for the TE_{10} mode fields:

$$H_z = A_{10} \cos\frac{\pi x}{a} e^{-j\beta z}, \tag{2.20a}$$

$$E_y = \frac{-j\omega\mu a}{\pi} A_{10} \sin\frac{\pi x}{a} e^{-j\beta z}, \tag{2.20b}$$

$$H_x = \frac{-j\beta a}{\pi} A_{10} \sin\frac{\pi x}{a} e^{-j\beta z}, \tag{2.20c}$$

$$E_x = E_z = H_y = 0. \tag{2.20d}$$

In addition, for the TE_{10} mode,

$$k_c = \pi/a, \tag{2.21}$$

$$\beta = \sqrt{k^2 - \left(\pi/a\right)^2}. \tag{2.22}$$

Fig. 2.2 shows the field lines for the lowest order TE mode (TE_{10}).

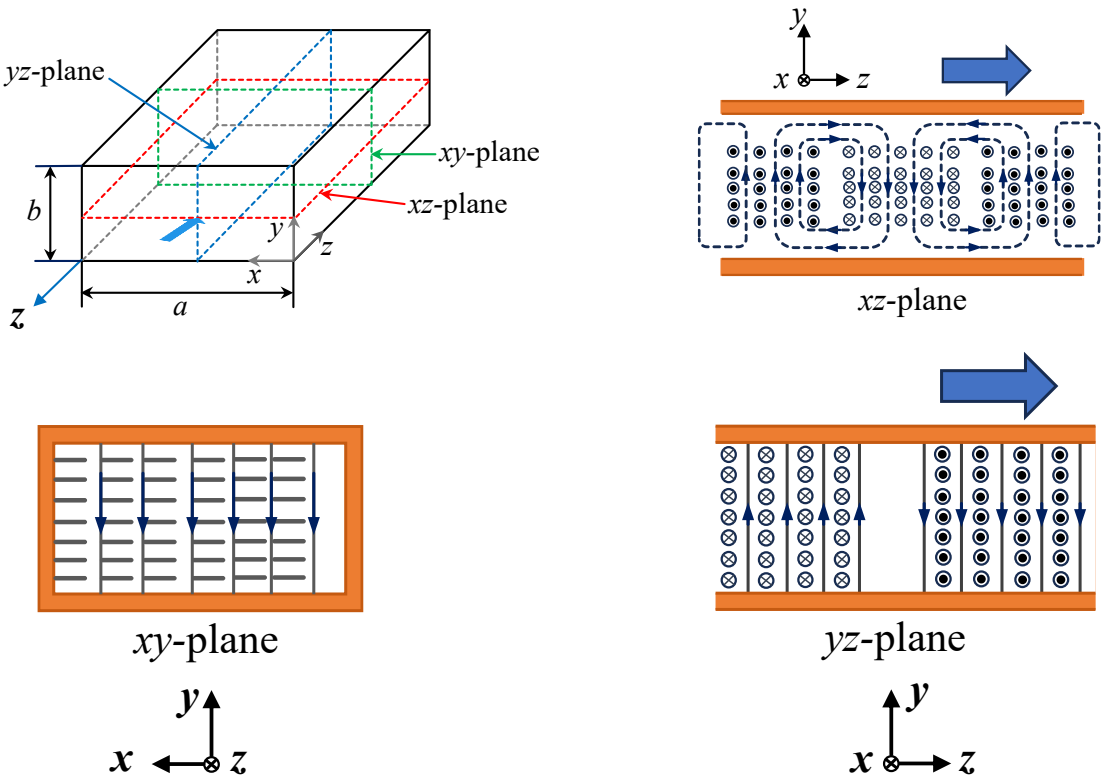

Figure 2.2 Field lines for the lowest order TE mode (TE_{10}).

2.1.2 Microstrip Line

Microstrip lines are one of the most popular types of planar transmission lines, primarily because it can be fabricated by photolithographic processes and it easily integrated with other passive and active microwave devices. The geometry of a microstrip line is shown in Fig. 2.3 (a). A conductor of width W is printed on a thin, grounded dielectric substrate of thickness T and relative permittivity ε_r. A sketch of the field lines is shown in Fig. 2.3 (b).

In most practical applications, the dielectric substrate is electrically very thin ($T << \lambda$), and so the fields are quasi-TEM. The fields are essentially the same as those of static cases. Thus, good approximations for the phase velocity, propagation constant, and characteristic impedance can be obtained from static quasi-static solutions. Then the phase velocity and propagation constant can be expressed as,

$$v_p = \frac{c}{\sqrt{\varepsilon_e}}, \tag{2.23}$$

$$\beta = k_0\sqrt{\varepsilon_e}, \tag{2.24}$$

where ε_e is the effective dielectric constant of the microstrip line. Since some of the field lines are in the dielectric region and some are in the air, the effective dielectric constant satisfies the relation,

$$1 < \varepsilon_e < \varepsilon_r$$

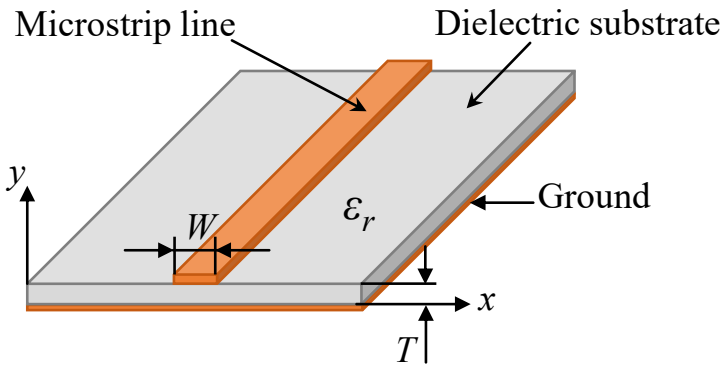

(a) Construction of microstrip line

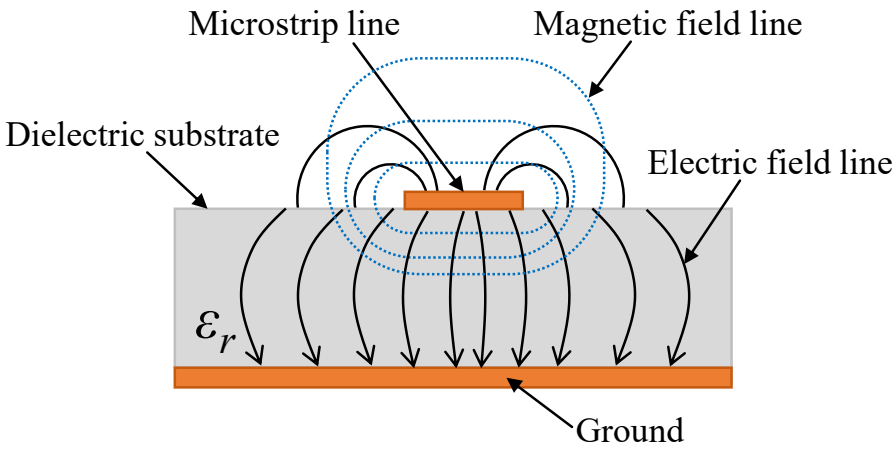

(b) Electromagnetic field distribution in quasi-TEM mode

Figure 2.3 Microstrip line.

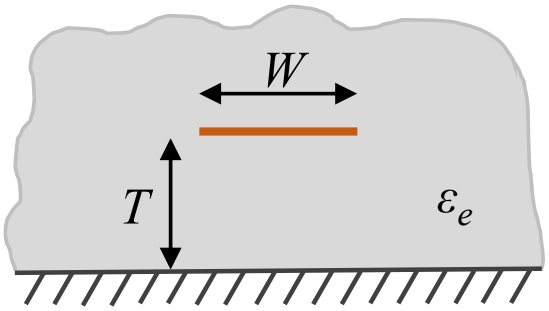

Figure 2.4 Equivalent geometry of quasi-TEM microstrip line, where the dielectric substrate has been replaced with a homogeneous medium of effective relative permittivity, ε_e.

and is dependent on the substrate thickness, T, and conductor width W. The effective dielectric constant of a microstrip line is given approximately by

$$\varepsilon_e = \frac{\varepsilon_r + 1}{2} + \frac{\varepsilon_r - 1}{2} \frac{1}{\sqrt{1 + \frac{12T}{W}}}. \tag{2.25}$$

The effective dielectric constant can be interpreted as the dielectric constant of a homogeneous medium that replaces the air and dielectric region of the microstrip line as shown in Fig. 2.4.

Given the dimensions of the microstrip line, the characteristic impedance can be calculated as

$$Z_0 = \begin{cases} \frac{60}{\sqrt{\varepsilon_e}} In\left(\frac{8T}{W} + \frac{W}{4T}\right) for \frac{W}{T} \leq 1 \\ \frac{120\pi}{\sqrt{\varepsilon_e}\left[\frac{W}{T} + 1.393 + 0.667 In\left(\frac{W}{T} + 1.444\right)\right]} for \frac{W}{T} \geq 1 \end{cases} \tag{2.26}$$

For a given characteristic impedance Z_0 and dielectric constant ε_r, the W/T can be found as

$$\frac{T}{W} = \begin{cases} \frac{8e^A}{e^{2A} - 2} for \frac{W}{T} < 2 \\ \frac{2}{\pi}\left[B - 1 - In(2B - 1) + \frac{\varepsilon_r - 1}{2\varepsilon_r}\left\{In(B - 1) + 0.39 - \frac{0.61}{\varepsilon_r}\right\}\right] for \frac{W}{T} > 2, \end{cases} \tag{2.27}$$

where,

$$A = \frac{Z_0}{60}\sqrt{\frac{\varepsilon_r + 1}{2}} + \frac{\varepsilon_r - 1}{\varepsilon_r + 1}\left(0.23 + \frac{0.11}{\varepsilon_r}\right)$$

$$B = \frac{377\pi}{2Z_0\sqrt{\varepsilon_r}}$$

2.1.3 Coplanar Waveguide

Microstrip is the most popular medium for circuit design at frequencies ranging from several hundred megahertz to tens of gigahertz. However, the electrical characteristics of a microstrip line are sensitive to variations of substrate thickness, and radiation from a microstrip line increases when the substrate is thick. The substrate thickness is not well controlled and can vary by in many substrate technologies. As a result, the characteristic impedance will change by about the same amount. This is not acceptable in many designs where microstrip synthesis should be accurate to or so. The lateral dimensions, however, are well controlled, being photolithographically defined and then etched.

A solution to the problems of microstrip is a coplanar waveguide (CPW) shown in Fig. 2.5 (a). CPW consists of a central strip flanked by two metal half-planes that carry the return current. The outer conductors can be regarded as ground, but they do not need to be explicitly connected to ground. Provided that the substrate is sufficiently thick, in practice this means that the substrate thickness is two or three times greater than both the strip width and the metal separation, the electrical characteristics of CPW are entirely determined by the lateral dimensions, since all of the metallization is on one layer.

Of course, the infinite half-grounds of CPW cannot be produced so a more realistic implementation of CPW is finite ground CPW (FGCPW), shown in Fig. 2.5 (b), where the signal return conductors are of finite width. For both the CPW and FGCPW lines, the vitalization

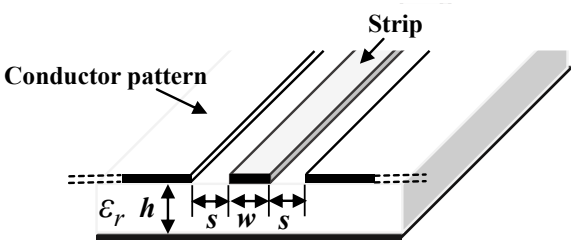

(a) Conventional

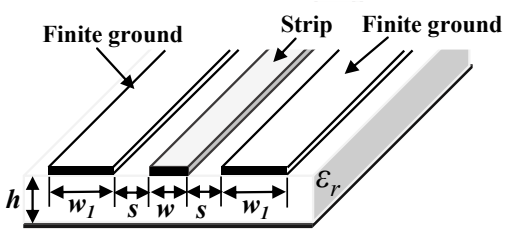

(b) finite ground CPW (FGCPW)

Figure 2.5 Coplanar waveguide (CPW)

and currents are confined to a single layer. However, the following discussion focuses on the idealized CPW structure in Fig. 2.5 (a) as this has been studied extensively. However, the characteristics of FGCPW are very close to those of CPW if $w_1 \geq 3w$ (see Fig. 2.5 (b)).

The fields in CPW, and thus the EM energy, are almost equally divided between air and dielectric, especially when the gap is small relative to the thickness of the dielectric. The effective relative permittivity of CPW is [3]

$$\varepsilon_e = \varepsilon_{r,e} = 0.5(\varepsilon_r + 1)\{\tanh[1.785\log(h/d) + 1.75] \tag{2.28}$$

$$+(ks/h)[0.04 - 0.7k + 0.01(1 - 0.1\varepsilon_r)(0.25 + k)]\}$$

which is accurate to 1.5% for $h/s \geq 1$. In equation (2.28)

$$k = \frac{w}{w + 2s} \tag{2.29}$$

Simply taking the effective permittivity as $(\varepsilon_r + 1)/2$ is a good starting point in analysis and design. The characteristic impedance of CPW is [4]

$$Z_0 = \frac{30\pi}{\sqrt{\varepsilon_e}} \frac{K'(k)}{K(k)} \tag{2.30}$$

where

$$k' = \sqrt{(1 - k^2)} \text{ and } K'(k) = K(k') \tag{2.31}$$

$K(k)$ and $K(k')$ are elliptic integrals, but the ratio, which is all that is required, is much simpler [4]:

$$\frac{K(k)}{K'(k)} \approx \frac{1}{\pi} \ln\left(2\frac{1 + \sqrt{k}}{1 - \sqrt{k}}\right) \qquad 0 \leq k \leq 0.707 \tag{2.32}$$

$$\frac{K'(k)}{K(k)} \approx \frac{1}{\pi} \ln\left(2\frac{1 + \sqrt{k'}}{1 - \sqrt{k'}}\right) \qquad 0.707 < k < 1 \tag{2.33}$$

Note that with CPW, Z_0 is determined by the ratio of the center strip width w to the gap width s. This makes the design of a CPW line with a particular Z_0 non-unique because an

infinite range of w and s values will result in a specific Z_0 requirement. This provides additional design flexibility.

The various CPW structures as shown in Fig. 2.6 are used to realize transmission line elements. The CPW-to-microstrip transition shown in Fig. 2.6 (g) requires vias to transfer the ground plane from the same surface as the strip in the CPW line to the second metal plane that forms the ground of the microstrip.

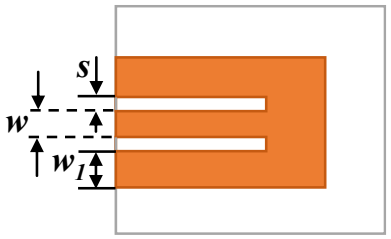

(a) Short circuit

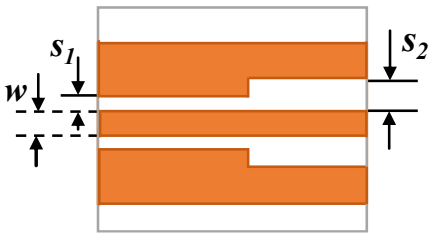

b) Impedance step out

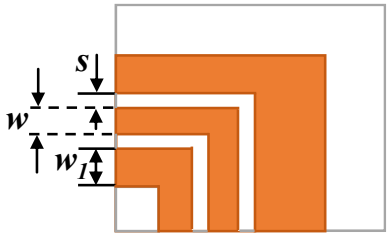

(c) Right-angled bend

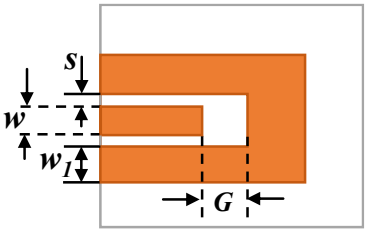

(d) Open circuit

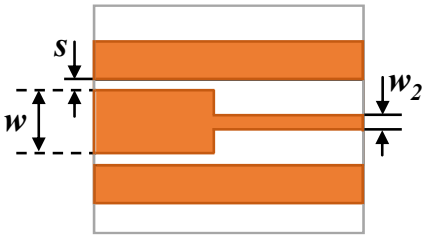

(e) Impedance step in

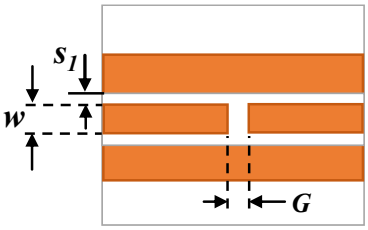

(f) Gap capacitor

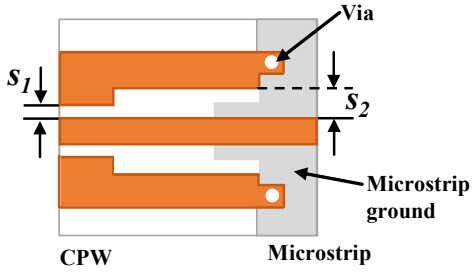

(g) CPW-to microstrip transition

Figure 2.6 Various CPW structures.

2.1.4 Grounded Coplanar Waveguide

The grounded coplanar waveguide (GCPW) is another popular transmission line structure used in microwave PCB design. Figure 2.7 shows the grounded coplanar waveguide configuration with two material layers of thickness and between two backing ground planes. The width of the signal conductor and the separation from the ground conductors are shown as w and s respectively. A material with permittivity and permeability is placed in the upper portion of the GCPWG and the material with properties is placed in the lower portion. Dimensions are chosen such that $2s + w \ll \lambda/2$ to ensure that the GCPWG supports a quasi-TEM mode of propagation [5].

The procedure for the extraction of the complex permittivity and permeability is comprised of two parts. The first part is the calculation of the filling factors through conformal mapping that describes the physical structure. The duality property along with the filling factors can then be used to construct a relationship between the effective permittivity (ε_{eff}) and effective permeability (μ_{eff}) of the entire structure, and the relative permittivity (ε_r) and relative permeability (μ_r) of the material. The second step involves deriving a relation for the ε_{eff} and μ_{eff} in terms of the characteristic impedance and propagation constant of the structure, which in turn, can be obtained from the full-wave simulated or measured scattering parameters of the structure. The complex permittivity and complex permeability of the material can be obtained by combining these two steps.

The filling factors are defined as the ratio of energy stored in one of the filling materials to the total energy stored in all the filling materials. Following a similar approach to the conformal mapping technique [6], filling factors for the GCPWG can be derived. For the structure shown in Fig. 2.7, the two filling factors, q_1 and q_2 can be derived as follows:

$$q_1 = \frac{\dfrac{K(k_1)}{K(k_1')}}{\dfrac{K(k_1)}{K(k_1')} + \dfrac{K(k_2)}{K(k_2')}} \tag{2.34}$$

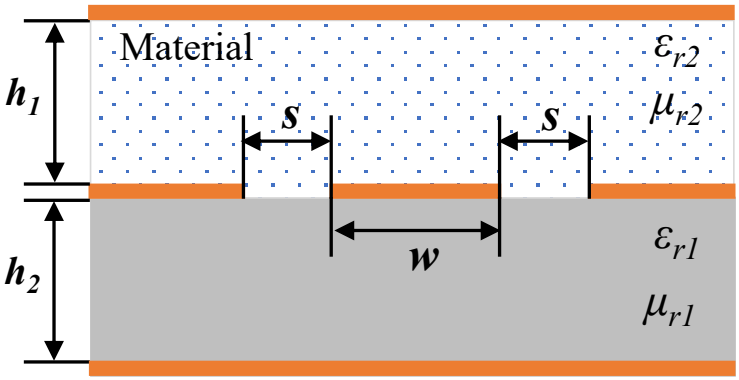

Figure 2.7 Grounded coplanar waveguide configuration.

$$q_2 = \frac{\dfrac{K(k_2)}{K(k_2')}}{\dfrac{K(k_1)}{K(k_1')} + \dfrac{K(k_2)}{K(k_2')}} \tag{2.35}$$

where K(k_1) and K(k_2) are the elliptic integrals of the first kind of k_1 and k_2, respectively and k_1, k_2, k_1' and k_2' are given in equations (2.36)-(2.39) [6]

$$k_1 = \tanh\left(\frac{\pi\omega}{4h_1}\right) \Big/ \tanh\left(\frac{\pi(2s+w)}{4h_1}\right) \tag{2.36}$$

$$k_2 = \tanh\left(\frac{\pi\omega}{4h_2}\right) \Big/ \tanh\left(\frac{\pi(2s+w)}{4h_2}\right) \tag{2.37}$$

$$k_1' = \sqrt{1-k_1^2} \tag{2.38}$$

$$k_2' = \sqrt{1-k_2^2} \tag{2.39}$$

The transmission properties of the GCPWG are dependent on the material properties of the substrate. The effective permittivity is defined as the ratio of the total capacitance of the complete GCPWG to the capacitance when all dielectrics are replaced by free space. The complex permittivity, (ε_{r2}) and permeability, (μ_{r2}) of the material can be related to the material properties, effective values, and filling factors as shown in equations (2.40) and (2.41) [6]

$$\varepsilon_{r2} = \varepsilon_{r2}' - j\varepsilon_{r2}'' = \varepsilon_{r2}'(1 - j\tan\delta_e) \tag{2.40}$$

$$= \frac{\varepsilon_{reff}}{q_2} - \frac{q_1 \varepsilon_{r1}}{q_2}$$

$$\mu_{r2} = \mu'_{r2} - j\mu''_{r2} = \mu'_{r2}(1 - j\tan\delta_m) \tag{2.41}$$

$$= \frac{q_2 \mu_{r1} \mu_{reff}}{q_1} \left(\frac{\mu_{r1}}{q_1} - \mu_{reff} \right)$$

where $\tan\delta_e$ and $\tan\delta_m$ are the dielectric and magnetic loss tangents of the material. equation (2.41) sets a condition that $\mu_{r1}/q_1 > \mu_{reff}$, which in turn, limits the maximum value of μ_{r2} that can be determined from this method for a given configuration. The ratio μ_{r1}/q_1 can be increased either by choosing the relative permeability of the material to be higher and (or) by choosing the structural dimensions.

The characteristic impedance and propagation constant can be expressed in terms of the known *ABCD* parameters and the length of the coplanar waveguide. The *ABCD* parameters for the GCPWG structure of length can be expressed in terms of the propagation parameters of the transmission line as

$$\begin{bmatrix} A & B \\ C & D \end{bmatrix} = \begin{bmatrix} \cosh(\gamma l) & Z_c \sinh(\gamma l) \\ \dfrac{\sinh(\gamma l)}{Z_c} & \cosh(\gamma l) \end{bmatrix} \tag{2.42}$$

where Z_c, and γ are the characteristic impedance and the propagation constant of the transmission line, respectively. The characteristic impedance and the propagation constant can also be expressed as equations (2.43) and (2.44) [7]

$$Z_c = Z_{c\_V} \sqrt{\frac{\mu_{reff}}{\varepsilon_{reff}}} \tag{2.43}$$

$$\gamma = \omega \sqrt{\varepsilon_0 \mu_0} \sqrt{\varepsilon_{reff} \mu_{reff}} \tag{2.44}$$

where Z_{c_V} is the characteristic impedance when the filled material is replaced with free space (ε_0 =8.854×10^{-12} F/m, μ_0 =4π×10^{-7} H/m) and $\omega, \varepsilon_{reff}$, and μ_{reff} are angular frequency, effective relative permittivity, and effective relative permeability, respectively.

From equations (2.43) and (2.44), the effective relative permittivity and permeability are derived as

$$\varepsilon_{reff} = \frac{Z_{c\_V}\gamma}{\omega Z_c \sqrt{\varepsilon_0 \mu_0}} \tag{2.45}$$

$$\mu_{reff} = \frac{Z_c \gamma}{\omega Z_{c\_V} \sqrt{\varepsilon_0 \mu_0}}. \tag{2.46}$$

From the above deduction, the effective relative permittivity and permeability can be derived from the *S*-parameters of a GCPWG. We can obtain the material properties of the material by substituting equations (2.45) and (2.46) in equations (2.40) and (2.41). It may be noted that for magnetic material characterization, demagnetization corrections are not necessary for the coplanar ground-signal-ground configuration with a wide layer of magnetic material [5].

2.1.5 Grounded Suspended Coplanar Waveguide

To further reduce the loss, based on CPW, a suspended coplanar waveguide was proposed. An ideal suspended coplanar waveguide model with three zones labeled as I, II, and III, respectively, has been proposed, as shown in Fig. 2.8. The characteristic impedance of the circuit model can be calculated by the conformal mapping method.

For zone I, the capacitance per unit length is set to be C_1, and the conformal mapping process is plotted in Fig. 2.9. Zone I is the inner region of a polygon on the *z*-plane, as shown in Fig. 2.9 (a). Firstly, the exponential transformation as

$$t = \exp\left(\frac{\pi z}{h_1}\right) \tag{2.47}$$

is used for transforming the rectangular area shown in Fig.2.9 (a) into the lower part of the *t*-plane, as shown in Fig. 2.9 (b). Each point on the *t*-plane is corresponding to each point on the *z*-plane, that is $t_1 = \exp(-\pi b / h_1), t_2 = \exp(-\pi a / h_1), t_3 = \exp(\pi a / h_1), t_4 = \exp(\pi b / h_1)$. Then by using the Schwarz-Christoffel transformation, the lower part of the t-plane can be transformed into the rectangular domain of the w-plane, as shown in Fig. 2.9 (c).

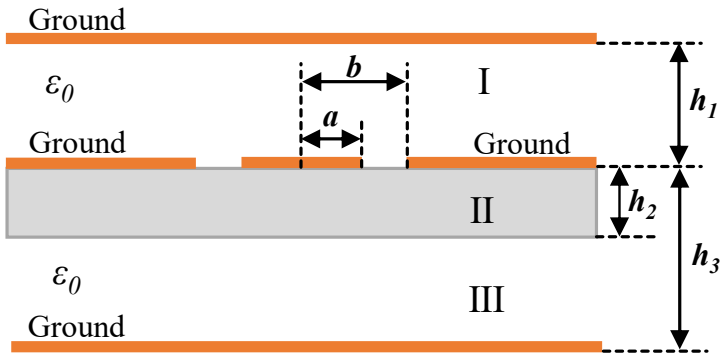

Figure 2.8 Ideal suspended coplanar waveguide structure.

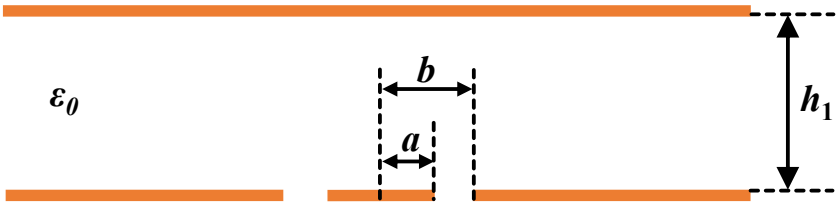

(a) z-plane

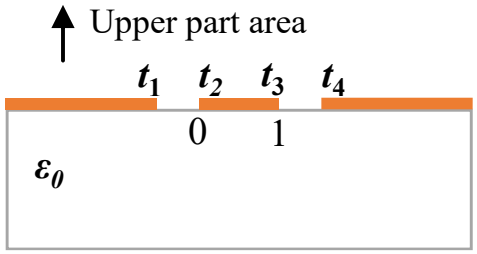

(b) t-plane

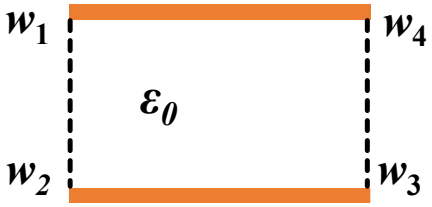

(c) w-plane

Figure 2.9 Schematic diagram of the transformation steps for solving C_1.

2.1.6 Coupling Strip Line

A symmetrical strip line is shown in Fig. 2.10. A strip line resembles a microstrip line and comprises a center conductor pattern symmetrically embedded completely within a dielectric, the top and bottom layers of which are conducting ground planes. The strip width is considered to have a thickness that is very small so that the strip is a distance from each of the ground planes and the ground planes are separated by *h*. The strip is completely surrounded by the dielectric and so this is a homogeneous medium and there is no need to introduce an effective permittivity.

The characteristic impedance of a strip line is [8], [9]

$$Z_0 = \left[\frac{30\pi}{\sqrt{\varepsilon_r}}\right]\frac{(1-t/b)}{(w_{eff}/b)+C_f}, \tag{2.48}$$

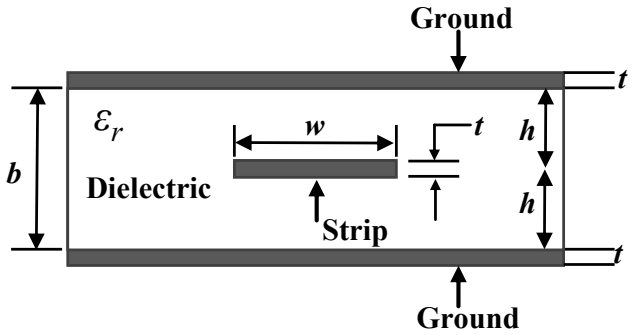

Figure 2.10 Strip line cross-section.

where the effective width of the strip, w_{eff}, is obtained from

$$\frac{w_{eff}}{b} = \begin{cases} \dfrac{w}{b} - \left[\dfrac{(0.35-w/b)^2}{(1+12t/b)}\right] & \dfrac{w}{b} < 0.35 \\ \dfrac{w}{b} & \dfrac{w}{b} \geq 0.35 \end{cases} \tag{2.49}$$

and

$$C_f = \frac{2}{\pi}\ln\left[\frac{1}{1-(t/b)}+1\right] - \frac{t}{\pi b}\ln\left\{\frac{1}{[1-(t/b)]^2}-1\right\} \tag{2.50}$$

where C_f accounts for the fringing capacitance at the edges of the strip and incorporates the effect of the strip thickness for $t \ll b$. The fringing capacitance per unit length (e.g., F/m) at each corner of the strip is

$$C'_f = \frac{\varepsilon_0 \varepsilon_r C_f}{1 - t/b} \tag{2.51}$$

and is shown in Fig. 2.11. The accuracy of these formulas is better than 1% for $W/(b-t) > 0.05$ and $t/b < 0.025$. Finding the physical length required to realize an electrical length θ (degrees) is also relatively straightforward. First, evaluate the wavelength using

$$\lambda_g = \frac{300}{F\sqrt{\varepsilon_r}} \quad \text{mm.} \tag{2.52}$$

When F is in gigahertz automatically provides the wavelength in millimeters. In equation (2.52), ε_r is the relative permittivity of the filling dielectric material and, of course, the effective relative permittivity $\varepsilon_{eff} = \varepsilon_r$.

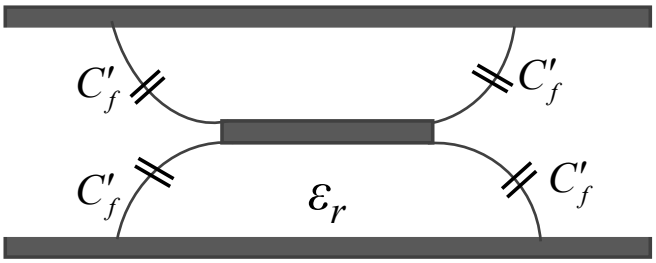

Figure 2.11 Fringe capacitance at the corners of the strip in a strip lines transmission line.

For strip lines with a homogeneous dielectric, the phase velocity is the same, and frequency independent, for all TEM modes. A configuration of two coupled strip lines (3-conductor system) may have two independent TEM modes, an odd mode, and an even mode as shown in Fig. 2.12.

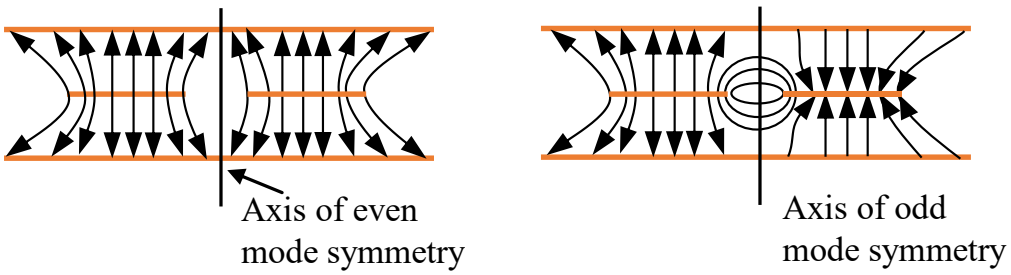

Figure 2.12 Even and odd modes in coupled strip lines.

The analysis of coupled strip lines is required for the design of directional couplers. Besides the phase velocity the odd and even mode impedances $Z_{0,\mathrm{odd}}$ and $Z_{0,\mathrm{even}}$ must be known. They are given as a good approximation for the side coupled structure as shown in Fig. 2.13 (a). They are valid as a good approximation for the structure shown in Fig. 2.13.

$$Z_{0,even} = \frac{1}{\sqrt{\varepsilon_r}} \cdot \frac{94.15\Omega}{\frac{w}{b}+\frac{ln\,2}{\pi}+\frac{1}{\pi}ln\left(1+tanh\left(\frac{\pi s}{2b}\right)\right)} \tag{2.53}$$

$$Z_{0,odd} = \frac{1}{\sqrt{\varepsilon_r}} \cdot \frac{94.15\Omega}{\frac{w}{b}+\frac{ln\,2}{\pi}+\frac{1}{\pi}ln\left(1+coth\left(\frac{\pi s}{2b}\right)\right)} \tag{2.54}$$

A graphical presentation of equations (2.55)-(2.57) is also known as the Cohn nomographs [11]. For a quarter-wave directional coupler, very simple design formulae can be given

$$Z_{0,odd} = Z_0\sqrt{\frac{1+C_0}{1-C_0}} \tag{2.55}$$

$$Z_{0,even} = Z_0\sqrt{\frac{1+C_0}{1-C_0}} \tag{2.56}$$

$$Z_0 = \sqrt{Z_{0,odd}Z_{0,even}} \tag{2.57}$$

where C_0 is the voltage coupling ratio of the $\lambda/4$ coupler.

In contrast to the 2-hole waveguide coupler this type couples backward, i.e., the coupled wave leaves the coupler in the direction opposite to the incoming wave. Strip line coupler technology is now rather widespread, and very cheap high-quality elements are available in a wide frequency range. An even simpler way to make such devices is to use a section of shielded 2-wire cable.

(a) Side-coupled parallel lines and (b) Broad-coupled parallel lines.

Figure 2.13 Types of coupled strip lines.

2.1.7 Differential Line

A conventional differential line (DL), commonly used on typical digital circuit boards for transmitting high-speed digital data, has fundamental limitations on the maximum signal bandwidth (~10 GHz), mainly due to signal skew, multiple line coupling, and EM interference. Therefore, to support super-high-speed digital data transmission, especially for beyond 5G communications, a practical high-performance transmission structure for digital signals is required.

A differential line (DL) is the most commonly used transmission line for differential signaling. The DL consists of two conductors and a ground plane, which is essentially a form of two microstrip lines laid out in parallel. The typical characteristic line impedance of the DL is 100 Ω, which is twice the single-ended (microstrip) line impedance of 50 Ω. The DL is easily fabricated and has good accessibility for installation of the various chips, with the advantages of reduced noise effects and low voltage signal detection. That is why the DL has been widely adopted over the single-ended (microstrip) line for the high-speed signal lines in most digital circuits [12].

A DL is the most widely used transmission line for differential signaling on typical PCBs. Fig. 2.14 shows a conventional DL structure, which is composed of two conductor signal lines, a ground plane, and a substrate in between them. The two conductor lines of opposite polarities with a gap are placed on the top side of the substrate. The DL is equivalent to two coupled microstrip lines of opposite polarities with a gap. The conductor lines are electromagnetically (EM) coupled, and the amount of the EM coupling mostly depends on the gap width between the lines.

Two types of planar balanced lines for differential signaling a coplanar strip line (CPS) and a parallel line (PSL) are shown in Fig. 2.15. The CPS is a uniplanar structure with two conductor lines of the opposite polarities on the top side of the substrate, and the PSL is an

antipodal structure in which a dielectric substrate is placed between the two conductor lines of the opposite polarities, as shown in Fig. 15(a)-(b), respectively. Each of the conductor lines of the BLs are considered a ground line to the other one, which supports the differential signaling.

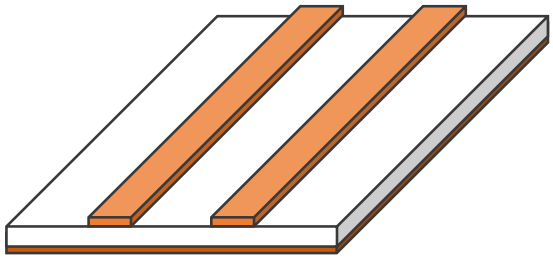

Figure 2.14 A perspective view of a conventional DL.

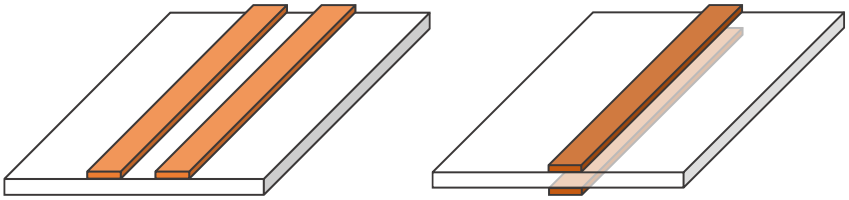

(a) CPS (b) PSL

Figure 2.15 Perspective views of the balanced lines.

2.1.8 Substrate Integrated Waveguide

Substrate-integrated waveguide (SIW) is a new possibility to the design of efficient circuits and components operating in the radio frequency (RF) and microwave frequency spectrum. Microstrip components are very good for low-frequency applications but are ineffective at extreme frequencies and involve rigorous fabrication concessions in the implementation of RF, microwave, and millimeter-wave components. This is due to wavelengths being short at higher frequencies. Waveguide devices, on the other hand, are ideal for higher frequency systems but are very costly, hard to fabricate, and challenging to integrate with planar components in the neighborhood.

SIW transmission line is basically a dielectric-filled waveguide implemented by two lines of conducting posts (also known as vias) implanted within a dielectric substrate, and electrically connecting the top and the bottom conducting walls [12]. The structural evolution

of the SIW technology is shown in Fig. 2.16 [13]. The evolution shows how the conventional rectangular waveguide presented in Fig. 2.16 (a) was modified by occupying the airspace with a dielectric material of dielectric constant, ε_r, as shown in Fig. 2.16 (b). The structure was further modified by using metallic posts to imitate/replace the two side walls as shown in Fig. 2.16 (c), to form the SIW. This paradigm-shifting technology can basically be generalized as a planar transmission line that portrays waveguide characteristics, as it builds the traditional waveguide on a section of a printed circuit board, substituting its metallic side walls with two rows of metalized vias. The substrate-integrated waveguide retains the benefits of a microstrip, including compactness and ease of integration, while also retaining some of the waveguide attributes, including minimal radiation loss, elevated unloaded Q-factor, and elevated power processing capacity. The very important advantage of the SIW transmission line technology is the opportunity to combine various devices (both active and passive) on a single substrate.

SIW and the traditional air-filled waveguide have comparable characteristics, as both technologies provide for $TE_{i,0}$ modes including $TE_{1,0}$, the dominant mode. Nevertheless, as opposed to the traditional air-filled waveguide which can maintain TM and $TE_{i,j}$ ($j \neq 0$) modes, the SIW is not able to maintain these modes due to the discontinuity in the side walls. Consequently, only the $TE_{i,0}$ modes can be supported in the SIW structure, as explained in [14]. The external current circulation of a conventional waveguide, with metallic posts on the thin walls, can be used to describe the fact of the presence of $TE_{1,0}$ mode in SIW, as shown in Fig. 2.17. This is due to surface currents being formed in guided wave constructions because of mode formation. According to [14], significant energy radiation should happen when the holes cut all the length of the current's transverse path. Alternatively, only an extremely small amount of radiation should happen when the holes cut through the current flow path. It can be observed from Fig. 2.17 that the holes do not cut the surface current on the side metallic wall. Hence, the $TE_{1,0}$ mode is maintained in the structure, which clarifies why the $TE_{i,0}$ modes can happen in the substrate-integrated waveguide structure.

The structure of the SIW transmission line is presented in Fig. 2.18. This physical geometry indicates the formation of the SIW by inserting a dielectric substrate in the middle of two opposite metal plates. The side walls of the SIW structure are achieved using two lines of regular metallic vias positioned adjacent to the lengths of the substrate. This is equivalent to the metal sidewalls of the conventional waveguide.

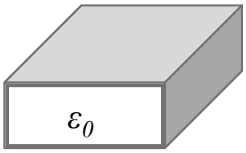

(a) Air-filled rectangular waveguide

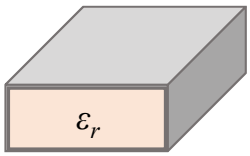

(b) Dielectric-filled rectangular waveguide

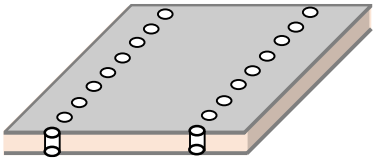

(c) Substrate-integrated waveguide

Figure 2.16 Evolution of SIW structure.

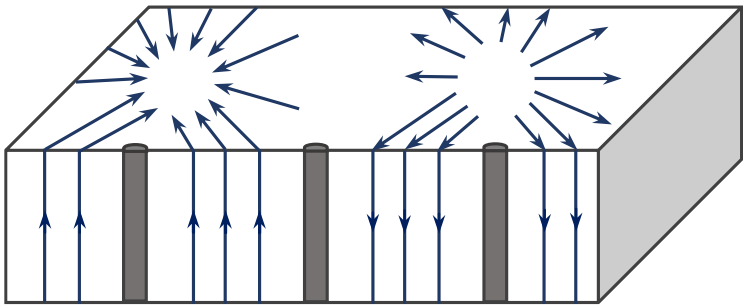

Figure 2.17 The TE_{10} mode surface current distribution of a conventional rectangular waveguide with metallic holes on the thin side walls.

Three fundamental design parameters must be considered when designing the substrate-integrated waveguide to function at an assigned frequency. These parameters are shown in Fig. 2.19 and include the substrate-integrated waveguide width, *w*, the metal via diameter, *d*, and the space or separation length between adjacent metal vias (that is, the pitch), *p*. Similar to the width of the conventional rectangular waveguide integrated waveguide, the SIW width relates to the cut-off frequency of its propagation mode. The *d* and the *p* parameters define the close relationship between the SIW structure and the rectangular waveguide. Reducing the value of *p* to *d*/2 essentially reduces the SIW to a regular dielectric-filled waveguide. Increasing the

value of p increases the amount of the SIW deviation from the conventional rectangular waveguide, with more EM energies emitting outward in the middle of the vias.

The physical size of the substrate-integrated waveguide cavity, at its basic TE_{101} mode, is calculated based on the matching resonance frequency, f_{101} as provided in equation (2.58). The design parameter w_{eff} gives the substrate-integrated waveguide effective width, l_{eff} gives its effective length, μ_r is the substrate relative permeability (μ_r =1 if substrate material is non-magnetic), ε_r is the substrate material dielectric constant, while c_0 gives the free space speed-of-light. Experimental formulations for the w_{eff} and the l_{eff} are provided in equation (2.60), with the simplified versions given in equation (2.59), and with the simplified versions given in equation (2.60). It is important to note that equations (2.59) and (2.60) are different versions of the same formulation. Hence both equations will return approximately the same value when applied in a calculation. equation (2.60) is just a simplified version of equation (2.59).

$$f_{101} = \frac{C_0}{2\pi\sqrt{\mu_r \varepsilon_r}} \left[\left(\frac{\pi}{w_{eff}} \right)^2 + \left(\frac{\pi}{l_{eff}} \right)^2 \right]^{0.5} \tag{2.58}$$

$$\left\{ \begin{array}{l} w_{eff} = w - 1.08\dfrac{d^2}{p} + 0.4\dfrac{d^2}{w} \\ l_{eff} = l - 1.08\dfrac{d^2}{p} + 0.1\dfrac{d^2}{l} \end{array} \right\} \tag{2.59}$$

$$\left\{ \begin{array}{l} w_{eff} = w - \dfrac{d^2}{0.95p} \\ l_{eff} = l - \dfrac{d^2}{0.95p} \end{array} \right\} \tag{2.60}$$

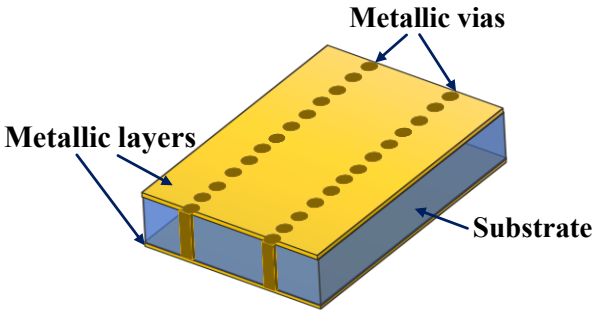

Figure 2.18 Physical structure of the substrate-integrated waveguide transmission line.

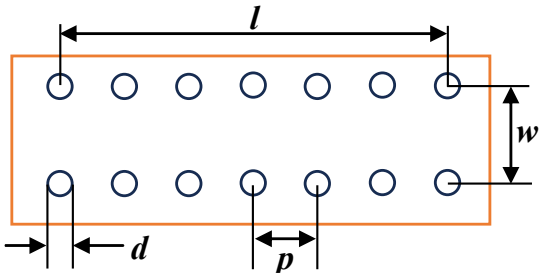

Figure 2.19 Substrate-integrated waveguide fundamental design parameters.

The conventional structure of the SIW has some limitations that can be linked to its evolution from the rectangular waveguide. One of the modified SIW structures is the substrate-integrated folded waveguide (SIFW) as indicated in Fig. 2.20 (a). This type of SIW allows for a 50% decrease in the physical size of a device due to the folded structure. The downside of SIFW is that it exhibits a slightly higher loss mechanism when compared to the standard/conventional version. The folding of the structure also means the requirement for a dual-layer fabrication process which is slightly more complex when compared to a single-layer fabrication process.

Another modified version of the SIW is the half-mode SIW (HMSIW) as shown in Fig. 2.20 (b). This type also allows for a 50% decrease in the physical dimension of a device such as the SIFW. However, unlike the SIFW, this type uses a symmetry plane to replace half of the standard SIW structure. The symmetry plane acts as a virtual magnetic wall used to replace one-half of the physical structure. This means that the HMSIW, like the standard SIW, is also manufactured using the single-layer manufacturing process. This is an added advantage over the SIFW.

The substrate-integrated ridge waveguide (SIRW) is another evolution of the standard SIW that has been investigated. The physical structure of SIRW is given in Fig. 2.20 (c). The SIRW is the SIW where a ridge is realized using a row of thin, partial-height metallic vias positioned in the center of the extended side of the SIW. This topology of the SIRW ensures that bandwidth improvement and compactness are achieved in an SIW device.

One other modification of the SIW that has been investigated is the substrate-integrated slab waveguide (SISW) as given in Fig.2.20 (d). In this evolution of the SIW, the dielectric material is regularly perforated with air-filled vias which are in the horizontal section of the SIW.

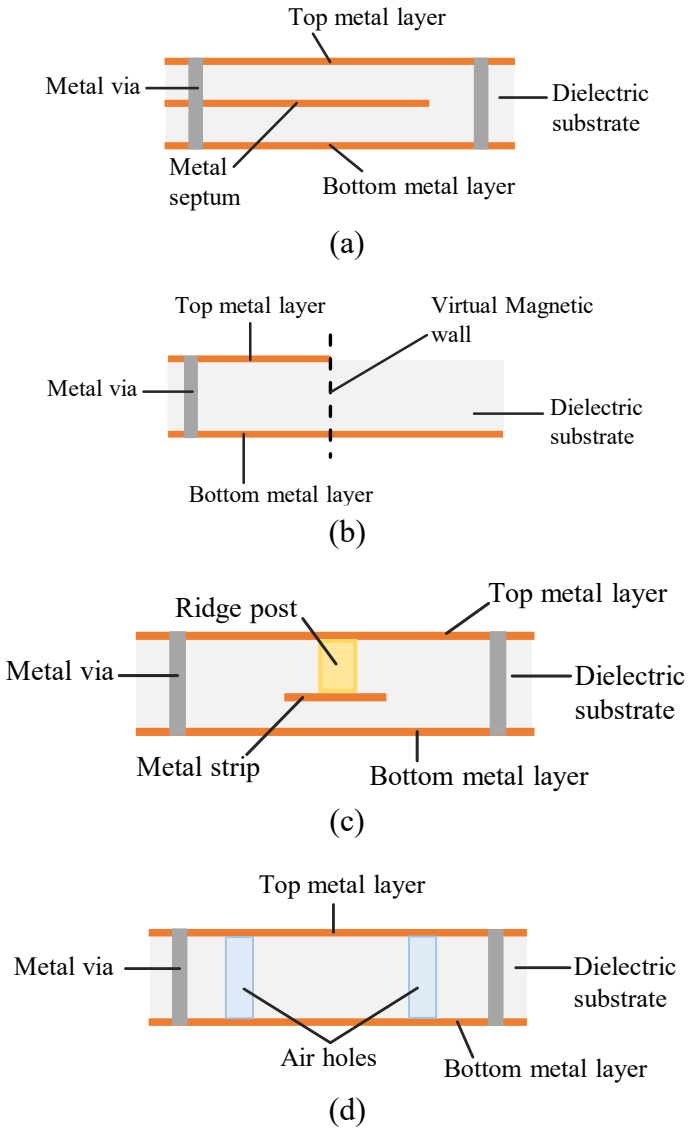

Figure 2.20 Cross section of the different versions of the compact SIW structures: (a) substrate integrated folded waveguide; (b) half-mode substrate-integrated waveguide; (c) substrate-integrated ridge waveguide; (d) substrate-integrated slab waveguide.

As SIW components are always integrated with other circuit components within a system, it is important to discuss the interconnection between devices. The transition sandwiched between planar transmission line technologies such as microstrips, and the substrate-integrated waveguide structure is a crucial part of the design of SIW devices. The tapered segment attaches a 50 Ω microstrip signal line to the substrate-integrated waveguide. The taper is utilized by converting the quasi-TEM mode in the microstrip technology to the TE_{10} mode of the substrate-integrated waveguide.

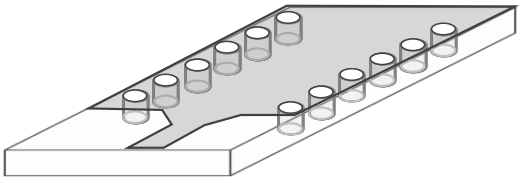

(a) microstrip-to-SIW transition based on a simple taper.

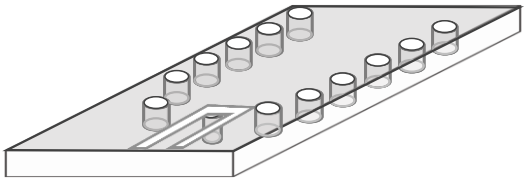

(b) CPW-to-SIW transition based on a current probe.

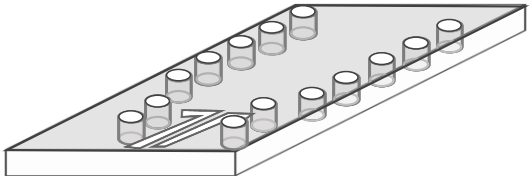

(c) CPW-to-SIW transition based on a ninety-degree bend.

Figure 2.21 Some popular transitions between planar transmission line and substrate-integrated waveguide.

Coplanar waveguide to substrate-integrated waveguide conversion established with a ninety-degree bend was reported in [15]. The new transition technique exploits the step impedance on a 50 Ω microstrip signal path, to the small impedance grounded coplanar waveguide, then linking to the SIW component through the brief small impedance grounded coplanar waveguide signal path. The conversion method is effective since it facilitates double flexibilities in managing input/output couplings; hence, the external quality factor may be altered by both altering the stepped impedance of the coplanar waveguide and the size of the brief coplanar waveguide signal path. Fig. 2.21 shows some of the popular transition techniques that have been employed in the design of substrate-integrated waveguide components.

2.2 Corrugaton Waveguide and Corrugation Structure

In a circular waveguide, the mode with the lowest loss is the TE_{01} mode. However, the field strength at the waveguide center for this mode is small and hence is not a good option for some applications as the electrons are to propagate down the center of the structure. A corrugation waveguide, as shown in Fig. 2.22, can be used in other applications such as a feed horn for a transmission line system due to its advantages of low cross-polarization field, low loss, and wide bandwidth. Its low attenuation feature is attractive for the transmission of high-power microwaves. The fundamental mode HE_{11} was found to have lower loss compared with the TE_{01} mode in the circular waveguide. It has been used to transport megawatt-level millimeter-wavelength radiation generated by gyrotron oscillators for fusion experiments such as ITER.

The corrugation waveguide contains circular waveguide steps and smooth sections. The properties of a corrugation waveguide with arbitrary radial corrugation depth can be accurately solved using a mode-matching method. For the periodically corrugation waveguide used for transmitting microwave power, analytical equations can be derived based on the fact that the waveguide radius is larger than the wavelength. The propagation characteristics of the periodically corrugation waveguide were studied using the simplified surface-impedance approach or the rigid equations taking into account the spatial harmonics in the corrugation gaps [16].

The surface-impedance approach assumes that only the lowest transverse magnetic (TM) standing wave exists in the slot and ignores its spatial harmonics. It gives a good approximation when the period per wavelength, defined by λ_0/p, is a reasonably large value and the corrugation slot length, defined by $w = p - b$ in Fig. 2.22, is a small value. At low frequencies, for example in the application of the microwave undulator, these assumptions would normally be satisfied. If only the lowest TM standing wave were present in the corrugation slot, its surface admittance at $r = r_1$ can be written as

$$\frac{H_\psi}{E_Z} = -jY_0 \frac{J_m'(x_1')Y_m(x_0') - J_m'(x_0')Y_m'(x_1')}{J_m(x_1')Y_m(x_0') - J_m(x_0')Y_m'(x_1')}, \tag{2.61}$$

where m indicates the azimuthal mode number, $x'_1 = kr_1$ and $x'_0 = kr_0$. J_m and Y_m are the first and second kinds of Bessel functions of order m, respectively. Y_0 is the free-space wave admittance. The surface admittance becomes 0 when

$$J_m'(x_1')Y_m(x_0') - J_m(x_0')Y_m'(x_1') = 0, \tag{2.62}$$

This is known as the balanced hybrid condition. If the operating frequency (f) and the waveguide radius (either r_0 or r_1) are given, the corrugation depth $d = r_0 - r_1$ can be determined from the equation. At $m = 1$ and $x'_1 >> 1$, the surface admittance can be further simplified as $H_\psi / E_z = jY_0 \cot(kd)$. The corrugation depth d would be equal to $\lambda_0/4$ to ensure $H_\psi = 0$.

Under the balanced hybrid condition and $x'_1 >> 1$, the dispersion curve between k and k_z is determined by

$$Kr_1 \frac{J_m'(Kr_1)}{J_m(Kr_1)} = \mp m \frac{k_z}{k}, \tag{2.63}$$

where $K^2 = k^2 - k_z^2$, the '-' in '$\mp$' denotes the HE modes, and the '+' denotes the EH modes. For a large radius, which leads to $k_z \simeq k$ and $m = 1$, equation (2.63) can be further simplified to $J_0(Kr_1) = 0$ for HE_{1n} modes and $J_2(Kr_1) = 0$ for EH_{1n} modes [17].

To describe the field distribution inside the corrugation waveguide, different eigenmode sets using TE/TM and HE/EH combinations have been derived. The field inside the corrugation waveguide with the linearly polarized mode sets can be simplified as

$$\begin{aligned} E_Z &= a_m J_m(Kr)\cos(m\varphi), \\ E_r &= -ja_m(k/K)J_{m\mp1}(Kr)\cos(m\varphi), \\ E_\varphi &= \mp(-j)a_m(k/K)J_{m\mp1}(Kr)\sin(m\varphi). \end{aligned} \tag{2.64}$$

Usually, a higher-order HE or EH mode is not linearly polarized. The suitable operating modes in the corrugation waveguide for the microwave undulator application are the HE_{11} and HE_{12} modes because they are low loss, linearly polarized, and have the peak electric field at the waveguide center.

The attenuation coefficient defined by the ratio between the lost power and the transported power per meter for the HE_{1n} modes, under the balanced hybrid condition, can be written as [17]

$$\alpha = \frac{1}{2}\left(\frac{R_s}{Z_0}\right)\frac{x_1^2 k}{x_1'^4}\left[\frac{1}{kb}\left(1+\frac{x_1'\pi}{2}\right)+x_1'\right], \tag{2.65}$$

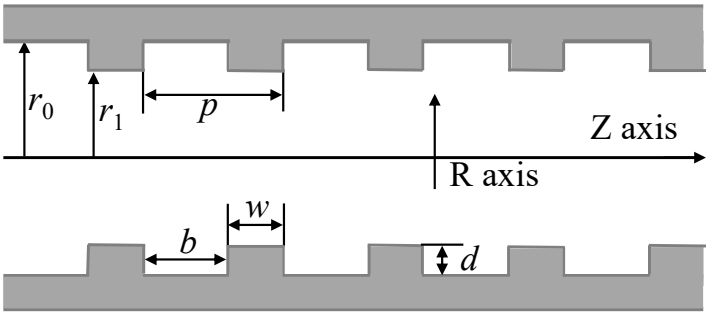

Figure 2.22 Schematic drawing of the corrugation waveguide.

where $Z_0 = 1/Y_0$ is the free space wave impedance, $R_s = (\pi f \mu_0 \sigma)^{1/2}$ is the resistivity of the corrugation metal waveguide and σ is the conductivity of the metal. Note that, oxygen-free high-conductivity copper was chosen, and $\sigma = 5.8 \times 10^7$ Sm^{-1} was used in the simulation. Equation (2.64) implies that the attenuation coefficient is proportional to r_1^{-3} and f^2 in the case of $x'_1 >> 1$.

The corrugation waveguide can be shortened at both ends to form a cavity. The resonance frequency of the corrugation waveguide can be estimated as

$$f = \frac{c}{\lambda_0} = \frac{c}{2\pi}\left[K^2 + \left(\frac{N\pi}{\lambda_g}\right)^2\right]^{1/2}, \tag{2.66}$$

where c is the speed of light, N is an integer and λ_g is the wavelength of the resonance mode in the cavity. Because the corrugation waveguide is normally over-mode, $\lambda_0 \simeq \lambda_g$ when $N = 2$. As mentioned earlier, the surface-impedance approach gives a good approximation when λ_0/p is a reasonably large value. Therefore, when designing the corrugation waveguide, the period p can be selected to be smaller than $\lambda_0/2$. It is of course the case that 'the smaller the period, the better'; however, as the operating frequency increases, the wavelength becomes smaller, resulting in a small corrugation period and a thin corrugation slot of $w \simeq 0$ which significantly increases the machining difficulty. The final choice of geometry should therefore also consider the machining tolerance.

Since $x_1' = kr_1 = \frac{2\pi r_1}{\lambda_0} \gg 1$ has to be satisfied, the corrugation waveguide radius r_1 is a large value. As the attenuation coefficient is proportional to r_1^{-3}, it is preferable to have a large r_1 at a given operating frequency. From equation (2.64), the waveguide radius affects the field strength if the input power is a fixed value. In a microwave undulator, a high field at the electron

beam path, in this case the waveguide center, is desired. Therefore, r_1 should be as small as possible under the constraint of $kr_1 >> 1$. On the other hand, it is preferred for the electron beam that travels through the microwave undulator to see a uniform field in the radial direction. The minimum waveguide radius can be solved from the field pattern of the operating mode if the electron beam aperture R_b and a threshold, for example, 90% of the maximum field at the beam edge, are defined. For HE_{1n} modes, it follows that $J_1(KR_b) = 0.9$. Taking the first two solutions of $J_0(Kr_1) = 0$, K is approximately equal to $2.4/r_1$ or $5.5/r_1$ for the HE_{11} or the HE_{12} mode, respectively. Therefore, the following parameters were chosen,

$$r_1 = \begin{cases} 3.8R_b, & \text{for the HE}_{11}\text{ mode} \\ 8.6R_b, & \text{for the HE}_{12}\text{ mode} \end{cases}$$

resulting in a reasonable value of r_1. Meanwhile, the value of r_1 should satisfy $x_1' = \frac{2\pi r_1}{\lambda_0} \gg 1$. If $x'_1 = 5$ is used, then $r_1 \geq 0.8\lambda_0$ and the results become

$$r_1 = \begin{cases} \text{maxima}(3.8R_b, 0.8\lambda_0), & \text{for the HE}_{11}\text{ mode} \\ \text{maxima}(8.6R_b, 0.8\lambda_0), & \text{for the HE}_{12}\text{ mode} \end{cases}.$$

2.2.1 The Corrugation Structure

An LC equivalent circuit can be established. Here the capacitive part of the surface reactance X_S (X_C) is a result of the wave passing through two parallel plates (corrugation walls) while the inductive part, X_L is a result of the circulation of the wave around the two parallel plates which are shorted at one end. This is represented in Fig. 2.23. It's important to emphasize that this physical model is a simplification of what really happens [18].

It is well known that in LC parallel circuits a resonant frequency ω_0 exists at which the inductive and capacitive reactance are equal in magnitude ($X_C = X_L$). Therefore, at the resonance frequency, the impedance will be minimal and equal to the ohmic resistance. The following equations (2.67) and (2.68) express as follows

$$\omega_0 = \frac{1}{\sqrt{LC}}, \tag{2.67}$$

$$\frac{1}{Z} = \sqrt{\frac{1}{R^2} + \left(\frac{1}{X_C} - \frac{1}{X_L}\right)^2}. \tag{2.68}$$

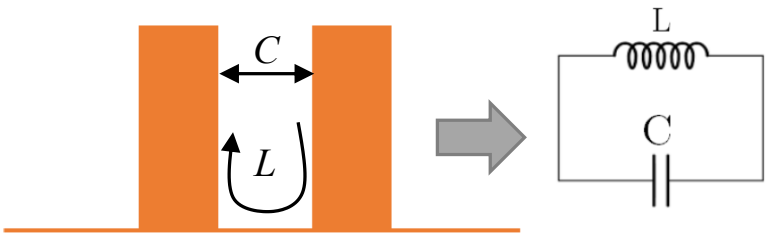

Figure 2.23 Equivalent LC parallel circuit of the corrugation structure.

It can be seen that in equation (2.68) if $X_L = X_C$ then $Z = R$. It can also be said that a limiting value of Z exists, given by the impedance of free space, which is a pure real resistance because in the vacuum there are no distributed charges (i.e., Z_0 = 119.9169832π Ω). If Z_0 is surpassed, the surface wave is liberated into the medium with a lower impedance. Thus, surface waves exist, when $\omega \rightarrow \omega_0 \Rightarrow Z_s \rightarrow \infty$, until a limiting value $Z_s \simeq 377\ \Omega$.

In this LC model, the surface impedance of the corrugation horn is given by

$$Z_S = \frac{j\omega L}{1-\omega^2 LC}. \tag{2.69}$$

Since its expression is $\phi = \arctan[(X_L - X_C)/R] = 0$, when $\omega = \omega_0$ the phase-shift is exactly $\pm$ 0 rad. A phase shift of $\pm\pi/2$ rad is given by purely inductive or capacitive reactance. This LC equivalent circuit describes the reality satisfactorily in the vicinity of the resonant frequency, i.e., $\omega_0 = 2\pi f_0$.

For a surface TM wave, by employing new Ampere's and Faraday's laws the following is derived

$$j\omega\varepsilon_0 E_z = \frac{\partial H_y}{\partial x} \tag{2.70}$$

$$j\omega\varepsilon_0 E_x = \frac{\partial H_y}{\partial z} \tag{2.71}$$

and

$$-j\omega\mu_0 H_y = \frac{\partial E_x}{\partial z} - \frac{\partial E_z}{\partial x}, \tag{2.72}$$

resulting in

$$E_x = -j\frac{\omega k_z}{k_x} C e^{-j(k_z z - k_x x + \omega t)}. \quad (2.73)$$

The combination of Maxwell's equations and equation (2.73) leads to the following expression of the wavevector in the u_z direction

$$k_z^2 = \mu_0 \varepsilon_0 \omega^2 + k_x^2, \quad (2.74)$$

and equation (2.74) leads, after some manipulation, to

$$k_z^2 = k_{TM}^2 = \frac{\omega^2}{c^2}\left(1 - \frac{Z_s^2}{Z_0^2}\right), \quad (2.75)$$

where $Z_0 = \sqrt{\mu_0/\varepsilon_0}$.

The analogous process for TE waves leads to the following expression for the wave vector

$$k_y^2 = k_{TE}^2 = \frac{\omega^2}{c^2}\left(1 - \frac{Z_0^2}{Z_s^2}\right), \quad (2.76)$$

where c is the speed of light.

Assuming a lossless case, from equation (2.75) it can be deduced that the propagation of TM surface waves is only possible when $Z_S^{TM} < Z_0$. From equation (2.76) it can be deduced that the propagation of TE surface waves is only possible when $Z_S^{TE} > Z_0$. It is possible to derive the phase difference between the incident and the reflected waves

$$\phi = Im\left\{ln\left(\frac{E^r}{E^i}\right)\right\} = Im\left\{\frac{Z_s - Z_0}{Z_s + Z_0}\right\}, \quad (2.77)$$

where Z_S is given by equation (2.69).

From equation (2.77) it can be deduced that when Z_S in a certain direction is low, the reflection phase (ϕ) of an incident wave is $\pm\pi$. While for increasing Z_S the value of ϕ tends to zero ($\phi \rightarrow 0$), and the critical value of Z_S is the medium impedance ($Z_S \rightarrow Z_0$).

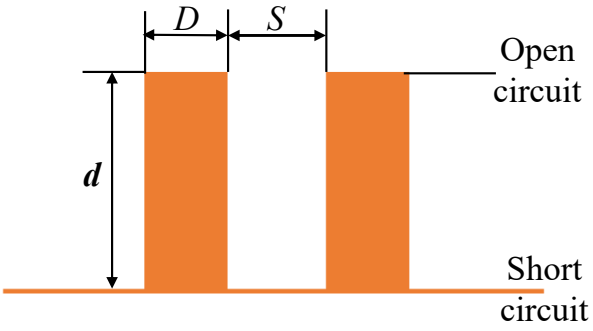

Figure 2.24 The configuration of the corrugation structure.

The configuration of the corrugation structure is shown in Fig. 2.24, where D represents the width of the corrugation, S is the spacing of the corrugation, and d is the depth of the corrugation. According to choke theory, the impedance of the corrugation is given by

$$Z_S = Z_C tan\beta l \tag{2.78}$$

The impedance of the corrugation is primarily controlled by the depth d of the corrugation.

2.3 Microstrip-to-Waveguide Transition

Various types of millimeter-wave transitions from waveguide to microstrip line have been proposed such as the ridge waveguide type, quasi-Yagi type, and planar waveguide type. About vertical transitions, a conventional type of probe feeding has a wideband characteristic, but it needs a metal short block with a quarter-wavelength on the substrate. The replacement of the metal short block is a patch element in the waveguide to achieve sufficient coupling between the waveguide and microstrip line. In addition, the proximity coupling type has been developed more recently. It can be composed of a single dielectric substrate attached to the waveguide. A rectangular patch element on the lower plane of the dielectric substrate couples with a microstrip line on the upper plane of the dielectric substrate.

2.3.1 Prob Transition with Back-Short

Transitions with a short-circuited waveguide of 1/4 guided wavelength on the substrate are very popular [19] because their principle of mode transformation is almost the same as that of ordinary transitions of a waveguide and a coaxial cable [20]. Probe transition connects a microstrip line and a waveguide as shown in Fig. 2.25. A probe at one end of the microstrip line is inserted into the perpendicular waveguide whose one end is short-circuited by the back-short

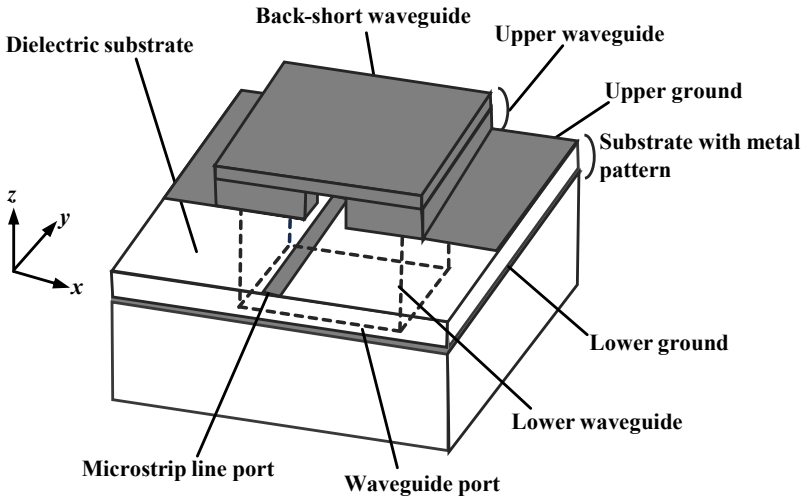

Figure 2.25 Probe transition with back-short.

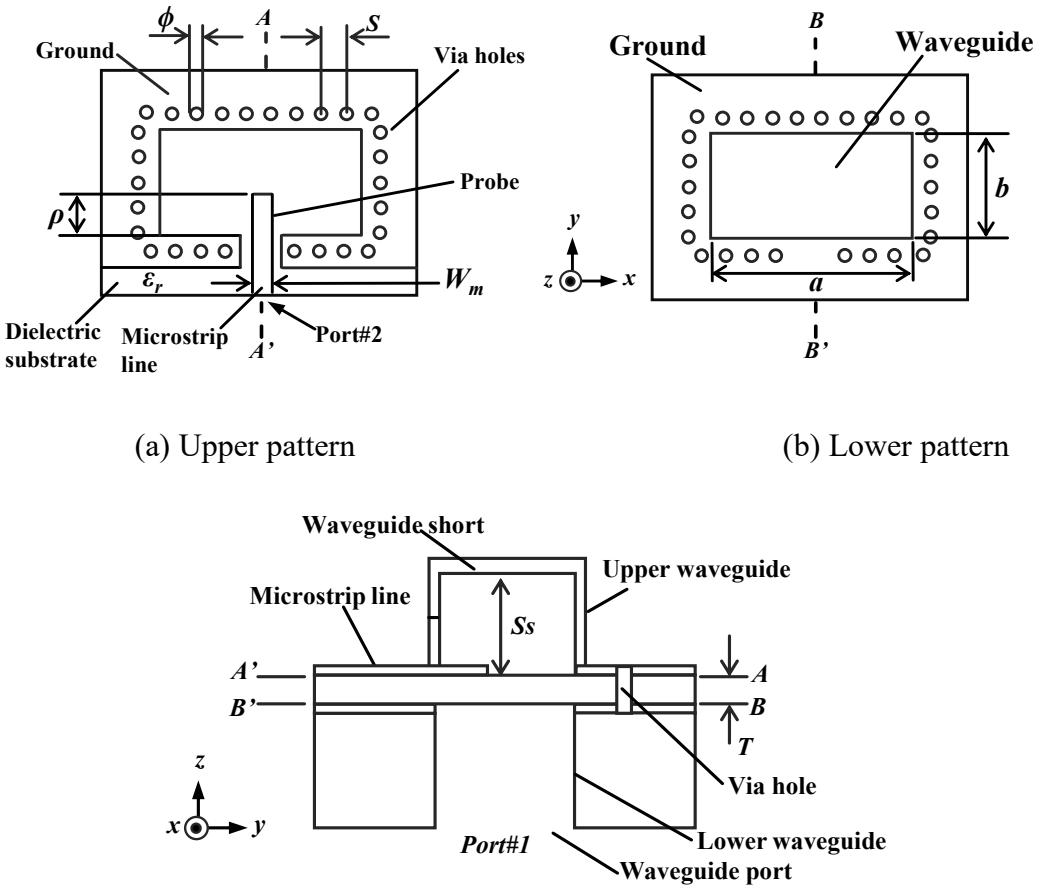

(a) Upper pattern (b) Lower pattern

(c) Sectional view in yz-plane

Figure 2.26 Detailed configuration of probe transition with back-short.

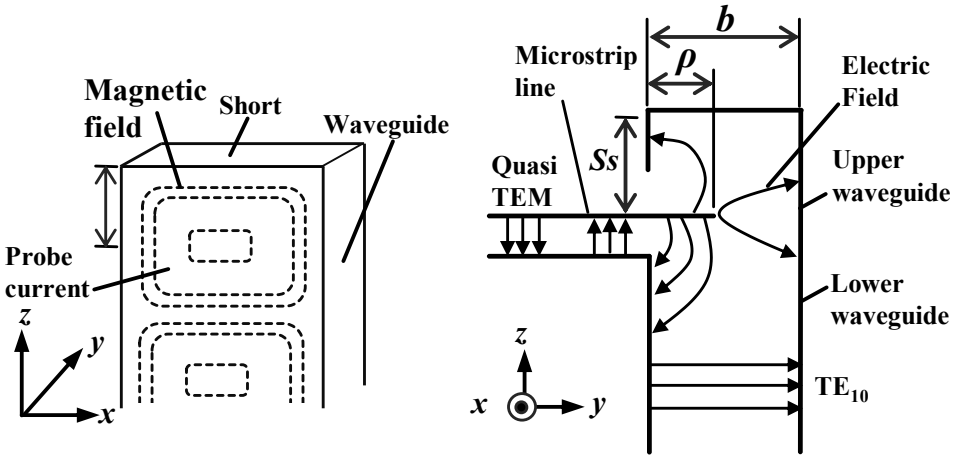

(a) Magnetic field distribution in xz-plane (b) Electric field distribution in yz-plane

Figure 2.27 Magnetic and electric field lines.

waveguide. The configuration is shown in Fig. 2.26. A dielectric substrate with conductor patterns on its both sides is placed on an open-ended waveguide (WR-12 standard waveguide). An aperture of the dielectric substrate is covered with an upper waveguide. A short circuit of the upper waveguide is essentially $\lambda_g/4$ (λ_g: guided wavelength of the waveguide) above the substrate. Consequently, the electric current on the probe couples to the magnetic field of the TE_{10} dominant mode of the waveguide as shown in Fig. 2.27. Via holes are surrounding the waveguide in the structure in order to reduce leakage of parallel plate mode transmitting into the substrate. Impedance matching could be achieved by controlling the length S_s of the probe and the length S_s of the upper waveguide.

2.3.2 Planar Proximity Coupling Transition

Planar proximity coupling transitions shown in Fig. 2.28 and Fig. 2.29 have been proposed [21]. This transition can be composed of only a single dielectric substrate attached to the waveguide end and is suitable for mass production. The conductor pattern with a notch (it is named a waveguide short pattern because of its function) and the microstrip line are located on the upper plane of the dielectric substrate. A rectangular patch element and a surrounding ground are patterned on the lower plane of the dielectric substrate. Via holes are arranged surrounding the aperture of the waveguide on the lower plane of the dielectric substrate to connect the surrounding ground and the waveguide short electrically. The microstrip line is inserted into the waveguide profile and the line overlaps the rectangular patch element with an overlap length ρ.

The electric field distribution of mode conversion in the transition is shown in Fig. 2.30. The dominant modes of the waveguide, the rectangular patch, and the microstrip line are TE_{10}, TM_{01} fundamental resonant mode, and quasi-TEM fundamental transmission mode, respectively. The electromagnetic fields of TE_{10} mode in the waveguide excite the TM_{01} mode of the patch element, followed by an electromagnetic coupling from the patch and quasi-TEM mode of the microstrip line. Consequently, power is transmitted from the waveguide into the microstrip line.

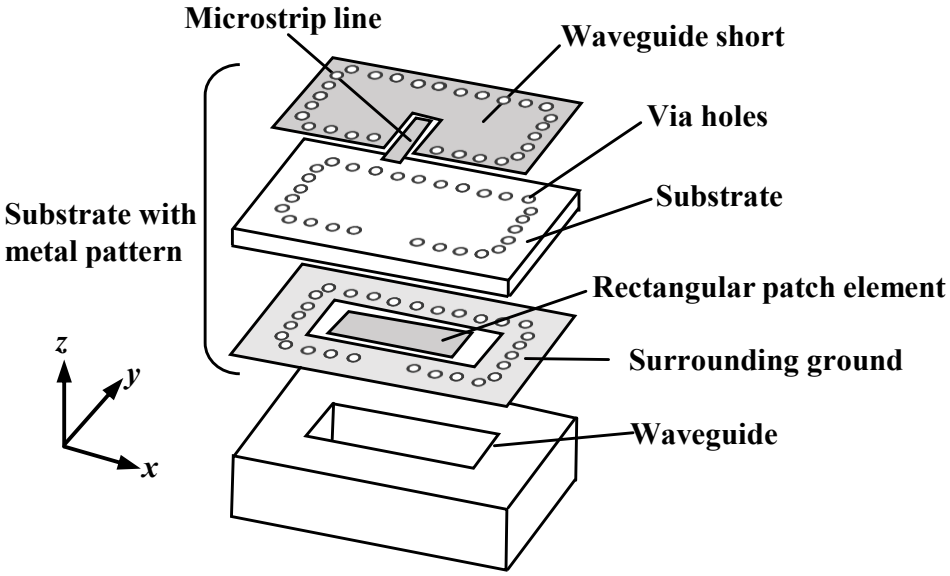

Figure 2.28 Planar proximity coupling transition.

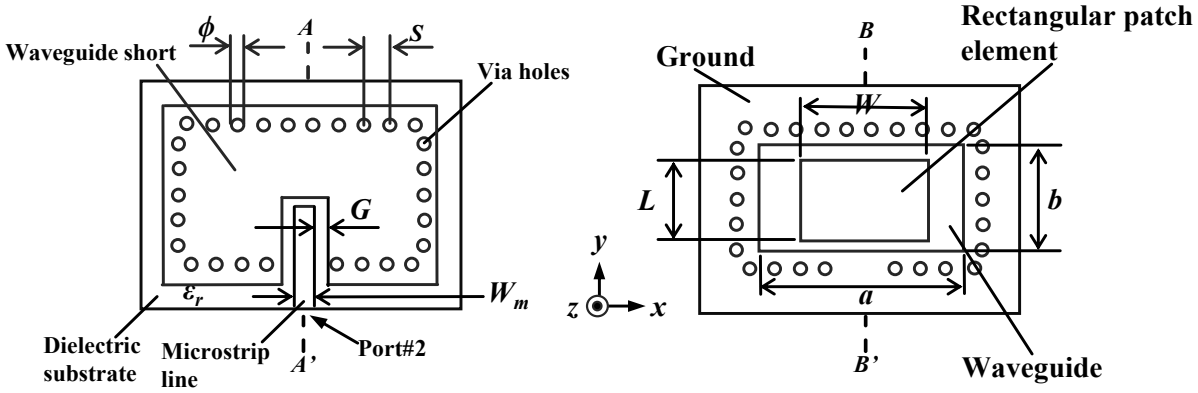

(a) Upper pattern (b) Lower pattern

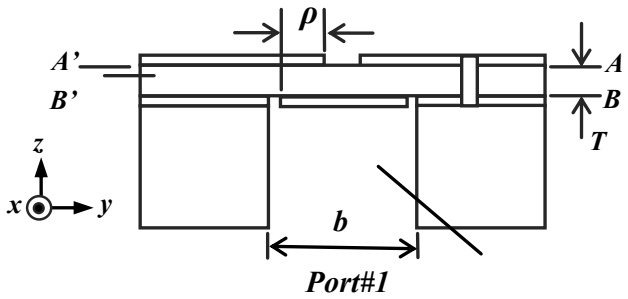

(c) Sectional view in yz-plane

Figure 2.29 Detailed configuration of planar proximity coupling transition.

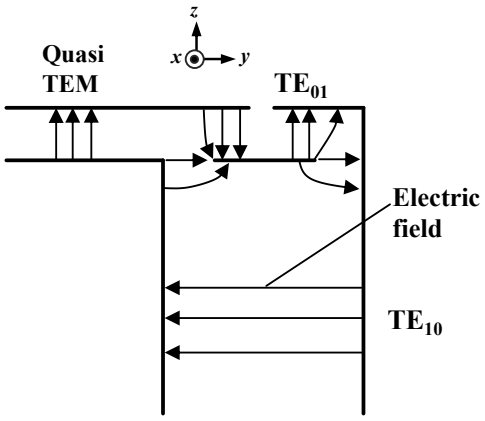

Figure 2.30 Electric field lines of each mode in planar proximity coupling transition.

2.3.3 Coplanar Waveguide-to-Rectangular Waveguide Transition

An overall picture of a new CPW-to-rectangular waveguide transition is depicted in Fig. 2.31, while cross-sections are shown in Fig. 2.32. In the transition, a dielectric substrate with a CPW circuit is centered in the *E*-plane of a full-height rectangular waveguide in line with the propagation direction of the waveguide as shown in Fig. 2.32 (a). The waveguide mode coming through the waveguide port on the left-hand side is coupled to the CPW with an -plane probe, as usually done in stripline or microstrip line transitions. However, in those transitions, the substrate protrudes into the waveguide through the broad wall. This figure shows the transition with a rectangular probe. Nonetheless, probes having different shapes can be employed as well, e.g., circular or radial.

The probe is formed by a 90 extension of the center conductor of the CPW as shown in Fig. 2.32 (b). The CPW is placed close by one of the broad walls in order to maintain the field distribution in the substrate-containing waveguide section as uniformly as possible. One of the ground planes forms a short plane into the waveguide at a distance l_1 to prevent the TE_{10} mode propagation toward the CPW port. The end of the substrate on the waveguide side can be extended to a distance l_2 from the probe to act as an impedance transformer between the waveguide and probe. The CPW dimensions (center conductor width w, ground-to-ground spacing d) and the distance to the waveguide wall were chosen so that the CPW is electrically only slightly asymmetrical, i.e., the fields are concentrated near the CPW slots and, thus, the waveguide wall does not affect. The CPW can be made fully symmetrical by, e.g., bringing it gradually to the center of the waveguide, which would provide a uniform transition, or by using a special CPW housing.

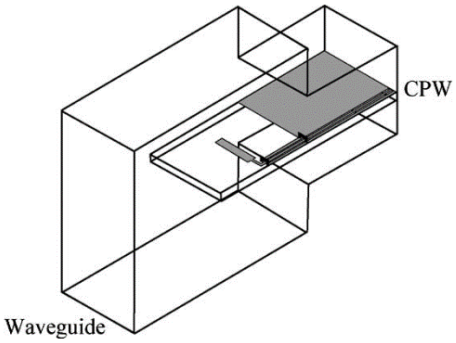

Figure 2.31 Overall picture of the new CPW-to-rectangular waveguide transition.

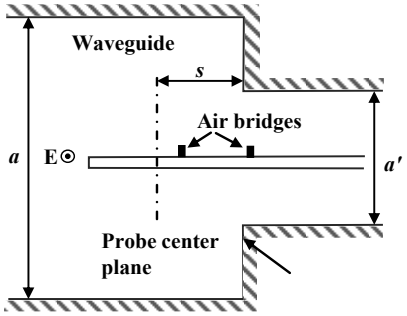

(a) Side view

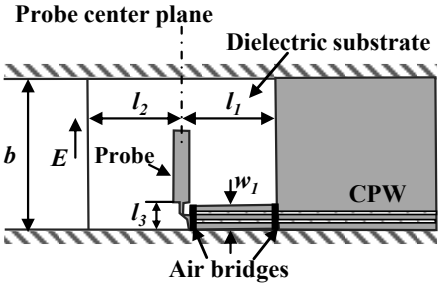

(b) Top view

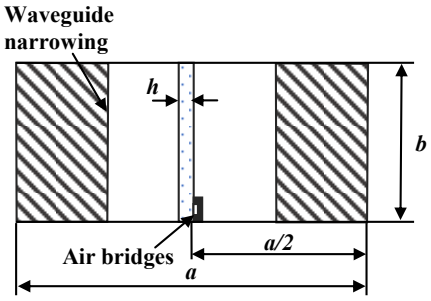

(c) End view

Figure 2.32 Cross-sectional views of the new CPW-to-rectangular waveguide transition.

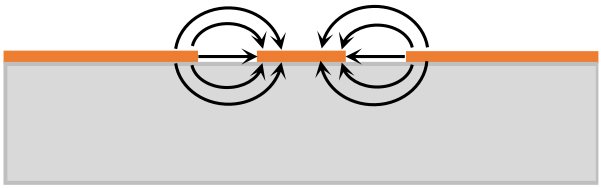

(a)

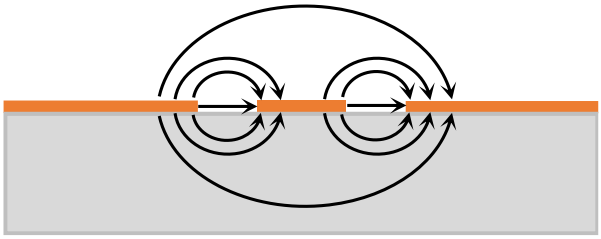

(b)

Figure 2.33 Modes of the CPW (a) CPW mode (b) CSL mode.

Two dominant modes can propagate in the CPW; a CPW and coupled slot line (CSL) mode as shown in Fig. 2.33. In order to prevent the propagation of the CSL mode potentially excited by any discontinuity, we have used air bridges and a CPW housing, as shown in Figs. 2.32 (a) and (c).

2.3.4 Narrow-Wall Connected Microstrip-to-Waveguide Transition

In some applications, the narrow-wall-connected microstrip-to-waveguide transition is required. Refer to the former developed proximity coupling type transition [21], the microstrip line is located on the waveguide broad-wall and the microstrip line probe is parallel to the E-plane of the waveguide, therefore, current on the rectangular patch element couples to the microstrip line efficiently. However, on the occasion of the microstrip line on the narrow-wall of the waveguide, the microstrip line probe is orthogonal to the E-plane of the waveguide. Therefore, they do not couple essentially. To couple currents on the microstrip line and the patch element, a V-shaped patch element is applied instead of the rectangular patch element.

Narrow-wall-connected microstrip-to-waveguide transition using V-shaped patch element in millimeter-wave band was proposed [22]. Since the microstrip line on the narrow wall is perpendicular to the E-plane of the waveguide, the waveguide field does not couple directly to the microstrip line. The current on the V-shaped patch element flows along the inclined edges, and then the current on the V-shaped patch element couples to the microstrip line efficiently.

Three types of transitions are investigated. *S*-parameters of the reflection S_{11} and the transmission S_{21} are calculated by using an electromagnetic simulator based on the finite element method (ANSYS HFSS). The numerical investigations of these transitions show some relations between the bandwidth and the insertion loss. It is confirmed that the improved transition exhibits an insertion loss of 0.6 dB from 76 to 77 GHz and a bandwidth of 4.1 % (3.15 GHz) for the reflection coefficient below −15 dB.

The configuration of the transition is shown in Fig. 2.34 and Fig. 2.35. The microstrip line and the waveguide short are located on the upper plane of the dielectric substrate. The V-shaped patch element and the surrounding ground are patterned on the lower plane of the dielectric substrate. Via-holes surround the aperture of the waveguide on the lower plane of the substrate to connect the surrounding ground and the waveguide short electrically. The design frequency range is from 76 GHz to 77 GHz. The V-shaped patch element is designed as follows. Refer to the conventional proximity coupling type [21], the current on the rectangular patch element has only the *y*-component which is parallel to the E-plane of the waveguide shown in Fig. 2.36(a). In this case, the current on the rectangular patch element is parallel to the microstrip line, therefore, the current on the rectangular patch element couples to the microstrip line. On the

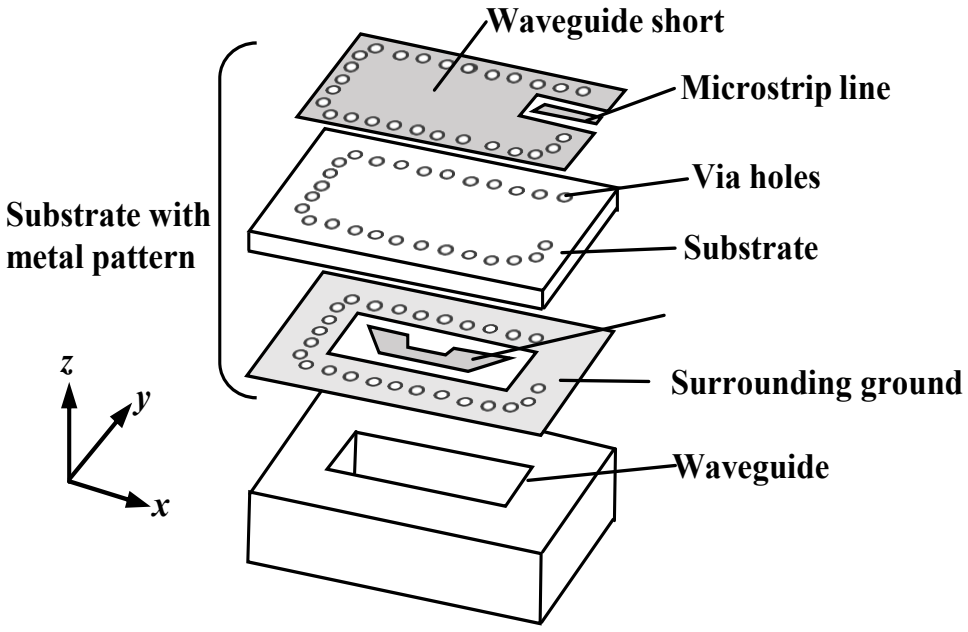

Figure 2.34 Configuration of transition.

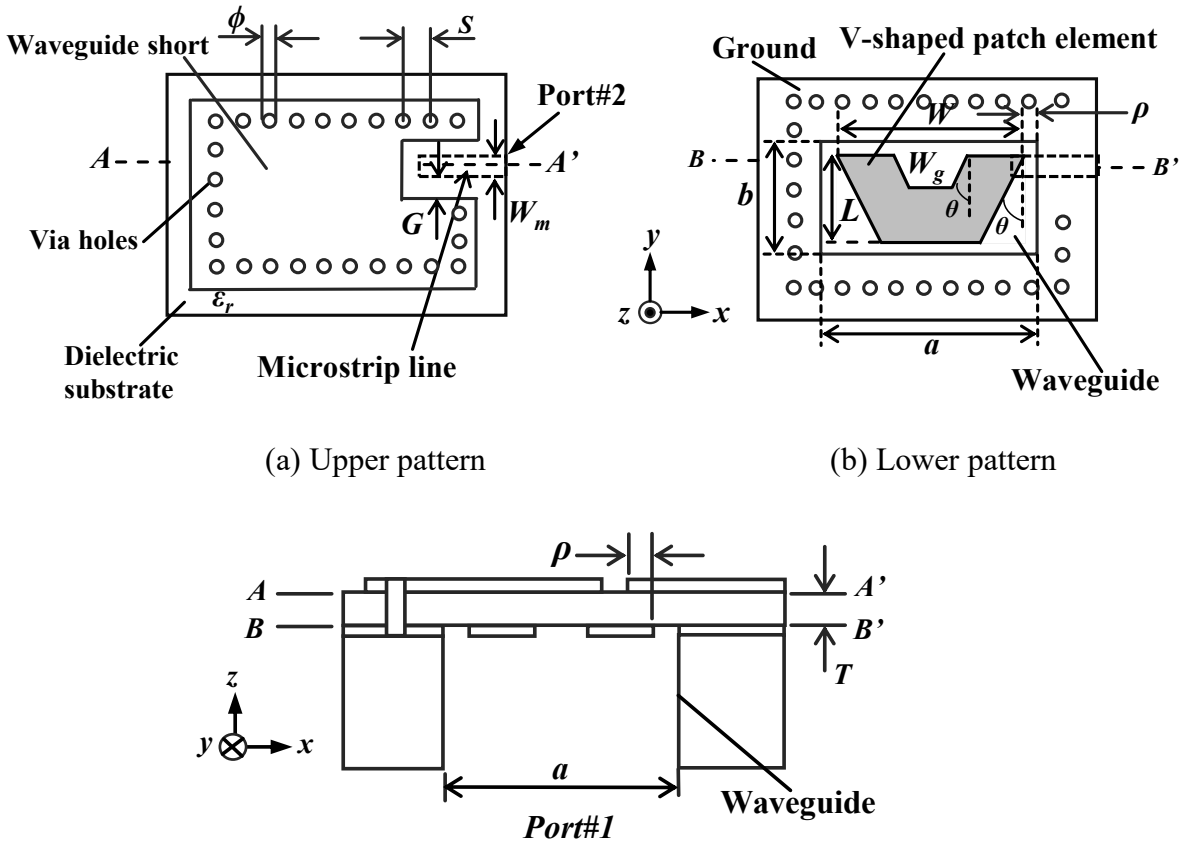

(a) Upper pattern

(b) Lower pattern

(c) Cross-section view

Figure 2.35 Detail configuration of transition.

other hand, the current on the patch element which is excited by the electromagnetic field in the waveguide must have both of *x*-component and *y*-component in order to couple to the microstrip line on the waveguide narrow-wall. The current on the V-shaped patch element is divided into two directions along the side edge as shown in Fig. 2.36 (b). Consequently, the current on the V-shaped patch element creates a parallel component with the microstrip line, and effective coupling is achieved with the microstrip line.

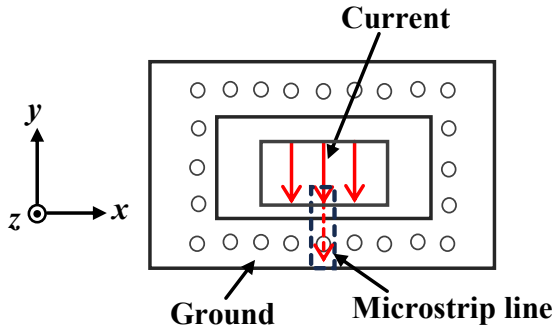

(a) Current on rectangular patch

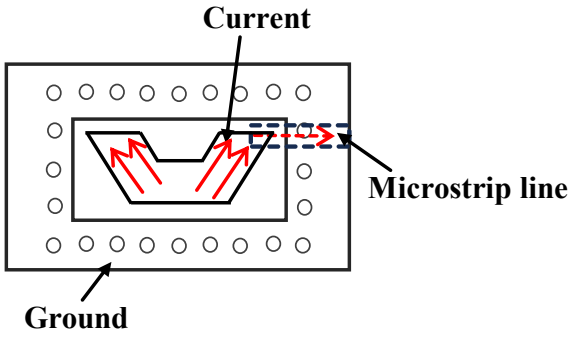

(b) Current on V-shaped patch

Figure 2.36 Current distributions on patch element.

2.4 Substrate Integrated Waveguide-to-Waveguide Transition

Substrate integrated waveguide (SIW), a low-profile type of waveguide realized on substrate, has become more and more popular in recent years. Various kinds of microwave and millimeter-wave integrated circuits such as filters, oscillators, and antennas have been and are being realized in SIW structure. The SIW circuits feature the merits of low-loss, low radiation, small size, and easy fabrications. In many cases, SIW can completely replace the rectangular waveguide for any circuit function. However, waveguide may be still an important transmission line in microwave/millimeter wave circuit design, and in particular, a large number of commercial and existing products are in waveguide format. Moreover, compared with SIW techniques, waveguide structures can be used to design devices with much better power handling capability, more structure rigidity, and more geometrical flexibility for 3D structures and extensions. Thus, we can anticipate that the hybrid design of planar structures such as microstrip lines, CPW lines, and SIW with the conventional waveguides in microwave/millimeter-wave circuits/systems could be unavoidable. Therefore, transitions between various types of transmission lines are necessary.

The transitions between different types of transmission lines have been studied by using the height-tapered waveguide geometry is bulky and tedious. Also, an alternative compact transition transfers microwave energy between an air-filled waveguide and SIW through a rectangular aperture which has the same size as the inner cross-section of the air-filled waveguide.

Fig. 2.37 depicts the example of the transition structure from SIW to RWG [23], in which the SIW and the RWG intersect vertically in geometry. As shown in the figure, the substrate of SIW is easily surface-mounted to the standard flange of the waveguide by creating a flange on the substrate. Thus, the connection between the waveguide circuit and the SIW circuit is straightforward. A longitudinal slot window is etched on the broad wall of SIW (the top surface of SIW), which couples energy between the two transmission lines. The slot has a length of half wavelength and a small offset to the centerline of SIW. The slot in this transition is similar to the slot antenna. Through the slot, the incident wave in SIW is radiated into the RWG. A short circuit is placed at the end of the SIW line. The distance between the short circuit and the center of the slot is 3 quarter-wavelengths (can be any odd times of quarter-wavelength) so that the circuit acts as an open circuit at the plane of the center of the slot. On the RWG side, the slot is located at the center of the RWG line.

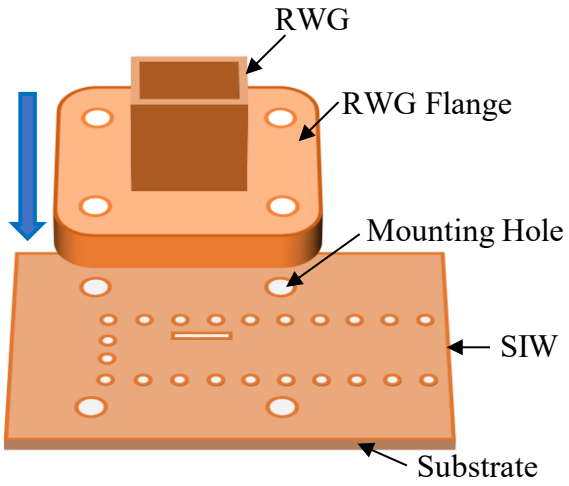

Figure 2.37 The transition between rectangular waveguide and SIW.

In addition, to obtain a broadband waveguide-to-SIW transition is in the development of the SIW in any layer of a multi-layer substrate [24]. The E-plane SIW in a multi-layer dielectric substrate has been proposed for leakage loss reduction. The utilization of thin dielectric substrates can control the cutoff frequency of E-plane SIW and significantly reduce leakage power. Copper foils at middle metal patterns will cut the power leakage of horizontal polarization between via-holes. The configuration of the E-plane SIW in multi-layer dielectric substrate is demonstrated in Fig. 2.38. The E-plane SIW is a stacked SIW consisting of multiple dielectric substrates bonded by a bonding film. Two rows of via-hole are arranged in parallel and penetrated through the multilayer substrate so that the waveguide is formed in the dielectric substrates. The substrates are NCP-H220A with thickness *t*, dielectric constant ε_r = 2.19, and loss tangent tan δ = 0.0006. The bonding film thickness is 35 μm with a dielectric constant ε_r = 2.4, and loss tangent tan δ = 0.018. The broad wall width of the E-plane SIW is the total thickness of the dielectric substrates including the thickness of the metal patterns (18 μm) and the bonding films. The narrow wall width *b* is the distance between the metal patterns in the E-plane SIW waveguide. The E-plane SIW is formed by drilling through holes in a printed circuit board and arranging them in two rows at a fixed interval. When the diameter of a via-hole is ϕ, the condition for pitch *c* of via-holes is $c/\phi \geq 2$.

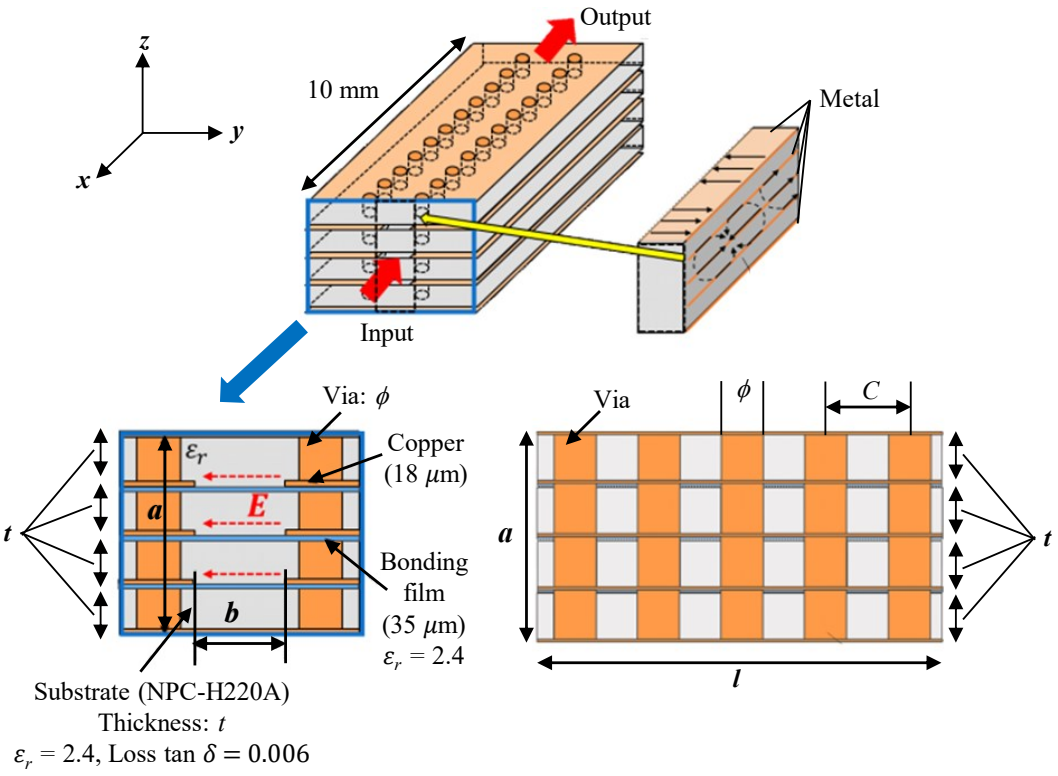

Figure 2.38 E-plane SIW in multilayer substrate configuration.

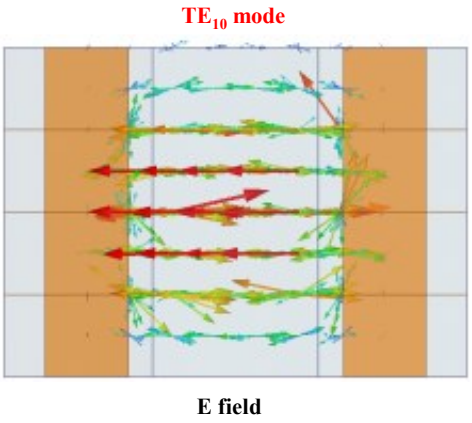

Figure 2.39 Electric field distributions in E-plane SIW.

The principle operation of the E-plane SIW is described. Unlike the commonly used H-plane SIW, the TE_{10} mode of the E-plane SIW is horizontally polarized as shown in Fig. 2.40. With single layer substrate structure, the polarization in the x-axis direction (waveguide propagation direction) cannot be cut off between the via holes, resulting in leakage loss. The

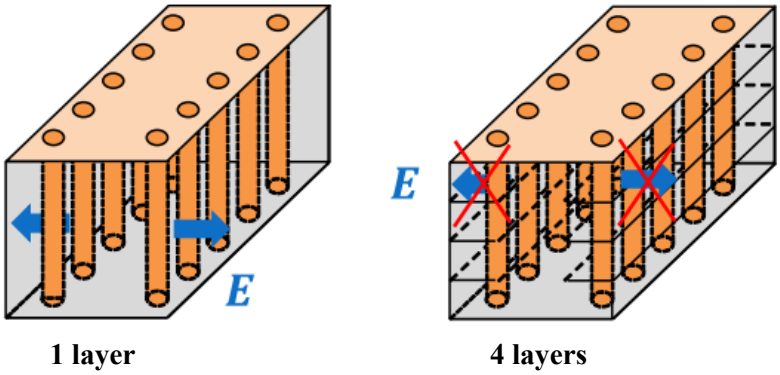

Figure 2.40 Leakage loss in E-plane SIW.

leakage loss between via holes of the E-plane SIW is described in Fig. 2.40. When multiple layers of metal patterns are placed inside, and the metal pattern spacing t is less than half the wavelength in the SIW, the polarization that contributes to the leakage loss due to the TE_{10} mode can be cut off. Therefore, the via-hole rows between the layers act as metallic walls, and the TE_{10} mode propagates without leakage and with low loss. However, due to the influence of higher-order modes, leakage loss cannot be completely prevented.

References

[1] N. Marcuvitz, Waveguide Handbook, IEE Press, 1986.

[2] David M. Pozar, Microwave Enginering Third Edition, Willy, 2005.

[3] W. Hilberg, “From approximations to exact relations for characteristic impedances,” *IEEE Trans. Microw. Theory Tech.*, vol. 17, no. 5, pp. 259–265, May 1969.

[4] M. Houdart, “Coplanar lines : Application to broadband microwave integrated circuits,” *in 6th European Microw. Conf.*, pp. 49–53, Sep. 1976.

[5] J. Hinojosa, “S-parameter broadband measurements on-coplanar and fast extraction of the substrate intrinsic properties,” *IEEE Microw. Wireless Compon. Lett*., vol. 11, no. 2, pp. 80–82, Feb. 2001.

[6] G. Ghione and C. U. Naldi, “Coplanar waveguides for MMIC applications; effect of upper shielding, conductor backing, finite-extent ground planes, and line-to-line coupling,” *IEEE Trans. Microw. Theory Tech*., vol. MTT-35, no. 3, pp. 260–267, Mar. 1987.

[7] R. A. Pucel and D. J. Masse, “Microstrip propagation on magnetic substrates–Part 1: Design theory,” *IEEE Trans. Microw. Theory Tech*., vol. MTT-20, no. 5, pp. 304–308, May 1972.

[8] I. Bahl and R. Garg, “A designer’s guide to stripline circuits,” *Microwaves*, pp. 90–96, 1978.

[9] S. Cohn, “Problems in strip transmission lines,” *IRE Trans. Microw. Theory Tech*., vol. 3, no. 2, pp. 119–126, Mar. 1955.

[10] S. B. Cohn, “Characteristic impedances of broadside-coupled strip transmission lines,” *IRE Trans. Microw. Theory Tech.*, vol. 8, no. 6, pp. 633–637, Jun. 1960.

[11] H. Howe, Stripline Circuit Design, 4th Edition (Artech, Dedham, MA, 1982); P.C.L. Yip, High Frequency Circuit Design and Measurements (Chapman and Hall, London, 1980).

[12] Hall, S.H.; Heck, H.L. Advanced Signal Integrity for High-Speed Digital Design; John Wiley & Sons: New York, NY, USA, 2009; pp. 297–314.

[13] A. O. Nwajana, and K. S. K. Yeo, "Practical Approach to Substrate Integrated Waveguide (SIW) Diplexer: Emerging Research and Opportunity", 1st ed.; IGI Global: Hershey, PA, USA, 2020; pp. 1–171.

[14] F. Xu, and K. Wu, "Guided-wave and leakage characteristics of substrate integrated waveguide" *IEEE Trans. Microw. Theory Tech*., vol. 53, pp. 66–73, 2005.

[15] K. C. Gupta, R. Garg, and I. J. Bahl, Microstrip Lines and Slotlines, Artech House, Dedham, Mass., 1979.

[16] E. J. Kowalski, D. S. Tax, M. A. Shapiro, J. R. Sirigiri, R. J. Temkin, T. S. Bigelow, and D. A. Rasmussen, "Linearly polarized modes of a corrugated metallic waveguide," IEEE Trans. Microw. Theory Techn., vol. 58, no. 11, pp. 2772–2780, Nov. 2010.

[17] L. Zhang, et al., "Systematic study of a corrugated waveguide as a microwave undulator," Journal Synchrotron. Radiaion, vol. 26, pp. 11-17, 2019.

[18] J. De Miguel-Hernández, and R.J. Hoyland, "Fundamentals of horn antennas with low cross-polarization levels for radioastronomy and satellite communications," Hoyland 2019 JINST 14, doi: 10.1088/1748-0221/14/08/R08001.

[19] Y. Leong and S. Weinreb, "Full band waveguide to microstrip probe transitions," *IEEE MTT-S Int. Microw. Symp. Dig.*, Anaheim, CA, May 1999, vol. 4, pp. 1435-1438.

[20] I. J. Bahl and D. K. Trivedi, "A Designer's Guide to Microstrip Line," *Microwaves*, pp. 174-182, May 1977.

[21] H. Iizuka, T. Watanabe, K. Sato, and K. Nisikawa, “Millimeter-wave microstrip line to waveguide transition fabricated on a single layer dielectric substrate,” *IEICE Trans. Commun.*, vol. E85-B, no. 6, pp. 1169-1177, Jun. 2002.

[22] Iizuka, H, Sakakibara, K, & Kikuma, N. Millimeter-Wave Transition From Wave-guide to Two Microstrip Lines Using Rectangular Patch Element,” *IEEE Trans. Microw. Theory Tech*., May 2007, doi: TMTT.2007.895139, 55(5), 899-905.

[23] K. Seo, K. Sakakibara, and N. Kikuma, “Narrow-Wall-Connected Microstrip-to-Wave-guide Transition Using V-Shaped Patch Element in Millimeter-Wave Band,” *IEICE Trans. Commun*., vol E93-B, np 10, pp. 2523-2530, Oct. 2010.

[24] Li, L., et al., “A transition from substrate integrated waveguide (SIW) to rectangular waveguide,” Proceedings of the 2009 Asia Pacific Microwave Conference, Singapore (2009).

[25] S. Kishi, K. Sakakibara, Y. Sugimoto, T. Morioka, J. Kim, and N. Kikuma, “274-GHz Substrate-Integrated-Waveguide Fed Rotman Lens Multibeam Antenna Integrated in Multi-layer Substrate,” 2023 International Symposium on Antennas and Propagation (ISAP2023), Oct. 30-Nov. 2, Kuala Lumpur.

Chapter 3

Broad-Wall-Inserted Planar-Line-to-Waveguide Transition in Multi-layer Substrates

This chapter introduces a broadband broad-wall-inserted planar-line-to-waveguide transition designed for sub-terahertz frequencies within multi-layer substrates. It encompasses both single-end line-to-waveguide and differential-line-to-waveguide transitions. The single-end line-to-waveguide transition employs grounded suspended coplanar waveguide (GSCPW) and grounded coplanar waveguide (GCPW) configurations for feeding, while the differential-line-to-waveguide transition utilizes GCPW. The characteristics of these transitions are analyzed through electromagnetic simulations employing the finite element method and validated through experimental measurements within the WR-3 band (220 GHz-320 GHz). The measured performances substantiate the feasibility of the multi-layer broad-wall-inserted planar-line-to-waveguide transition, indicating its suitability for practical sub-terahertz systems.

3.1 GSCPW-to-Waveguide Transition in Multi-layer Substrates

This section proposes a GSCPW-to-waveguide transition designed on a multi-layer dielectric substrate with a patch at 275 GHz. However, the transmission drops at a particular frequency due to the resonance among the apertures on Layer 2 to Layer 8. Therefore, the corrugation structure is applied to Layer 5 to cut the electric current and improve transmission [1].

3.1.1 Configuration of the GSCPW-to-Waveguide Transition

The GSCPW-to-waveguide transition is designed to be composed of WR-3 waveguide and multilayer substrates with HL972LF-LD [2] three prepreg layers on both sides of a core layer. The prepreg and the core substrates with a dielectric constant (ε_r) of 3.5 and loss tangent tan δ = 0.003 have thicknesses of 30 μm and 100 μm, respectively. Concurrently, it has eight copper layers with a thickness of 15 μm. The feeding GSCPW is inserted into the waveguide on Layer 2 of the dielectric substrate which forms the back-short type transition, as shown in Fig. 3.1 (a).

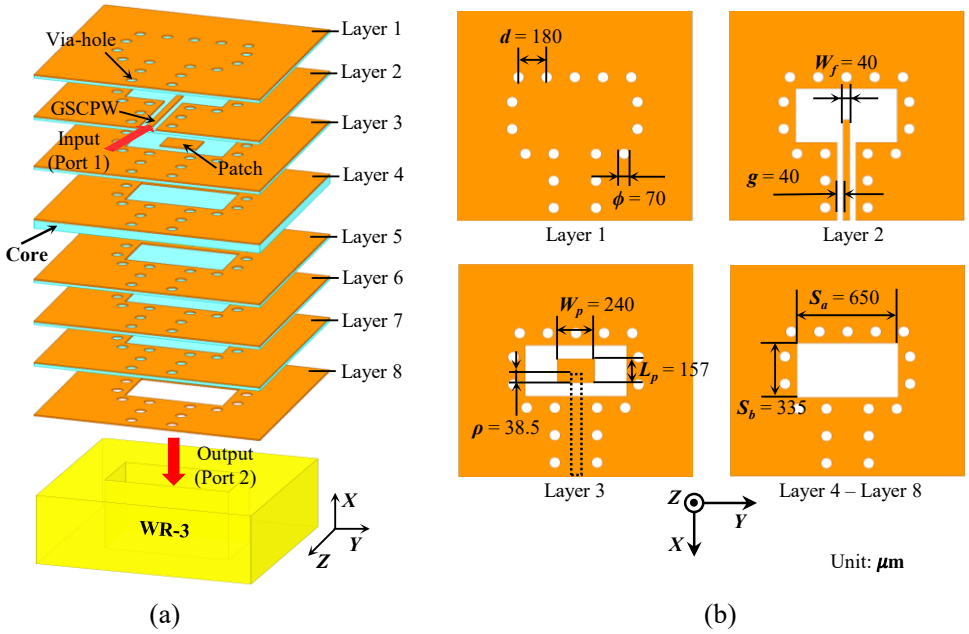

Figure 3.1 Configuration of the GSCPW-to-waveguide transition (a) 3D overview and (b) Top views of each layer with the parameters.

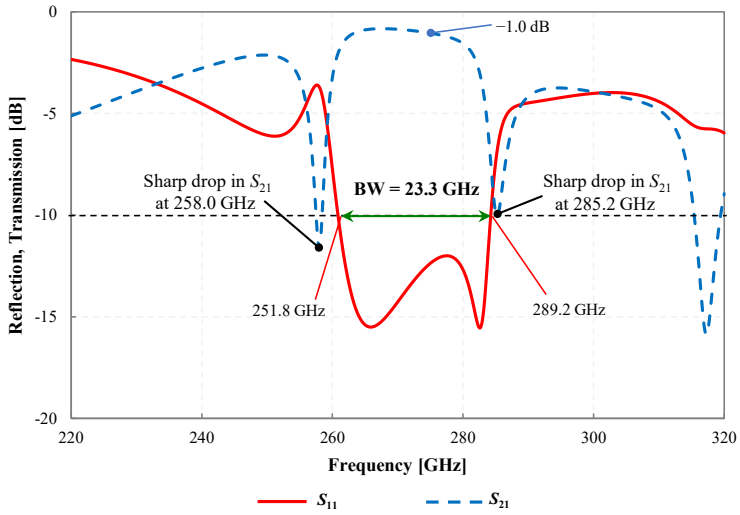

Figure 3.2 Simulation results of scattering parameters of the GSCPW-to-waveguide transition.

The electric current at the end of the signal line is coupled to the patch on Layer 3. The patch radiates toward the hollow waveguide through the lower dielectric layers. The via-holes are arranged to prevent leakage of the parallel plate mode in the substrates. The patch length is designed to set the operational frequency at 275 GHz. The metal patterns of each layer with their respective parameters are depicted in Fig. 3.1 (b). The simulation results of the GSCPW-to-waveguide transition using these optimized parameters are shown in Fig. 3.2. The frequency bandwidth for the reflection coefficient less than −10 dB spans from 261.0 GHz to

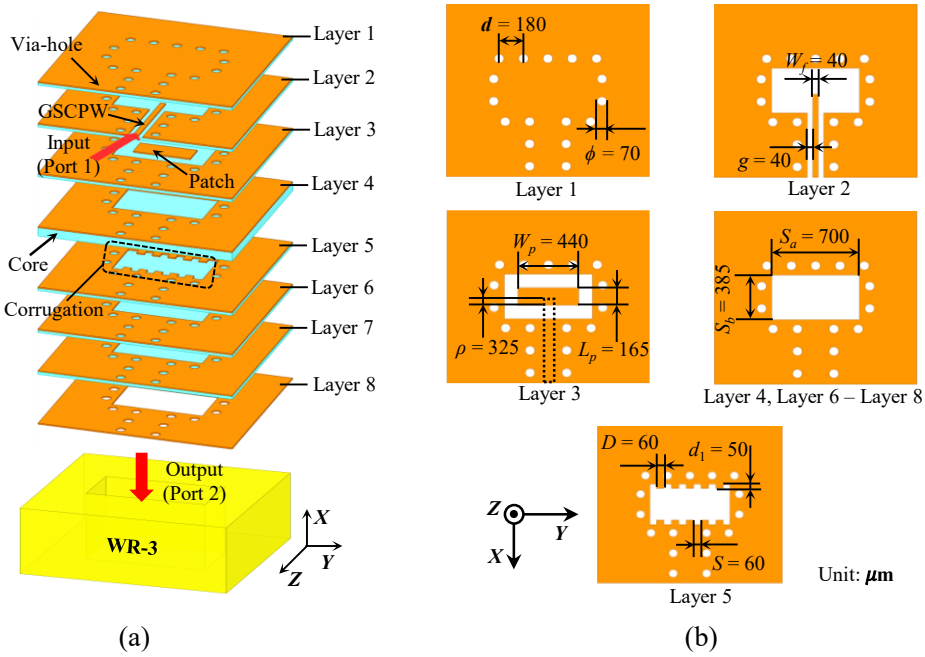

(a) (b)

Figure 3.3 Configuration of the GSCPW-to-waveguide transition with corrugation structures (a) 3D overview and (b) Top views of each layer with the parameters.

284.3 GHz, resulting in a bandwidth of 23.3 GHz (8.5%). Also, at the center frequency of 275 GHz, the transmission coefficient was −1.0 dB. It shows a narrow bandwidth characteristic was observed due to the drop in S_{21} at 258.0 GHz and 285.2 GHz. The transmission coefficient sharply drops at a particular frequency due to the resonance among the apertures on Layer 2 to Layer 8.

Therefore, the corrugation structure with a quarter-guided wavelength is applied at the middle layer to reduce the resonance in the substrate and improve the transmission characteristic. The configuration of the GSCPW-to-waveguide transition with corrugation structures is shown in Fig. 3.3 (a). The metal patterns of each layer with parameters are depicted in Fig. 3.3 (b).

3.1.2 Study Parameters of the GSCPW-to-Waveguide Transition

This subsection examines the reflection characteristics of the GSCPW-to-waveguide transition with corrugation structures based on simulated parameters. The transition's numerical analysis is conducted using the finite-element method ANSYS HFSS [3]. The objective is to broaden the resonance bandwidth to achieve a reflection coefficient of less than −10 dB. A parameter simulation was executed to investigate the crucial elements of the

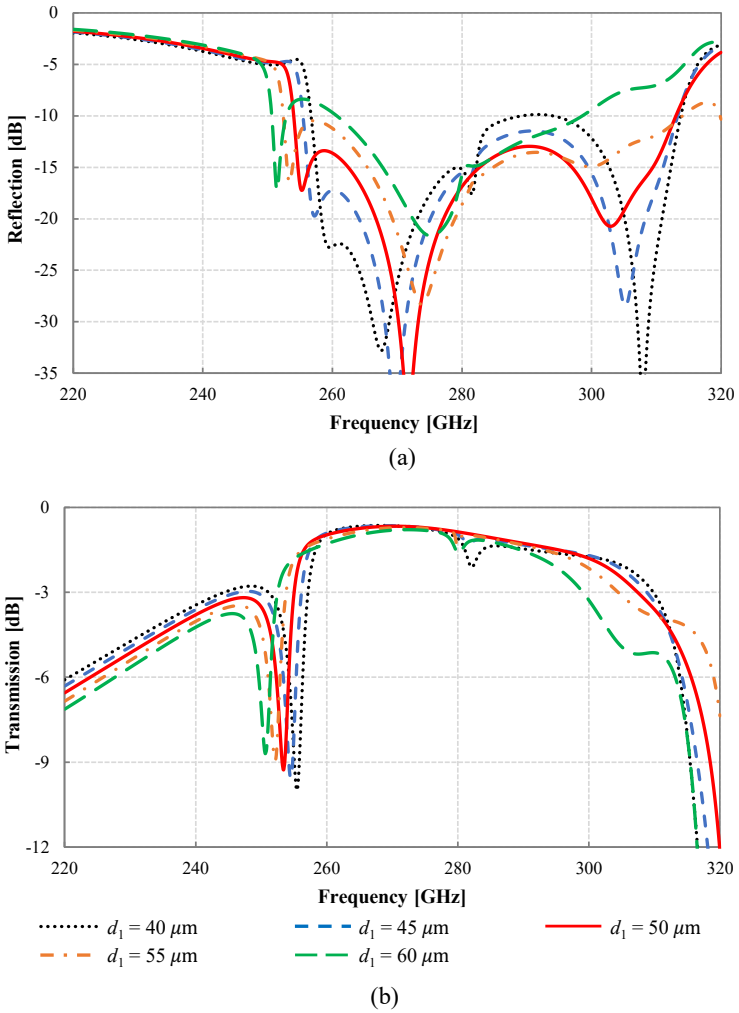

Figure 3.4 Reflection characteristics of the GSCPW-to-waveguide transition with corrugation structures depend on d_1 (a) reflection coefficient and (b) transmission coefficient.

transition's wideband design. The critical parameters of the transition were scrutinized to achieve wideband operation. The length of the rectangular patch (L_P) is a crucial parameter for controlling the resonant frequencies, while the width of the rectangular patch (W_P) governs impedance matching. Additionally, the corrugation depth (d_1) influences the transmission coefficient and bandwidth. These parameters collectively determine the resonant frequency, thereby impacting the enhanced bandwidth.

Fig. 3.4 shows the scattering parameters from the simulation with the sweep depth d_1 of the corrugation. The d_1 affects the transmission coefficient and bandwidth. The sharp drop in the transmission coefficient was improved when d_1 was 50 μm, and the bandwidth was increased in the high-frequency range. As d_1 decreases, the reflection coefficient level at lower resonant

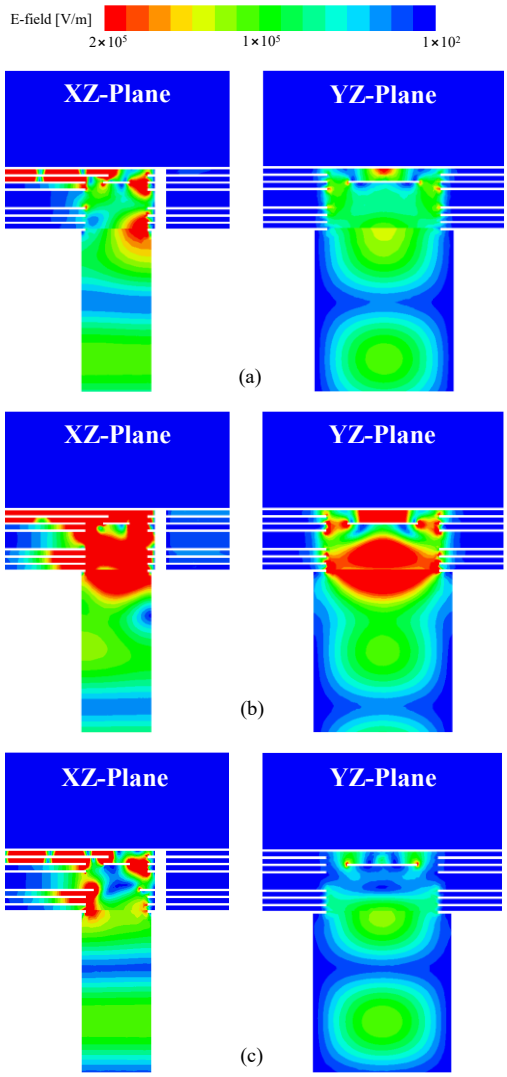

Figure 3.5 The electric field of the transition (a) without corrugation at 275 GHz, (b) without corrugation at 285.2 GHz, and (c) with corrugation at 285.2 GHz.

frequencies decrease, while it increases at higher resonant frequencies, as shown in Fig. 3.4 (a). The sharp drop in the transmission coefficient was improved when d_1 decreased, as depicted in Fig. 3.4 (b).

To investigate the phenomenon at the sharply dropped frequency and the effect of the corrugation, the electric fields of the transition in the XZ-plane and YZ-plane are simulated in Fig. 3.5. The electric field at the operational frequency of 275 GHz of the transition without corrugation is depicted in Fig. 3.5 (a). The electric fields in the signal line are coupled to the waveguide via a patch. On the other hand, at 285.2 GHz the electric field of the transition is

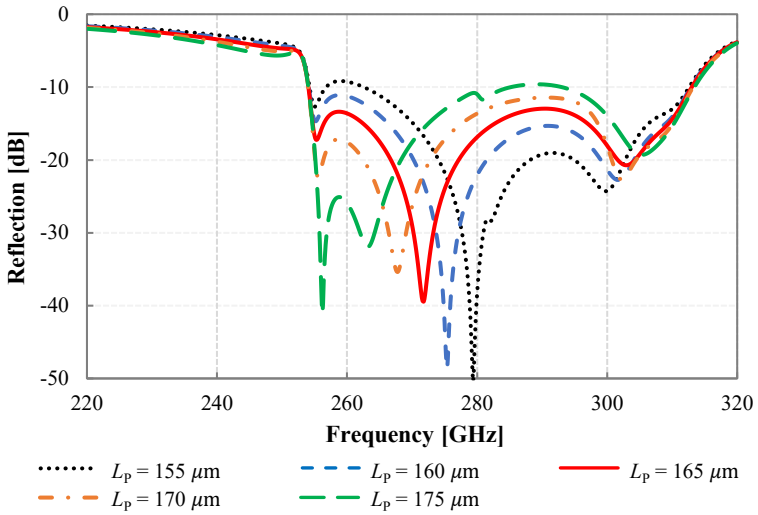

Figure 3.6 Reflection characteristics of the GSCPW-to-waveguide transition with corrugation structures depending on L_P.

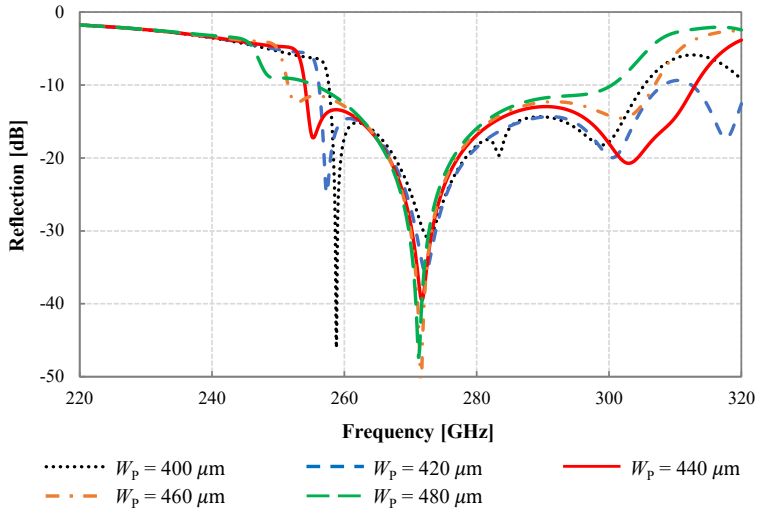

Figure 3.7 Reflection characteristics of the GSCPW-to-waveguide transition with corrugation structures depending on W_P.

high due to the effect of strong resonance as shown in Fig. 3.5 (b). The transmission coefficient sharply drops down at this frequency as shown in Fig. 3.2. To prevent this resonance, corrugations are applied at the edges around the aperture on layer 5. Consequently, the strong electric field of the transition at 285.2 GHz is reduced as shown in Fig. 3.5 (c) to the same level as in Fig. 3.5 (a). Therefore, the transmission coefficient improved, and the bandwidth was extended, as depicted in the red curve in Fig. 3.4.

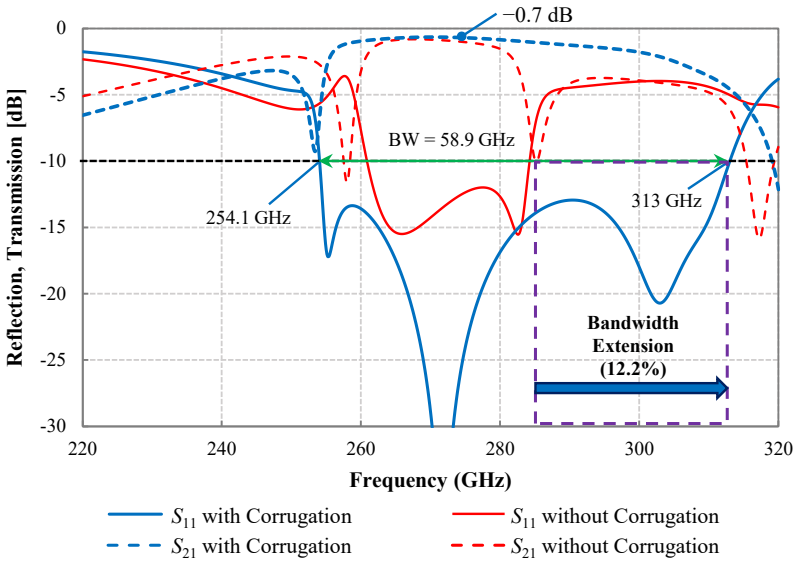

Figure 3.8 Simulation results of the transition with and without corrugation structures.

Fig. 3.6 illustrates the simulation of the scattering parameters depending on L_P. It is evident that as L_P increases, the center resonance frequency shifts to lower frequencies, resulting in a narrower bandwidth. Therefore, to achieve a wide bandwidth, the optimal value for L_P was determined to be 165 μm. The reflection characteristics of the transition with corrugation structures, depending on W_P, are illustrated in Fig. 3.7. Decreasing W_P leads to a decrease in the reflection coefficient level at lower resonant frequencies while increasing W_P results in an increase in the reflection coefficient level at higher resonant frequencies. The suitable value for W_P was found to be 440 μm.

The optimal design parameters obtained through electromagnetic simulation are summarized in Fig. 3.3 (b), while the transmission and reflection characteristics of these parameters are depicted in Fig. 3.8. The bandwidth of reflections less than −10 dB was 58.9 GHz (ranging from 254.1 GHz to 313.0 GHz). At the center frequency of 275 GHz, the transmission loss was observed to be 0.7 dB. The bandwidth of reflection characteristics at high frequencies was increased by 12.2%.

3.2 GCPW-to-Waveguide Transition in Multi-layer Substrates

The GCPW-to-waveguide transition uses a rectangular patch and extended bandwidth by corrugation structure. However, the transmission line is located on the lower layer 2 of the substrate. The structure to connect with mounted ICs becomes complicated. Therefore, this section proposes a GCPW-to-waveguide transition in a multi-layer dielectric substrate using a double rectangular stacked patch and a corrugation structure to extend the bandwidth. Moreover, the via-holes are strategically arranged to prevent leakage of the parallel plate mode within the substrates. The double line of via-hole arrangement was applied carefully to stop propagating in the E-plane [4], [5].

3.2.1 Configuration of the GCPW-to-Waveguide Transition

The designed GCPW-to-waveguide transition without corrugation structure is composed of WR-3 waveguide and multilayer substrates with HL972LF-LD [2] (Mitsubishi Gas Chemical Company, Inc.). The prepreg and the core substrates with a dielectric constant (ε_r) of 3.6 and loss tangent tan δ = 0.006 have thicknesses of 30 μm and 100 μm, respectively. Moreover, this transition has eight copper layers with a thickness of 15 μm, as shown in Fig. 3.9 (a). The configuration of the transition and geometrical parameters of each layer are shown in Fig. 3.9 (b). The via-holes are strategically arranged to prevent leakage of the parallel plate mode within the substrates. The double line of via-hole arrangement was applied carefully to stop propagating in the E-plane. To accomplish this, additional via-holes are introduced, as highlighted in blue. The length of the patch is designed to set the operation frequency at 275 GHz.

The simulation results of the GCPW-to-waveguide transition using these optimized parameters are shown in Fig. 3.10. The frequency bandwidth for the reflection coefficient less than −10 dB spans from 255.5 GHz to 279.5 GHz, resulting in a bandwidth of 24.0 GHz (8.9%). Also, at the center frequency of 275 GHz, the transmission coefficient was −1.0 dB. It shows a narrow bandwidth characteristic was observed due to the drop in S_{21} at 261.8 GHz and 282.8 GHz. The transmission coefficient sharply drops at a particular frequency due to the resonance among the apertures on Layer 2 to Layer 8.

Hence, a corrugation structure with a quarter-guided wavelength is implemented in the middle layer to mitigate resonance in the substrate and enhance transmission characteristics. A double rectangular stacked patch is employed to broaden the bandwidth. The configuration of

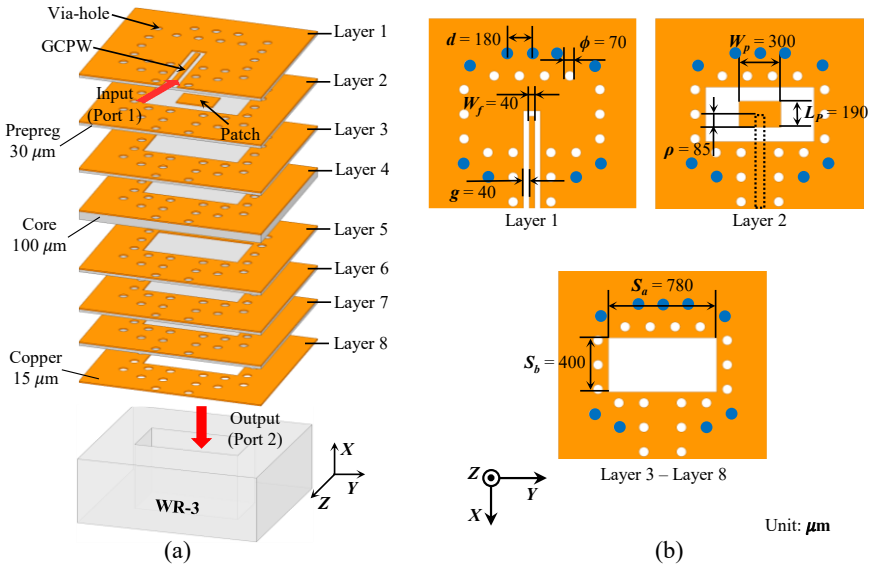

Figure 3.9 Configuration of the GCPW-to-waveguide transition (a) 3D overview and (b) Top views of each layer with the parameters.

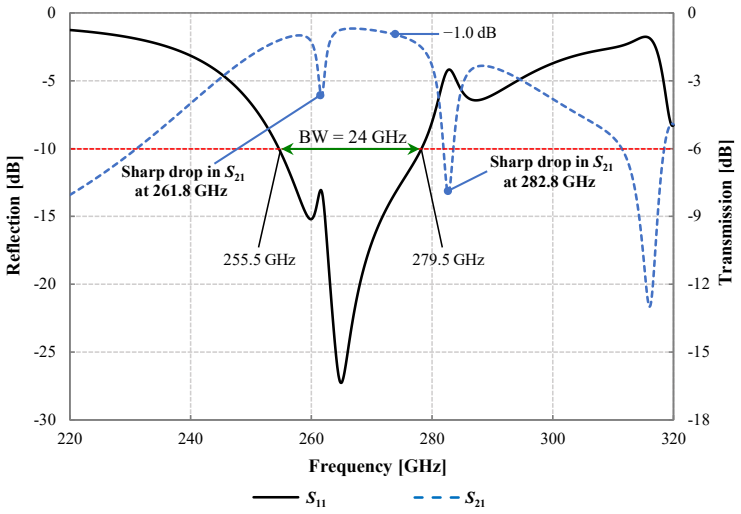

Figure 3.10 Scattering parameters of the GCPW-to-waveguide transition without corrugation structure.

the GCPW-to-waveguide transition with corrugation structures is depicted in Fig. 3.11 (a). The GCPW feed line is inserted into the waveguide on layer 1 of the dielectric substrate, with Patch 1 mounted on copper layer 2 and Patch 2 mounted on copper layer 3. The mechanism is shown in Fig. 3.11 (b). The electric field at the end of the signal line is coupled to Patch 1 on the copper layer 2 and Patch 2 on the copper layer 3. Patch 2 radiates into the waveguide and TE_{10} mode propagates toward the hollow waveguide through the lower dielectric layers. The configuration of the transition and geometrical parameters of each layer are shown in Fig. 3.11 (c). The via-holes are strategically arranged to prevent leakage of the parallel plate mode

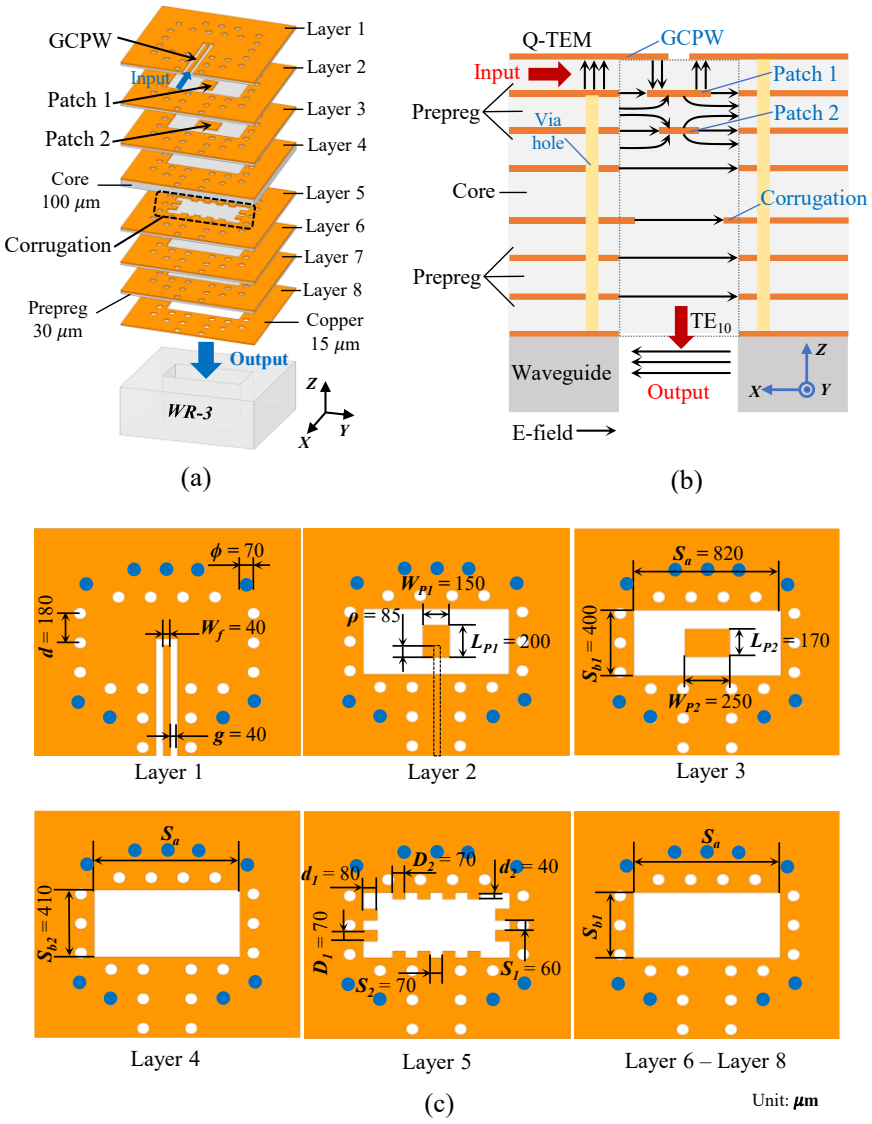

Figure 3.11 Configuration of the GCPW-to-waveguide transition with corrugation structure (a) 3D overview, (b) Transmission mode, and (c) Top views and geometrical parameters on layer n (n = 1, 2, …, 8).

within the substrates. A double line of via-hole arrangement was applied carefully to stop propagating in the E-plane. To accomplish this, additional via-holes are introduced, as highlighted in blue. The length of the Patch 1 is designed to set the operation frequency at 275 GHz. Eventually, the corrugation structure is applied at the middle layer to reduce the unwanted resonance in the substrate and improve the bandwidth over the high-frequency band.

3.2.2 Study Parameters of the GCPW-to-Waveguide Transition

This subsection investigates the reflection and transmission characteristics of the GCPW-to-waveguide transition with corrugation structures based on simulated parameters. The transition's numerical analysis is performed using the finite-element method ANSYS HFSS, to achieve a reflection coefficient of less than −10 dB. Parameter simulations were conducted to explore the essential elements of the transition's wideband design.

The critical parameters of the transition were analyzed to achieve wideband operation. Corrugation depth (d_1) significantly affects the transmission coefficient at lower frequencies, while corrugation depth (d_2) influences the transmission coefficient at higher frequencies

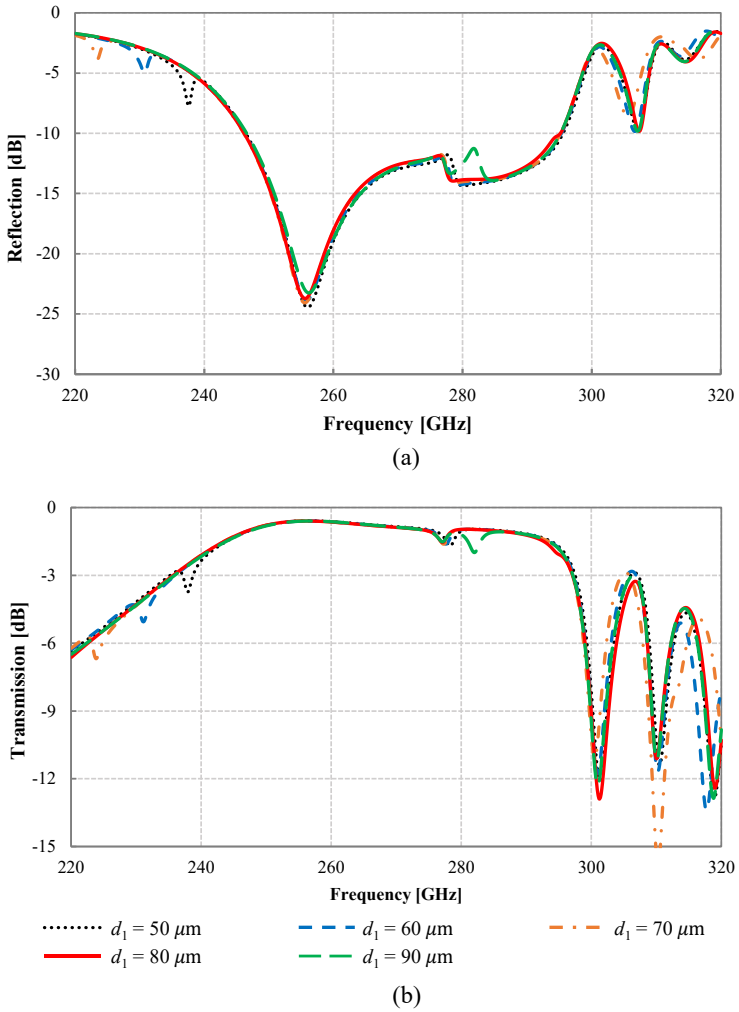

Figure 3.12 Scattering parameters of the GCPW-to-waveguide transition with corrugation structures depending on d_1 (a) reflection coefficient (b) transmission coefficient.

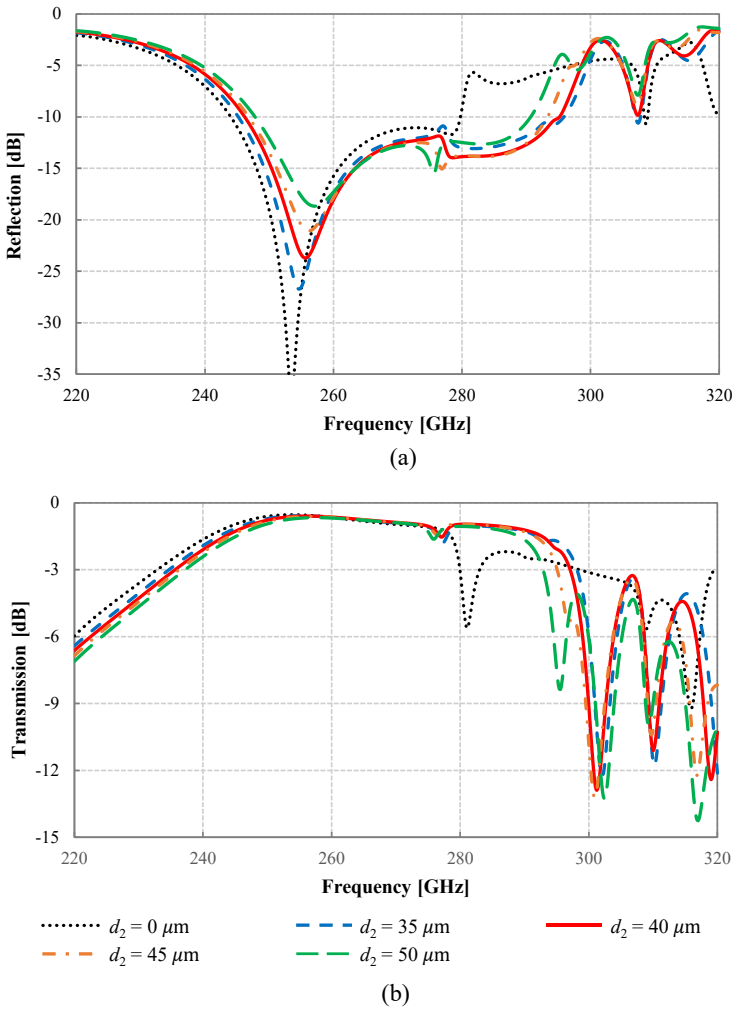

Figure 3.13 Scattering parameters of the GCPW-to-waveguide transition with corrugation structures depending on d_2 (a) reflection coefficient (b) transmission coefficient.

and bandwidth. These parameters collectively determine the resonant frequency, thereby impacting the enhanced bandwidth. The length of rectangular patch 1 (L_{P1}) is crucial for controlling resonant frequencies, while the length of rectangular patch 2 (L_{P2}) governs resonant frequencies and impedance matching.

Figure 3.12 displays the scattering parameters obtained from simulating the transition with varied corrugation depth (d_1). The depth d_1 influences a significant drop in the transmission coefficient at 261.8 GHz, which notably improves with a depth of 80 μm. As d_1 increases, the sharp drop in the reflection coefficient at lower frequencies shifts to even lower frequencies, as shown in Fig. 3.12 (a). Conversely, the improvement in the sharp drop of the transmission coefficient is evident with increasing d_1, as shown in Fig. 3.12 (b).

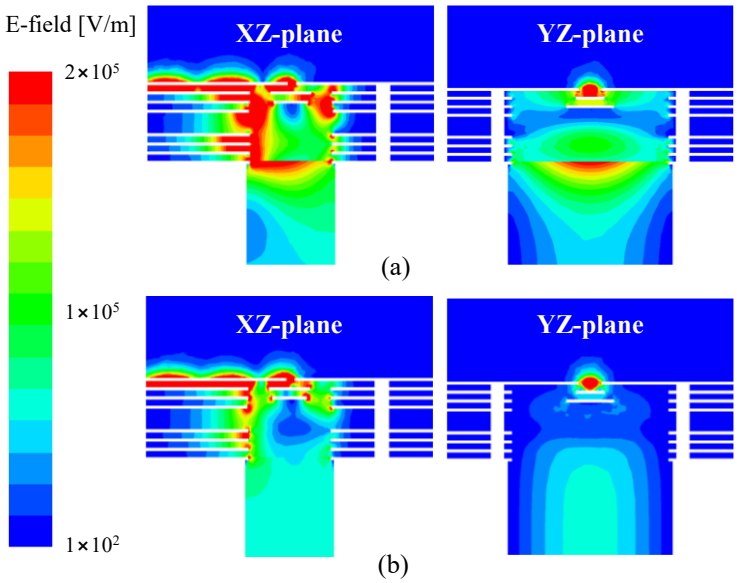

Figure 3.14 Simulated electric field of the transition on the XZ-plane and YZ-plane of the waveguide center at 282.8 GHz (a) d_2 = 0 μm, (b) d_2 = 40 μm.

Similarly, the scattering parameters from simulating the transition with varied corrugation depth (d_2) are presented in Fig. 3.13. Here, d_2 significantly affects the transmission coefficient and bandwidth. Increasing d_2 leads to a decrease in the reflection coefficient level at higher resonant frequencies, as shown in Fig. 3.13 (a), and variations in the transmission coefficient, as shown in Fig. 3.13 (b). Specifically, at 282.8 GHz, the transition without the d_2 (d_2 = 0 μm) results in a transmission drop, as illustrated in Fig. 3.13 (b).

Electric field simulations of the transition in the XZ-plane and YZ-plane at 282.8 GHz are depicted in Fig. 3.14. In Figure 3.14 (a), with a corrugation depth (d_2) of 0 mm, a high electric field is observed due to strong resonance, correlating with the sharp drop in transmission coefficient shown in Fig. 3.13 (b). Conversely, increasing d_2 to 40 μm improves the sharp drop in transmission coefficient, consequently reducing the strong electric field at 282.8 GHz, as evident in Fig. 3.14 (b).

The reflection coefficients of the transition depend on the length of patch 1 (L_{P1}), as shown in Fig. 3.15. As L_{P1} decreases, the lower resonant frequency shifts to a higher band. The suitable value for L_{P1} was found to be 200 μm. Additionally, the reflection coefficients of the transition depend on the length of patch 2 (L_{P2}), as shown in Fig. 3.16. As L_{P2} decreases, both lower and higher resonant frequencies shift higher. The suitable value for L_{P2} was determined to be 170 μm.

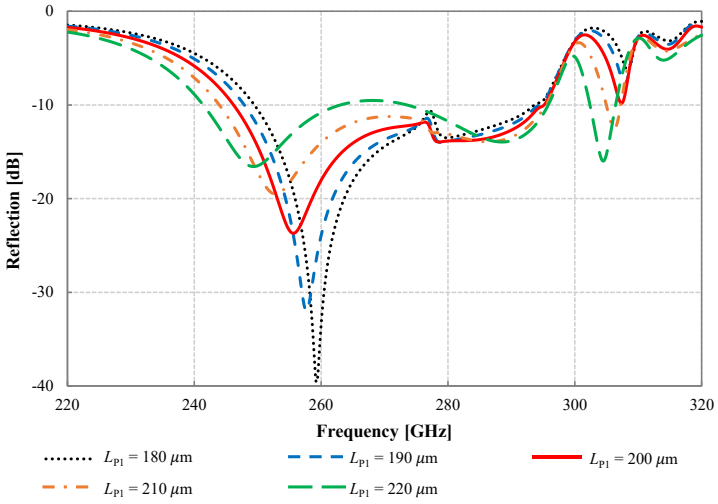

Figure 3.15 Reflection characteristics of the GCPW-to-waveguide transition with corrugation structures depending on L_{P1}.

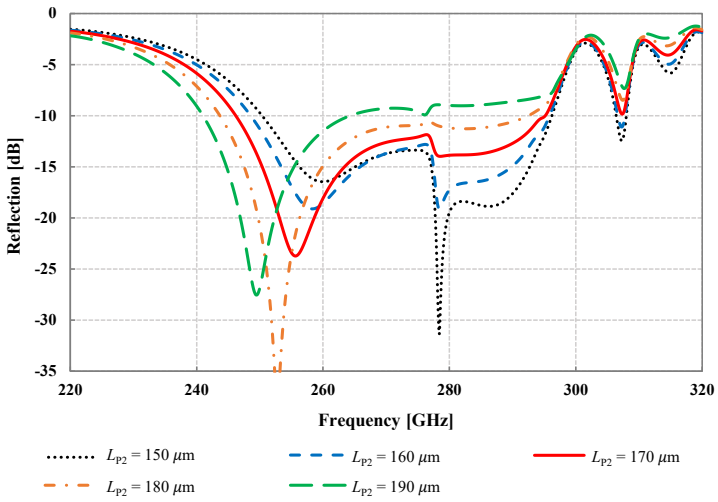

Figure 3.16 Reflection characteristics of the GCPW-to-waveguide transition with corrugation structures depending on L_{P2}.

The optimized parameters of the GCPW-to-waveguide transition using a double patch and corrugation structure are shown in Fig. 3.11 (c). To investigate the effectiveness of the double rectangular stacked patches in increasing the bandwidth, the scattering parameters of transitions are compared between a single and double patch with and without the corrugation structure in Fig. 3.17. The frequency bandwidth for the reflection coefficient transition using a double patch and corrugation structure, with values less than −10 dB, spans from 246.2 GHz to 295.2 GHz, resulting in a bandwidth of 49.0 GHz (18.1%). Also, at the center frequency of

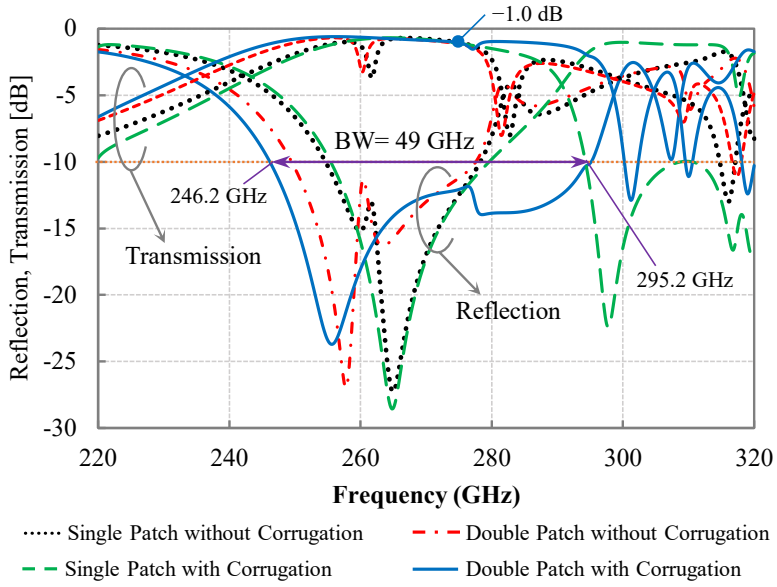

Figure 3.17 Comparison of simulated reflection and transmission coefficients of the GCPW-to-waveguide transitions.

275 GHz, the transmission coefficient was −1.0 dB, depicted by a solid blue line in Fig. 3.17. It can be observed that the bandwidths of the transition using a double patch and corrugation structure are approximately double that of the 24.0 GHz (8.9%) for the transition using a single patch and corrugation structure.

3.3 Waveguide-to-Differential-Line Transition in Multi-layer Substrates

This section proposes a broadband waveguide-to-differential-line transition covering the WR-3 band based on the principle of multimode resonance in a cavity. Broadband operation is accomplished through a combination of techniques, a triple circular stacked patch, and the utilization of multiple resonances within the circular cavity formed by a via-hole arrangement with apertures patterned in a multi-layer substrate. The differential lines are located on the top layer of the multi-layer substrate, where IC chips can be mounted. The differential lines are inserted from the broad wall of the waveguide. The TE_{10} mode on L8 of the rectangular waveguide transforms into the TE_{11} mode within the quasi-circular waveguide on L6 and L7. Subsequently, the TE_{11} mode from Patch 1 transforms into the quasi-TEM mode on the differential lines. Then, multimode resonance in a cavity produces broadband operation [6].

3.3.1 Configuration of the Waveguide-to-Differential-Line Transition

This subsection describes the configuration and the design of the proposed waveguide-to-differential-line transition. Planar-line-to-waveguide transitions can offer broadband performance across a broad frequency spectrum while maintaining low insertion losses. The purpose of developing this transition is to establish a connection between the 265 GHz CMOS circuit receiver and the WR-3.4 waveguide interface in a multi-layer substrate [7]. Multi-layer substrates provide the flexibility to integrate various passive and active components. Utilizing the specified core materials, these substrates offer the advantage of enabling the transition's use in intricate circuits requiring multiple routing layers. The multi-layer substrate consists of eight copper plates separated by seven dielectric plates, with three prepreg layers on each side of the core layer. It is produced using a high-pressure heating process. The modified semi-additive process (MSAP) achieves micropatterns with fine pitches [8]. These micropatterns are gold-plated with a thickness of 0.05 μm, following a 4 μm nickel layer application on the copper plate interface. MSAP imparts rounded corners to the metal patterns, with a 10 μm corner radius. The accuracy of metal patterns on the same layer is 10 μm, whereas, on different layers, it is 25 μm. Additionally, the signal line pattern width maintains an accuracy of ±10 μm.

The rectangular structure will produce errors with rounded corners, so a comparatively circular structure reduces the frequency shifts due to rounded corner errors and a more compact size at the same frequencies. The circular cavity structure was chosen for this paper because a

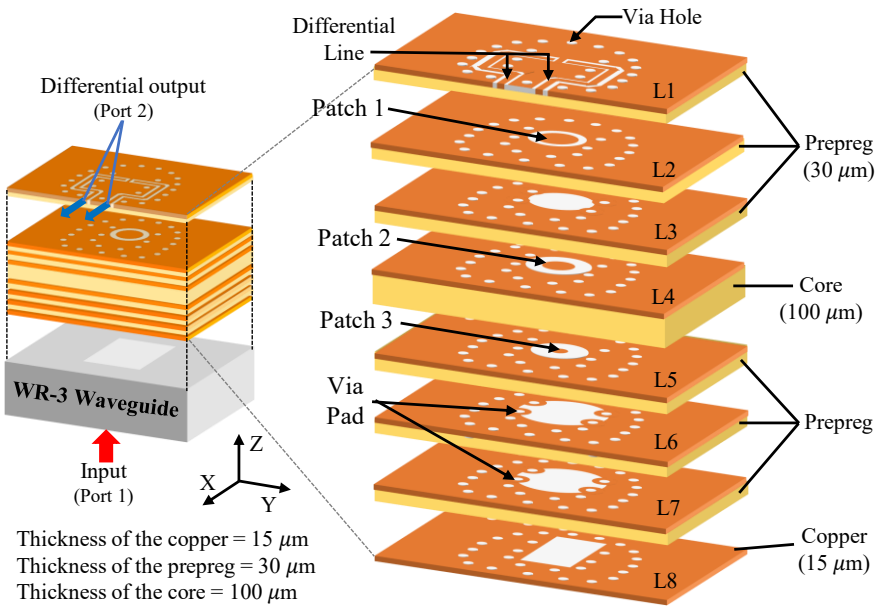

Figure 3.18 Configuration of the waveguide-to-differential-line transition.

circular cavity possesses a high degree of geometric symmetry, and the circular cross-section of the cavity inherently encourages the formation of multiple resonance modes.

The transition consists of three parts: a triple-stacked patch arrangement in the circular cavity structure and a via-hole arrangement to block the electric field leakage in the high band. The cavity structure in a multi-layer substrate consists of a main TE_{10} and TE_{11} dual-mode cavity. The concept behind this cavity structure is founded on utilizing three cavity resonance modes. The cavity structure is configured in an hourglass shape. The circular aperture sizes transition from small to large from L5–L7, whereas they shift from large to small from L2–L5. Specifically, L5 features the smallest apertures. On the other hand, L8 is distinguished by rectangular apertures, primarily due to its connection to the waveguide. Grounded coplanar waveguides (GCPW) are used as differential signal lines. The differential signal lines are inserted into the waveguide region on top of L1 from both broad walls of the waveguide, as shown in Fig. 3.18. The TE_{10} mode propagates in the bottom waveguide and inputs into the substrate from the aperture on the metal L8. The electromagnetic wave passes through all apertures on all metal layers. Three patches on L2, L4, and L5 were placed at the middle of the apertures to control the electromagnetic coupling between the apertures. The excited field at the patch on L2 was strongly coupled with the signal lines of the differential lines on top L1.

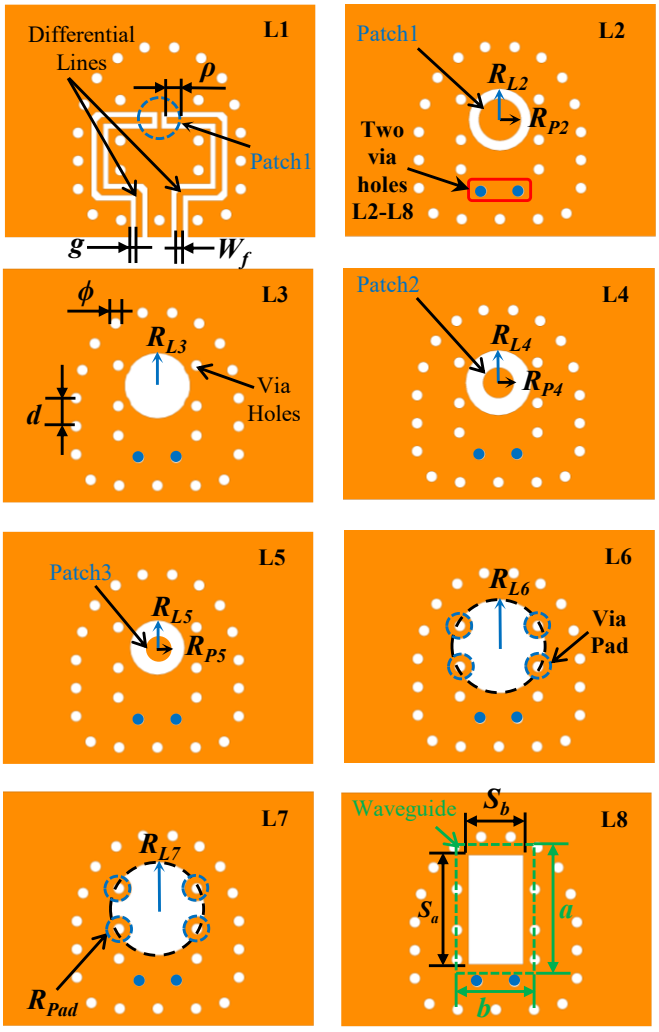

Figure 3.19 Top views of each layer with the parameters for the waveguide-to-differential-line transition.

The detailed design of each copper layer is shown in Fig. 3.19. The metal L8 is in direct contact with the bottom waveguide. Therefore, the aperture is rectangular, and its size is smaller than that of the waveguide cross-section for tolerance in assembly. The apertures on L2–L7 are circular and transformed into the TE_{11} mode, which forms a circular cavity in the multi-layer substrate. The size of the circular aperture gradually decreases from L7–L5. Next, the size of the circular patch increases from L5–L2 for a smooth flow of the electromagnetic wave from the waveguide to the upper layers for broadband characteristics, as shown in Fig. 3.20. The sizes of the circular apertures on L6 and L7 were designed to balance the mode transformation and prevent higher-order modes. To connect the via holes between L8 surrounding the rectangular

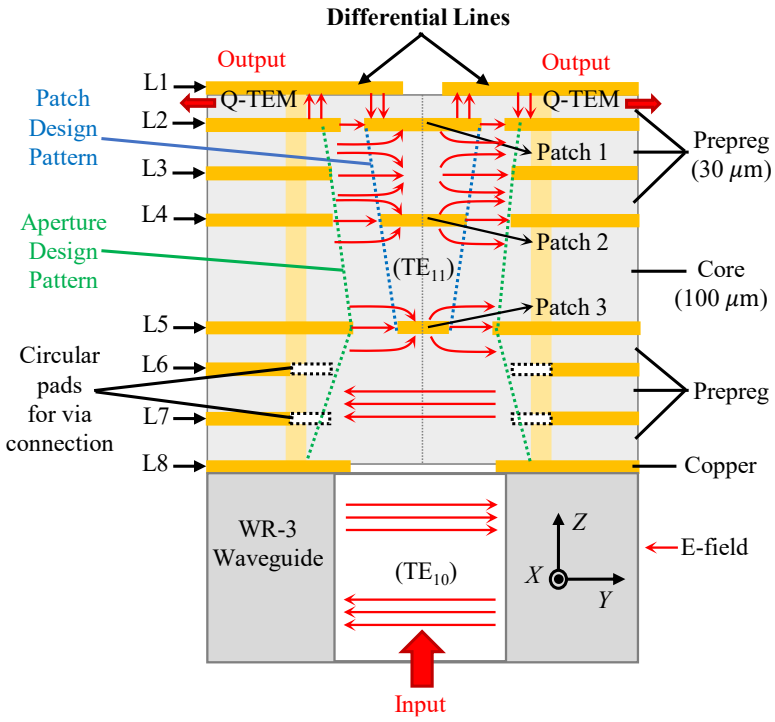

Figure 3.20 Cross-sectional view with transmission mode of the waveguide-to-differential-line transition.

aperture and L6 and L7 surrounding the circular apertures via pads are necessary in the inner region of the circular apertures.

The outer conductor of each patch was operated on the ground. The simulated electric field on each layer is shown in Fig. 3.21. It was confirmed that the electric field of the TE_{10} mode on L8 transformed into the TE_{11} mode in the quasi-circular waveguide on L6 and L7. Patch 3 on L5 was excited, and a strong electric field was generated on both sides of the patch. Patch 2 was excited in the same manner as Patch 3. These two patches are required for a strong coupling between both planes of the thick core layer. The field passes through the aperture on L3. The aperture sizes of L2–L4 were almost the same. However, the size of Patch 3 was smaller, the size of Patch 2 was larger, and Patch 1 was the largest. Therefore, the gap between the patch and the ground gradually decreased from lower to upper to increase the bandwidth. The cavity structure is anticipated to yield multiple resonances. Leveraging these principles, this transition has extended the bandwidth of reflection below –10 dB to encompass the range of 218.5–314.5 GHz. In this analysis, it can observe multimode resonant frequencies at 226 GHz, 278 GHz, and 304 GHz.

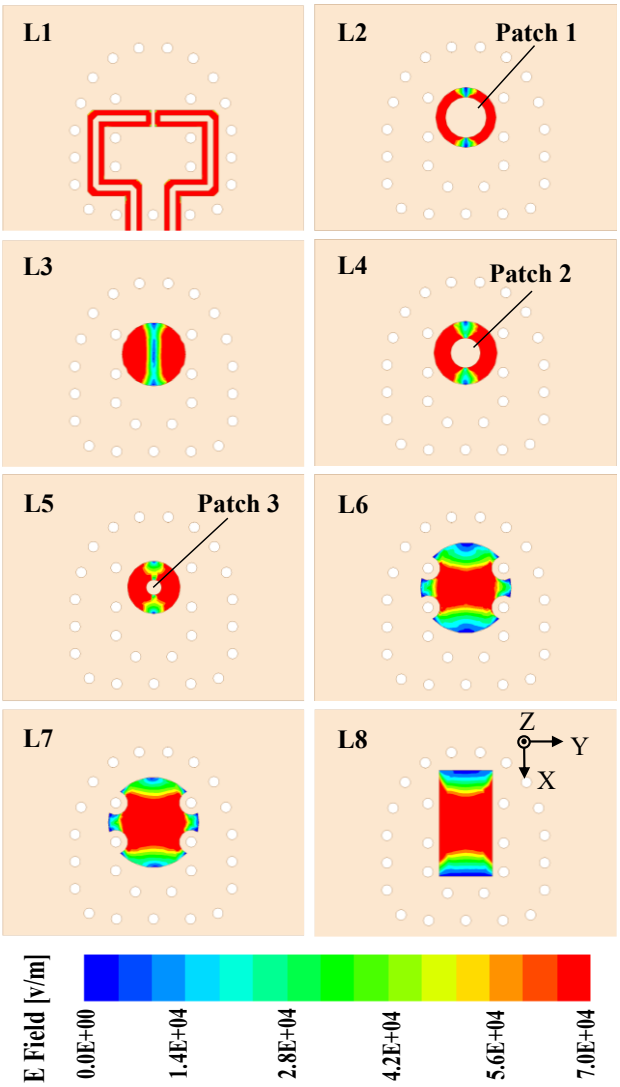

Figure 3.21 Simulated electric field distribution on the metal layer n (n = 1, 2, …, 8) of the waveguide-to-differential-line transition at 250 GHz.

To validate the impact of multi-transmission modes on the transition characteristics, a parametric study was conducted by systematically varying the radius of the circular patches and apertures. A strong electric field was excited on both sides of Patch 1 on L2 in the opposite phase. The signal lines of the differential line were essentially excited at 180° out of phase due to the symmetrical structure, resulting in differential mode operations.

Both the waveguide region and grounded coplanar lines were surrounded by the via-hole arrangement to prevent leakage of the parallel-plate mode between the ground planes. The minimum diameter of the via-holes, the minimum spacing between adjacent via-holes,

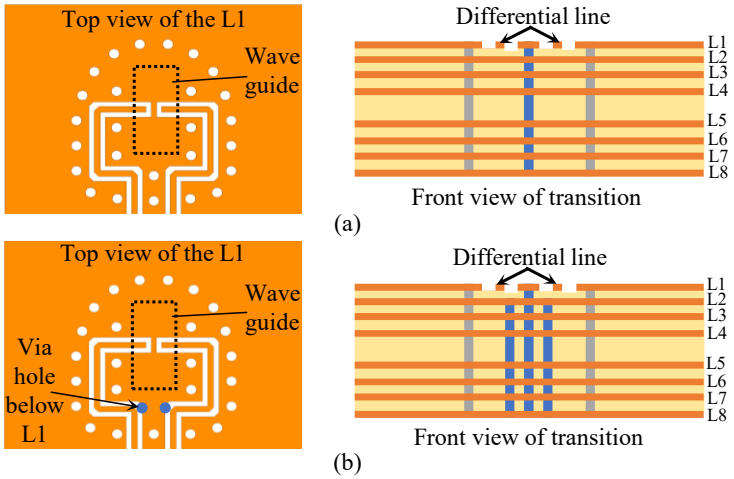

Figure 3.22 Via-hole arrangement (a) with center via-hole L1–L8 (b) with two via-holes L2–L8.

minimum clearance from the via-hole, and pattern edge of the aperture were limited owing to the fabrication process. The via-holes with a diameter of 70 μm are arranged around the waveguides with a center separation of 180 μm. In the manufacturing of the substrate, the via-hole positions may vary by up to ±25 μm, and their diameters may vary by up to ±20 μm. The layout of the via-holes was designed to minimize the leakage between the via-holes, as shown in Fig. 3.22 (a). The via-holes between the signal lines were located at the middle of the two signal lines. However, the via-hole spacing was sufficiently large to allow the leakage of electromagnetic waves from the waveguide corners. To prevent the leakage between the via-holes at the middle of the signal lines and at the waveguide corners, two via-holes were designed at a location nearly under the signal lines from L2–L8 without connecting to L1, as shown in Fig. 3.22 (b). The via-holes did not interfere with the signal lines on L1.

The features of the proposed transition are included in the eight copper patterns with a conductivity (σ) of 5.8×10^7 S/m. The copper plate has a thickness of 15 μm. The variation in thickness of the copper plate is less than ±7 μm. A seven-layer dielectric substrate HL972LF-LD [2] (Mitsubishi Gas Chemical Company, Inc.) with a dielectric constant (ε_r) 3.5 and loss tangent (tan δ) 0.003 (based on the datasheet) was used in this paper. Concurrently, three prepreg layers with copper were placed on both sides of the center core layer, forming seven dielectric layers. The thicknesses of the core and the prepreg substrates were 100 μm and 30 μm, respectively. The thickness variation of the core layer is less than ±15 μm, and the variations of the prepreg layers are less than ±10 μm. A WR-3 waveguide (864 μm × 432 μm) was used for the feeding. The dimensions of the design parameters for all the copper layers are

shown in Fig. 3.19. A differential line with width W_f and gap g was inserted into the waveguide region with an overlap ρ on the patch at the top layer, L1. Circular Patch 1 with radius R_{P2} approximately λg/4 at 250 GHz (where λg represents the wavelength in the substrate) was located at the center of the circular aperture on Substrate 2. The radius of Circular Patch 2 and Circular Patch 3 can be approximately less than λg/8 at 250 GHz. Circular Patch 2 with radius R_{P4} and circular Patch 3 with radius R_{P5} were placed at the center of the circular apertures on both sides of the thick-core substrate for strong coupling. After arranging the elements within their layers and assessing their interactions with the ground planes, parameters were optimized to adjust size and gap dimensions. The rectangular aperture $Sa \times Sb$ on L8 was slightly smaller than that on the WR-3 waveguide.

3.3.2 Parametric Analysis of the Waveguide-to-Differential-Line Transition

This subsection presents the numerical investigations of the multi-layer waveguide-to-differential-line transition using the finite element electromagnetic simulator ANSYS HFSS. Furthermore, parameters such as the circular patch radius, circular aperture radius of each layer, and via hole arrangement were investigated to study their effects on the frequency response and bandwidth of the transition.

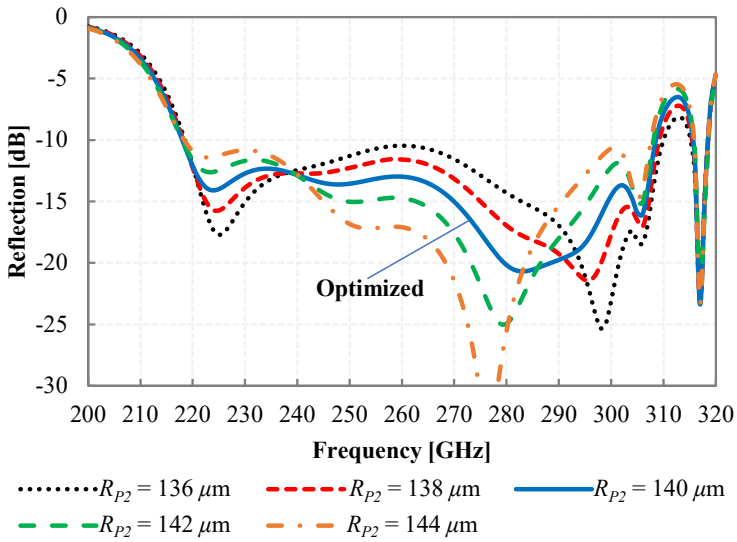

Figure 3.23 Reflection characteristics of the waveguide-to-differential-line transition with center via-hole L1–L8 depending on R_{P2}.

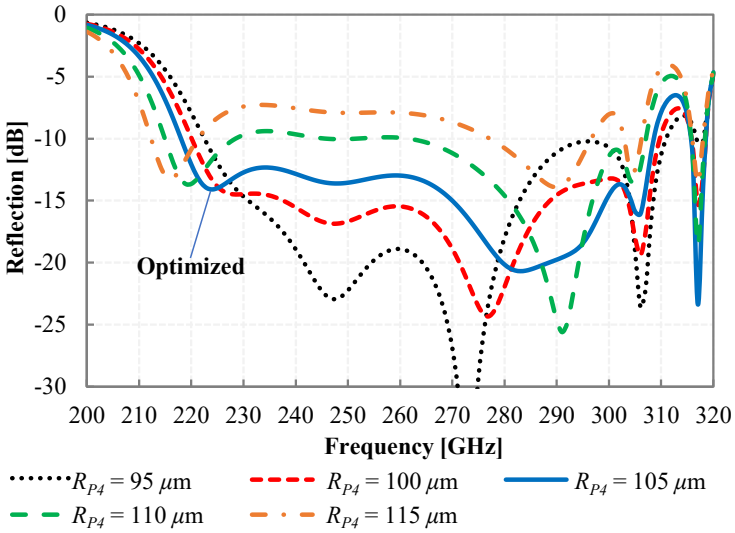

Figure 3.24 Reflection characteristics of the waveguide-to-differential-line transition with center via-hole L1–L8 depending on R_{P4}.

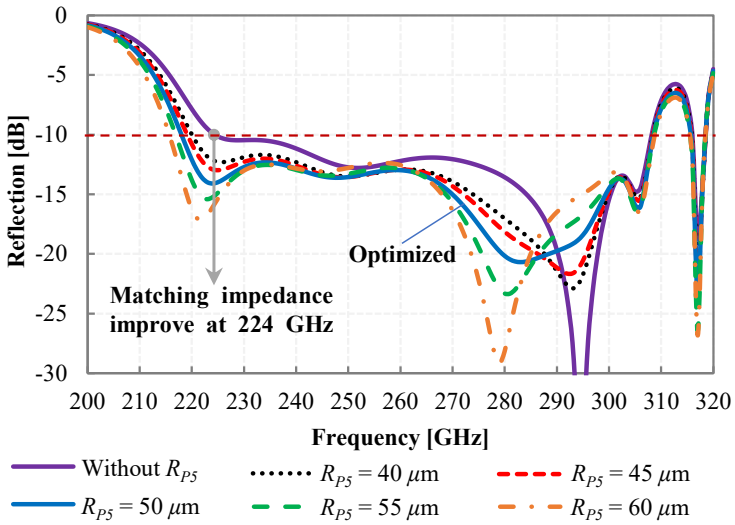

Figure 3.25 Reflection characteristics of the waveguide-to-differential-line transition with center via-hole L1–L8 depending on R_{P5}.

This part discusses the effects of the circular patch radius. The effect of the radius of circular Patch 1 was studied. The radius of circular Patch 1 (R_{P2}) affects the center resonant frequency observed at approximately 250 GHz. As the radius decreased, the center resonant frequency shifted to a higher as shown in Fig. 3.23. The effect of the radius (R_{P4}) of parasitic Patch 2 was analyzed. When varying R_{P4}, the reflection level changes, as shown in Fig. 3.24. This implies that the electromagnetic coupling was controlled by changing R_{P4}. As R_{P4} decreases, the radius of circular Patch 2 approaches that of circular Patch 3, enhancing electric field coupling. Thus, significant improvement in impedance matching was observed.

Conversely, the reduced radius of circular Patch 2 led to a reduction in the bandwidth. Thus, the optimum value for R_{P4} was 105 μm, providing a broad bandwidth and a suitable matching impedance. This suggests that the matching characteristics can be controlled by changing the radius of circular Patch 2 during the transition.

The effect of the radius of the parasitic circular Patch 3 (R_{P5}) was analyzed. Circular Patch 3 was crucial for improving the matching impedance at low frequencies. The reflection coefficient of the transition depends on R_{P5}, as shown in Fig. 3.25. The results demonstrated an improved matching impedance at 224 GHz and an increased bandwidth at low frequencies. As R_{P5} increased, the matching impedance at low and high frequencies increased. However, it is worth noting that a slight impact on bandwidth occurs with an increased R_{P5}. The optimal value of R_{P5} was 50 μm.

This part discusses the effects of the aperture on each layer. The effect of the aperture radius on L2 (R_{L2}) was studied to assess its effect on the resonant frequency and bandwidth of the transition. Fig. 3.26 illustrates the influence of varying R_{L2}, which includes the circular Patch 1, on the reflection coefficient. The aperture size affected the distance between the patches and the aperture edges. When the R_{L2} decreased, the gap with the patch decreased. The bandwidth

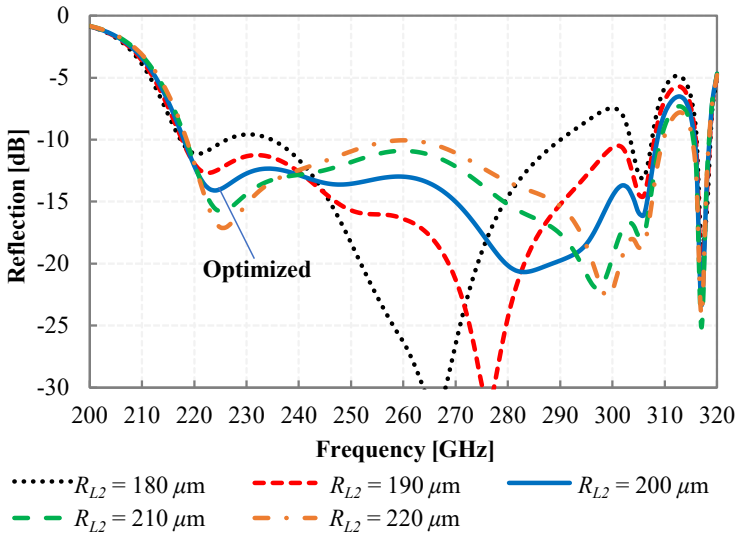

Figure 3.26 Reflection characteristics of the waveguide-to-differential-line transition with center via-hole L1–L8 depending on R_{L2}.

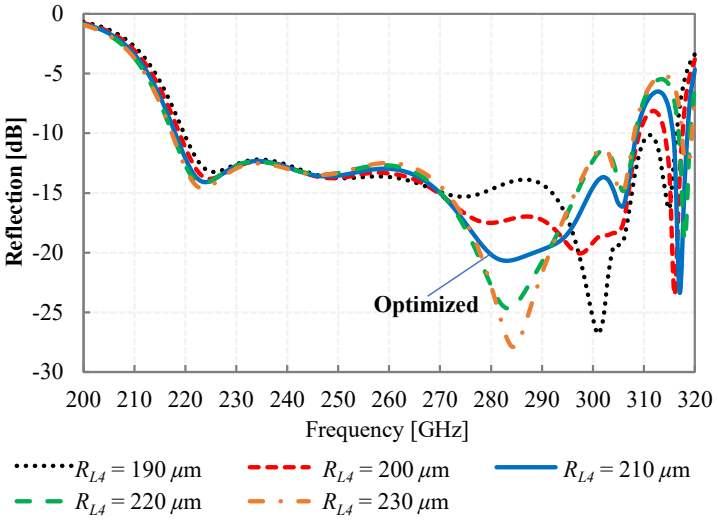

Figure 3.27 Reflection characteristics of the waveguide-to-differential-line transition with center via-hole L1–L8 depending on R_{L4}.

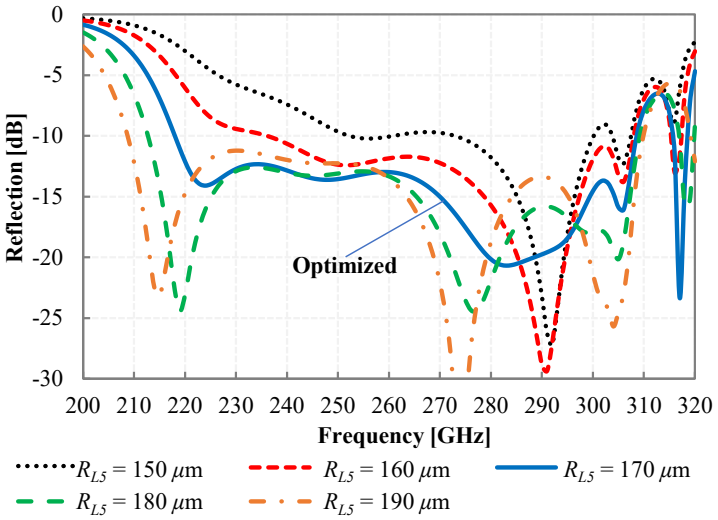

Figure 3.28 Reflection characteristics of the waveguide-to-differential-line transition with center via-hole L1–L8 depending on R_{L5}.

narrowed with a shifting lower band, owing to the high-Q structure. The effect of the aperture radius on L4 (R_{L4}), which contains circular Patch 2, on the reflection coefficient at high frequencies is shown in Fig. 3.27. As observed, a decrease in R_{L4} resulted in an improvement in the matching impedance at high frequencies.

Fig. 3.28 illustrates the dependence of the reflection coefficient on the radius of the aperture on L5 (R_{L5}). The graph demonstrates that increasing R_{L5} significantly improves impedance matching in the low-frequency band. The transmission mode changed drastically at L5 from

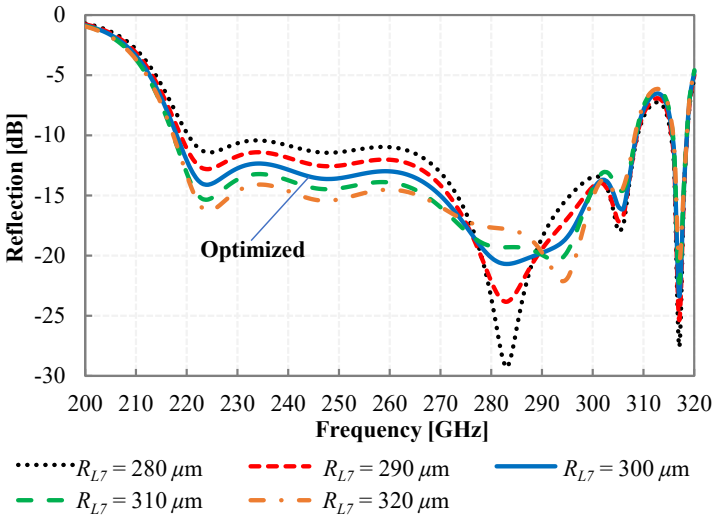

Figure 3.29 Reflection characteristics of the waveguide-to-differential-line transition with center via-hole L1–L8 depending on R_{L7}.

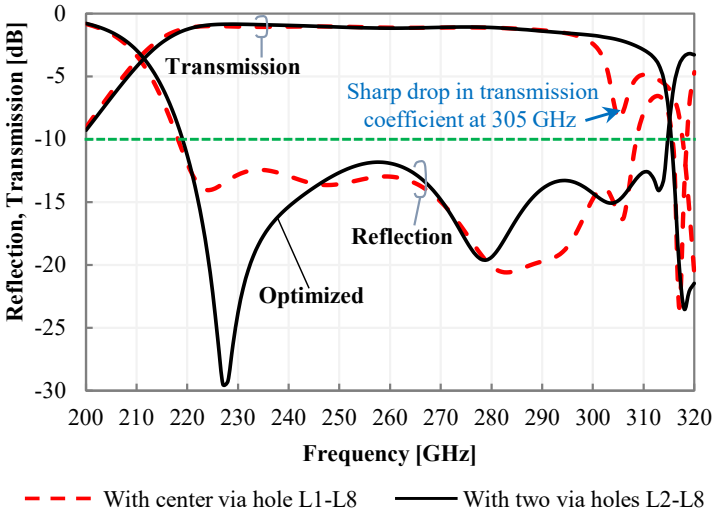

Figure 3.30 Comparison of the scattering characteristics of transition with center via-hole L1-L8 and with two via-holes L2-L8.

the waveguide mode to the coaxial mode because of the center patch. Therefore, the dimensions of the apertures R_{L5} and patch R_{P5} are significant parameters for controlling the bandwidth. Fig. 3.29 shows the reflection coefficient of the transition as the radius of the aperture on L7 (R_{L7}) is varied. The graph demonstrates that the matching impedance at the low-frequency range improves as the radius increases, thereby providing evidence that the aperture radius significantly influences the reflection coefficient level. In conclusion, R_{L2} regulates the reflection coefficient level of the transition across the entire frequency range. R_{L4} governs

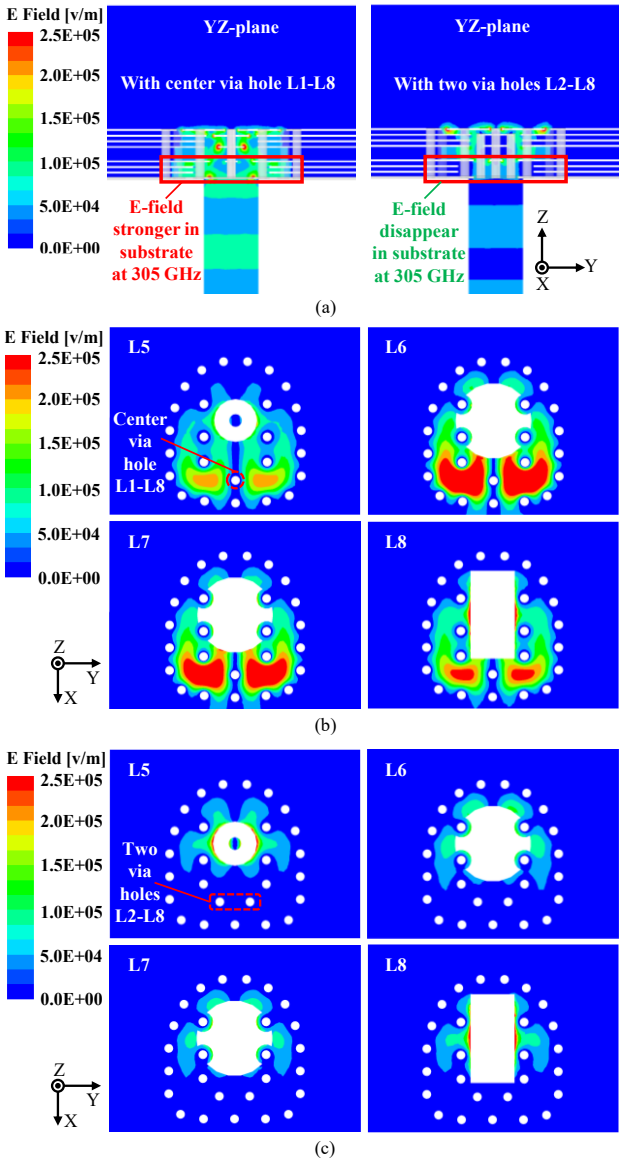

Figure 3.31 Simulated electric field distribution of the proposed transition at 305 GHz (a) Electric field distribution on the YZ-plane of the waveguide center (b) Electric field distribution of the transition from L5–L8 of the multi-layer substrates with center via-hole L1–L8 (c) Electric field distribution of the transition from L5–L8 of the multi-layer substrates with two via-holes L2–L8.

the reflection coefficient level of the transition at high frequencies, whereas R_{L5} and R_{L7} determine the reflection levels of the transition in the low-frequency range.

The via-hole spacing against wavelength is wider in the higher-frequency band. This subsection describes the enhancement of the transmission and reflection coefficients at high frequencies by improving the via-hole arrangement. In response to the identified issue, the rearrangement of the via-holes is shown in Fig. 3.22. The layout of the via-holes was designed to minimize the leakage between the via-holes. Fig. 3.30 shows the transmission and reflection

coefficients of these transitions. An analysis was conducted to identify the factors contributing to the decrease in the transmission coefficient at high frequencies over 300 GHz by examining the electric field distribution on each transition layer. Fig. 3.31 illustrates the electric field distribution of the proposed transition at 305 GHz. Fig. 3.31 (a) shows the electric field distribution on the YZ-plane, including the center axis of the waveguide, indicating a stronger electric field in the substrates from L5–L8. Consequently, resonance occurs at a frequency of 305 GHz, leading to a decrease in the transmission coefficient at this frequency, as depicted by the red dashed line in Fig. 3.30. It was observed that the inclusion of two via-holes in L2–L8 effectively eliminates the strong electric field. To demonstrate the preventive effect of the via-hole arrangement on the electric field leakage, Figs. 3.31 (b) and 3.31 (c) illustrate the electric field distribution of the transition from L5–L8 in the multi-layer substrates with a center via-hole in L1–L8 and two via-holes in L2–L8. The results indicate that the via-hole arrangement, specifically with two via-holes in L2–L8, effectively prevents leakage and resonance at 305 GHz. The proposed arrangement reduced the via-hole pitch and positioned the via-holes to cover the waveguide connections. Consequently, the transmission coefficient was improved, which is evident from the enhancement shown by the black dashed line in Fig. 3.30.

Table 3.1 presents all the parameters of the waveguide-to-differential-line transition obtained through this optimization process after conducting a comprehensive study on the impact of various transition parameters and subsequent optimizations. Except for three parameters, namely, the radius of circular Patch 1 (R_{P2}), the radius of circular Patch 2 (R_{P4}), and the radius of the circular aperture on L5 (R_{L5}), all the other parameters remained unchanged between the transitions with a center via-hole in L1–L8 and with two via-holes in L2–L8. The proposed transition introduces the following parameter values: R_{P2} = 140 μm, R_{P4} = 104 μm, and R_{L5} = 170 μm.

Table 3.1 Optimized parameters of the waveguide-to-differential-line transition

Name	Description	Value
W_T	Total width of the transition	1.5 mm
L_T	Total length of the transition	1.5 mm
a	Broad wall length of the waveguide	864 μm
b	Narrow wall length of the waveguide	432 μm
ϕ	Diameter of via-hole	70 μm
d	Distance between via-holes (Pitch)	180 μm
W_f	Width of differential line	40 μm
g	Width of gap	35 μm
ρ	Overlap length of inserted probe	87.5 μm
R_{P2}	Radius of circular Patch 1	135 μm
R_{P4}	Radius of circular Patch 2	98 μm
R_{P5}	Radius of circular Patch 3	50 μm
R_{L2}	Radius of circular aperture on L2	200 μm
R_{L3}	Radius of circular aperture on L3	210 μm
R_{L4}	Radius of circular aperture on L4	210 μm
R_{L5}	Radius of circular aperture on L5	175 μm
R_{L6}	Radius of circular aperture on L6	300 μm
R_{L7}	Radius of circular aperture on L7	300 μm
R_{Pad}	Radius of circular pad for via-holes	80 μm
S_a	Broad wall length of aperture on L8	700 μm
S_b	Narrow wall length of aperture on L8	350 μm

3.4 Experimental Performances

This subsection presents the validated simulation results of the proposed transition that were obtained by conducting measurements on the fabricated transitions. This study focused on measuring the transmission loss and reflection characteristics.

3.4.1 Fabrication and Measurement Setup

A back-to-back configuration was employed to assess the transmission line losses, characteristics, and efficiencies of the proposed transitions. The fabrication accuracy from the company is shown in Table 3.2. The setup of the measurement system is shown in Fig. 3.32. The measured transitions were positioned on a metal jig connected to the waveguide. The measurement setup involved a differential line connecting two identical transitions with the same geometrical parameters as those of the fabricated transition (device under test: DUT). The DUT was mounted on a metal jig, and the waveguides were connected at both terminals and attached to the flange of a standard waveguide (WR-3), as shown in Fig. 3.32 (a). A choke structure was built around the waveguide on the jig surface to reduce leakage from the gap between the substrate and the jig. The DUT was fixed at a particular position with high precision using a small screw with a diameter of 1 mm. The measurement accuracy was ensured through repetition of the assembly and measurements. Millimeter-wave extension modules VDI WR-3.4-VNAX were connected to a vector network analyzer (ANRITSU MS4647B), as shown in Fig. 3.32 (b). The two ports of the standard waveguide, which extend from the millimeter-wave module, were calibrated using a WR-3 Anritsu waveguide calibrator model SM6567 at the waveguide-connected plane within the metal jig. The reflection and transmission characteristics encompassing the waveguide within the jig and the transmission line between the two transitions were measured. A vector network analyzer equipped with a time-gate domain function was employed to measure the scattering parameters and mitigate the occurrence of multiple reflections [9]. The entire frequency band of WR-3, ranging from 220 to 320 GHz, was utilized to achieve high time resolution.

Table 3.2 Fabrication accuracies of the multi-layer substrates

	Accuracy
Thickness of the core	±15 μm
Thickness of the prepreg	±10 μm
Thickness of the copper	±7 μm
Via diameter	±20 μm
Via position	±25 μm
Pattern width of the signal lines	±10 μm
Gap	±10 μm

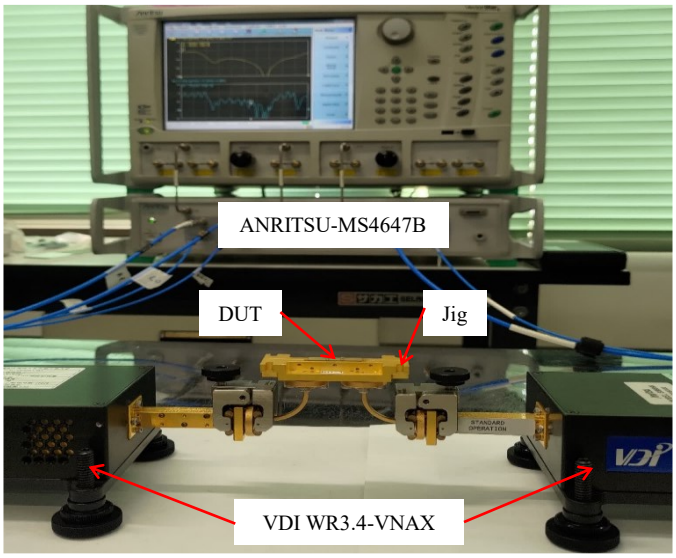

(a)

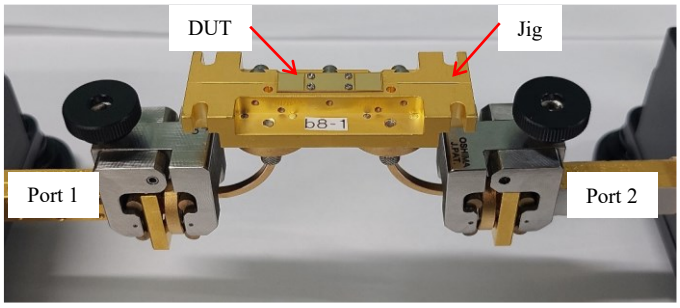

(b)

Figure 3.32 Experimental setup of the broad-wall-inserted planar-line-to-waveguide (a) top view (b) side view.

3.4.2 Measurement Results of the GSCPW-to-Waveguide Transition

To evaluate the insertion loss of each transition accurately, the losses of the transmission line between the transitions and waveguides within the jig were measured to determine the required compensation. A study focused on investigating losses in transmission line structures on package substrates tailored for the 100 GHz to 300 GHz frequency range. The performance of these transmission lines was evaluated through a combination of analytical and experimental methods, as implemented in [10]. To obtain the transmission loss of the transmission line transitions with back-to-back configurations connected by transmission lines of different lengths were fabricated as shown in Fig. 3.33. The lengths of the transmission lines were selected as 3.136, 5.136, 7.136, and 19.136 mm to evaluate the transmission loss of the transmission line accurately.

The measured and simulated scattering parameters for the GSCPW-to-waveguide transition are shown in Fig. 3.34. The measurement process used the WR-3 standard equipment, which covered the entire frequency band ranging from 220 to 320 GHz. The simulation results for the transition indicate a bandwidth of reflection coefficient less than −10 dB, which spans 58.9 GHz (20.7%). The simulated transmission coefficient of the transition at the center frequency of 275 GHz was −0.7 dB. The measured results, the bandwidth of reflection lower than −10 dB was 60.8 GHz (21.8%). The measured transmission coefficient at the design frequency of 275 GHz was −4.3.0 dB.

It is evident from the graph that the measured reflection coefficient shifted to lower frequencies and the reflection level was deferred. This shift can be attributed to the imperfections in the size and position of the via hole as well as uneven substrate thickness. Furthermore, the measured dielectric constant of the fabricated substrate exceeded the reference value provided in the datasheet, with a value of approximately 3.6 at 275 GHz. The measured transmission coefficient results differ from the simulation results mainly because of the surface roughness of the copper sticking to the substrate. This discrepancy could be attributed to imperfections in the size of the corrugation structure and placement of the patch, as well as misalignment between layers during the fabrication process.

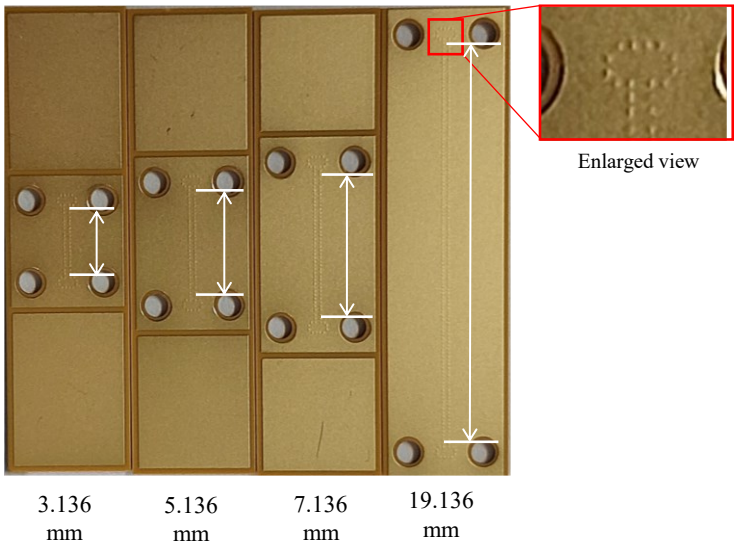

Figure 3.33 Fabricated the GSCPW-to-waveguide transition (DUT) with various lengths of the transmission line and an enlarged view.

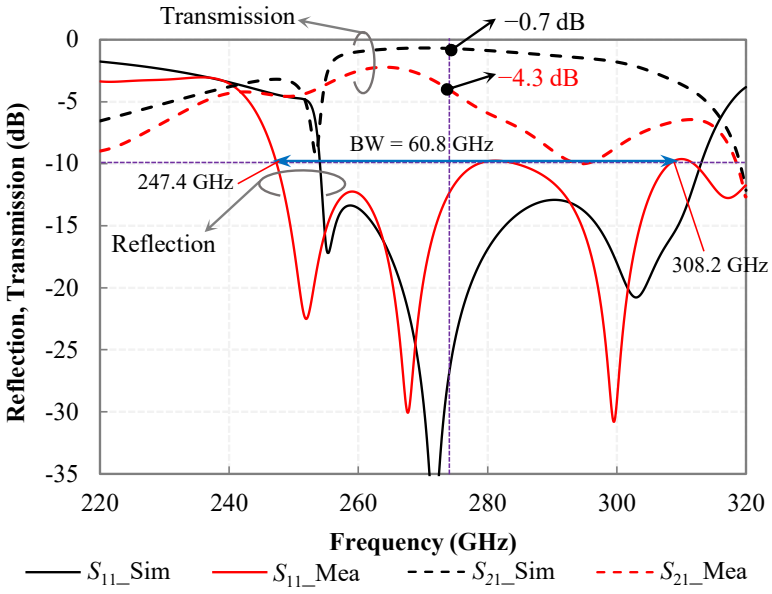

Figure 3.34 Simulated and measured scattering parameter results of the GSCPW-to-waveguide transition.

3.4.3 Measurement Results of the GCPW-to-waveguide Transition

To evaluate the insertion loss of each transition accurately, the losses of the transmission line between the transitions and waveguides within the jig were measured to determine the required compensation. To obtain the transmission loss of the transmission line transitions with back-to-back configurations connected by transmission lines of different lengths were

fabricated as shown in Fig. 3.35. The lengths of the transmission lines were selected as 3.136, 5.136, 7.136, and 19.136 mm to evaluate the transmission loss of the transmission line accurately.

The measured and simulated scattering parameters for the GCPW-to-waveguide transition are shown in Fig. 3.36. The measurement process used the WR-3 standard equipment, which covered the entire frequency band ranging from 220 to 320 GHz. The simulation results for the transition indicate a bandwidth of reflection coefficient less than −10 dB, which spans 49.0 GHz (18.1%). The simulated transmission coefficient of the transition at the center frequency of 275 GHz was −1.0 dB. The measured results, the bandwidth of reflection lower than −10 dB was 48.0 GHz (18.1%). The measured transmission coefficient at the design frequency of 275 GHz was −4.4 dB.

It is evident from the graph that the measured reflection coefficient shifted to lower frequencies and the reflection level was deferred. This shift can be attributed to the imperfections in the size and position of the via hole as well as uneven substrate thickness. Furthermore, the measured dielectric constant of the fabricated substrate exceeded the reference value provided in the datasheet, with a value of approximately 3.6 at 275 GHz. The measured transmission coefficient results differ from the simulation results mainly because of the surface roughness of the copper sticking to the substrate. This discrepancy could be attributed to imperfections in the size of the corrugation structure and placement of the patch, as well as misalignment between layers during the fabrication process.

This is attributed to significant variations in the transmission coefficient measurement results at high frequencies. Consequently, a thorough analysis focuses on understanding the reasons behind the discrepancies between the measurement and simulation results, particularly concerning the substrate properties and the surface roughness of the metal. Further details are provided in the subsequent subsection.

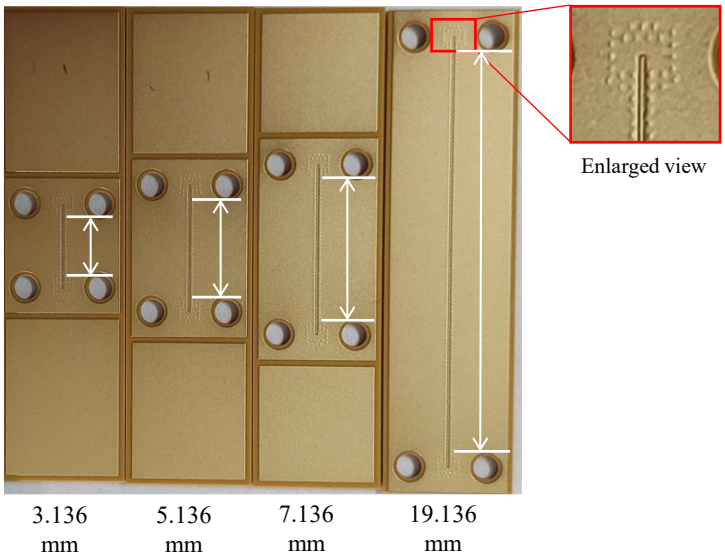

Figure 3.35 Fabricated the GCPW-to-waveguide transition (DUT) with various lengths of the transmission line and an enlarged view.

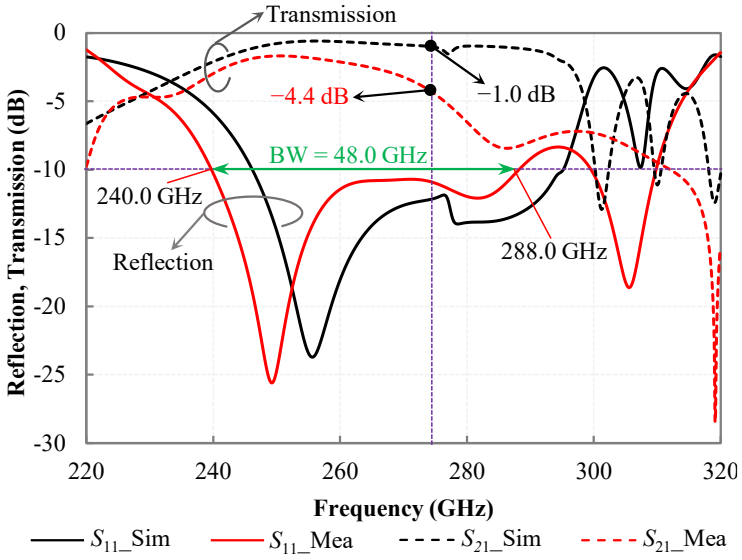

Figure 3.36 Simulated and measured scattering parameter results of the GCPW-to-waveguide transition.

3.4.4 Measurement Results of the Waveguide-to-Differential-Line Transition

To evaluate the insertion loss of each transition accurately, the losses of the differential line between the transitions and waveguides within the jig were measured to determine the required compensation. A study focused on investigating losses in transmission line structures on package substrates tailored for the 100 GHz to 300 GHz frequency range. The performance of these transmission lines was evaluated through a combination of analytical and experimental methods, as implemented in [10]. To obtain the transmission loss of the differential line transitions with back-to-back configurations connected by differential lines of different lengths were fabricated as shown in Fig. 3.37. The lengths of the transmission lines were selected as 3.136, 5.136, 7.136, and 19.136 mm to evaluate the transmission loss of the differential line accurately. Fig. 3.38 illustrates the transmission loss of the differential line, assessed by examining the slopes of curves derived from transmission measurements with differential lines of four different lengths at 230, 250, and 270 GHz. The assessment reveals a transmission loss of approximately 0.8 dB/mm at 250 GHz. Fig. 3.39 illustrates the individual losses of each component for estimating the insertion loss of a single transition. The measured transmission of the back-to-back of two transitions, including transmission line and jig from Port 1 to Port 2, is represented by the black dashed line. The purple dashed line represents the 3.136 mm transmission line loss, estimated from the difference in measured transmissions for the back-to-back transition of four lengths, as shown in Fig. 3.37. Additionally, the transmission with waveguide losses in the jig, indicated by the green dashed line, was obtained through the jig

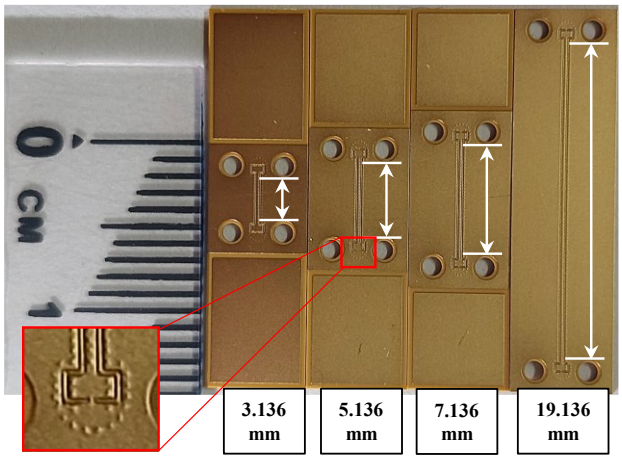

Figure 3.37 Fabricated DUT for different lengths of the transmission line and an enlarged view of the waveguide-to-differential-line transition (left).

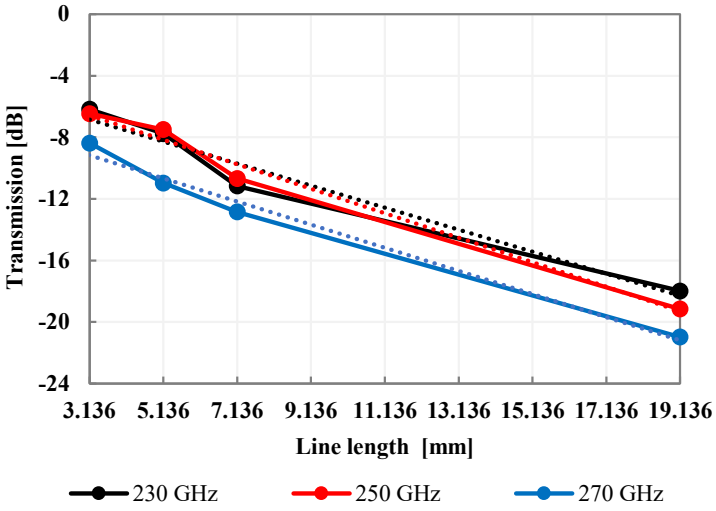

Figure 3.38 Measured transmission of the fabricated waveguide-to-differential-line transition with four different line lengths.

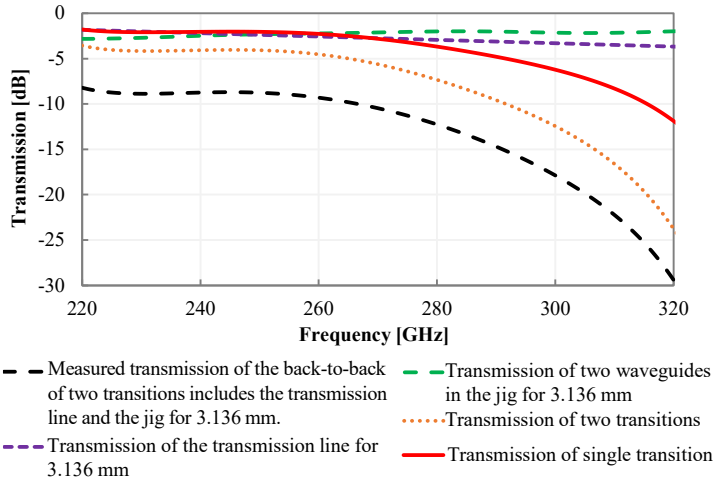

Figure 3.39 Transmission characteristics at each correction process of the waveguide-to-differential-line transition.

measurement. The loss of the waveguide in the jig was measured by connecting two identical jigs. The losses of the two waveguides in the jigs were measured as 1.8 dB at 250 GHz, and the loss of the single waveguide in the jig was estimated to be 0.9 dB by dividing the measured transmission of the two jigs by two. Finally, the transmission coefficient of the single transition was evaluated from the transmission of the entire structure with a differential line of 3.136 mm by de-embedding the jig, and differential line losses at every frequency point across the entire frequency band are represented by the red solid line.

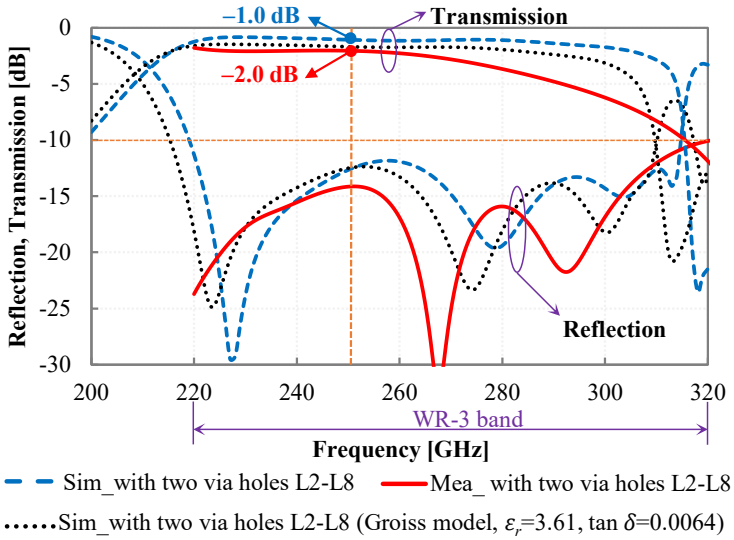

Figure 3.40 Simulated and measured scattering parameter results of the waveguide-to-differential-line transition.

The measured and simulated scattering parameters for the waveguide-to-differential-line transition are shown in Fig. 3.40. The measurement process used the WR-3 standard equipment, which covered the entire frequency band ranging from 220 to 320 GHz. The simulation results for the transition with two via-holes in L2–L8 indicate a bandwidth of reflection coefficient less than −10 dB, which spans 95.6 GHz (35.8%). The simulated transmission coefficient of the transition with two via-holes in L2–L8 at the center frequency of 250 GHz was −1.0 dB. Regarding the measured results, although the lower band edge could not be observed because of the limit of the WR-3 band, the bandwidth of reflection lower than −10 dB from the simulated lower band edge to the measured band edge was 100.0 GHz (37.0%). The measured transmission coefficient at the design frequency of 250 GHz was −2.0 dB. Furthermore, the measured result shows a bandwidth of transmission coefficient higher than −3 dB, measuring 63.0 GHz.

It is evident from the graph that the measured reflection coefficient shifted to lower frequencies and the reflection level was deferred. This shift can be attributed to the imperfections in the size and position of the via-hole as well as uneven substrate thickness. Furthermore, the measured dielectric constant of the fabricated substrate exceeded the reference value provided in the datasheet, with a value of approximately 3.6 at 250 GHz. The measured reflection level at a high resonant frequency is higher than the simulation. The reflection level decreases due to transmission loss. This discrepancy could be attributed to imperfections in the size and placement of the patch, as well as misalignment between layers during the fabrication process.

The measured transmission coefficient results differ from the simulation results mainly because of the surface roughness of the copper sticking to the substrate. The average surface roughness (*Ra*) utilized in fabrication was approximately 0.3 μm. *Ra* is the arithmetic average of the absolute values of the profile heights over the evaluation length. This information was sourced from the fabrication company. The skin depth on the copper surface was 0.13 μm based on the theoretical calculations performed at 250 GHz, which is nearly the same dimension as the surface roughness. Therefore, it is suggested that surface roughness significantly influences conductor loss. Additionally, the measured loss tangent of the fabricated substrate exceeded the reference value provided in the datasheet, with a value of approximately 0.01 at 250 GHz. The relative permittivity and loss tangent of the substrate were determined using the Fabry-Perot resonator method within the frequency range of 220 GHz to 320 GHz. Furthermore, multiple factors including fabrication tolerance and mechanical assembly errors can decrease the transmission coefficient. These factors are critical in the THz frequency bands, particularly when dealing with multilayered structures. For surface roughness analysis, HFSS offers a modified version of the Morgan-Hammerstad empirical fit, referred to as the Groiss equation. The Groiss model [11] assumes that the high-frequency current adheres to the surface profile. This adherence is measured by deviations in the direction of the normal vector from its ideal form. Large deviations indicate a rough surface, while small ones suggest a smooth surface. The simulation results integrate a Groiss model with an average surface roughness (*Ra*) of 0.3 μm, as the actual value from the fabrication is not available. Coupled with the measured dielectric constant of 3.6 and a loss tangent of 0.01, they are depicted by the black dotted line in Fig. 3.40. It can be observed that surface roughness and loss tangent affect the transmission, particularly at high frequencies. It aligns with [10] that as the frequency increases, the loss tangent and the dielectric constant of the substrate also increase, resulting in an increase in loss at high frequencies. Moreover, an increase in the dielectric constant causes the reflection coefficient to shift to low frequencies.

Table 3.3 Comparison of waveguide-to-microstrip transition

Ref.	f_c (GHz)	BW_{rel} (%)	S_{11} (dB)	S_{21} (dB)	Interface	Structure
[12]	10.5	47.6	−15	−0.95	CPW	Back-to-Back
[13]	33	40.9	−18.5	−0.26	SSL	Single
[14]	33	44.0	−12	−0.34	SISL	Single
[15]	33	40.6	−15	−0.4	Differential	Single
[16]	80	20.2	−10	−1.92	Differential	Single
[17]	122	11.8	−10	−1.63	Differential	Back-to-Back
[18]	120	25.0	−10	−1.8	Differential	Single
[19]	60	20.0	−10	−0.8	Differential	Single
[20]	275	23.6	−10	−2.6	Differential	Single
This work	250	37.0	−10	−2.0	Differential	Single

Table 3.3 presents the performance comparison between the proposed waveguide-to-microstrip transition and previously published results. However, the design frequencies and techniques used in this paper differ from those of the proposed method. For instance, a transition from CPW to air-filled rectangular waveguide was proposed in [12]. A suspended strip line to air-filled rectangular waveguide transition was presented in [13], and a substrate-integrated suspended line (SISL) to rectangular waveguide transition was developed [14]. While these transitions exhibit a wide bandwidth, their operation is low frequencies. Therefore, comparisons with the most similar methods are provided to evaluate the effectiveness of this paper, focusing mainly on the waveguide-to-differential-line transitions [15]-[19], but the bandwidth is still not wide. For [20], the bandwidth of the reflections less than −10 dB was 66.3 GHz (23.6%) and the measured transmission coefficient for the single transition was −2.6 dB at 275 GHz. For this work, the frequency bandwidth of 100 GHz (37.0%) at the reference S_{11} below −10 dB was consistent with the waveguide standard of WR-3. The transmission coefficient of the single transition from the measured was −2.0 dB at 250 GHz and more than −3 dB at frequencies higher than 280 GHz. These results are comparable to those of other designs.

3.5 Summary

A grounded suspended coplanar waveguide (GSCPW)-to-waveguide transition in a multi-layer dielectric substrate using corrugation structures was developed. The feeding GSCPW is inserted into the waveguide on layer 2 of the dielectric substrate, forming the back-short type transition. A rectangular patch element is used to transmit to the waveguide. Concurrently, the corrugation structures are applied at the edges of the aperture on the middle layer to improve the transmission characteristics and extend the bandwidth. The corrugation structures can extend the bandwidth up to 12.2% compared to the transition without corrugation. The measured results show a bandwidth of the reflection coefficient less than −10 dB with a frequency band of 60.8 GHz (21.8%). The measured transmission coefficient at the center frequency of 275 GHz was −4.3 dB.

A broadband grounded coplanar waveguide (GCPW)-to-waveguide transition in a multi-layer dielectric substrate covering the 250-290 GHz band was developed. This transition consists of a GCPW line inserted from the broad wall of the waveguide that excites a double rectangular stacked patch located at the waveguide center. The corrugation structures are applied at the edges of the aperture on the middle layer. Broadband operation is achieved by using a double patch, corrugation structures, and a cavity formed by the via-hole arrangement surrounding apertures patterned in a multi-layer substrate. The transition geometries are optimized by electromagnetic simulation using a finite element method. The measured results show a bandwidth of the reflection coefficient less than −10 dB with a frequency band of 48.0 GHz (18.1%). The measured transmission coefficient at the center frequency of 275 GHz was −4.4 dB.

A multi-layer waveguide-to-differential-line transition with a circular cavity and triple circular patch was developed. The multi-layer waveguide-to-differential-line transition operates under a combination of triple-stacked patch arrangements and circular cavity structures. Concurrently, the optimized arrangement of via-holes can prevent electric field leakage efficiently and improve the transmission characteristic in a high-frequency band. The geometry of the transition was optimized through electromagnetic simulations using the finite element method. Measurements and simulations were implemented to evaluate the performance of the transition. The transition had a wide bandwidth of 100.0 GHz (37.0%). The multi-layer waveguide-to-differential-line transition measured with a circular cavity and triple patch showed a transmission coefficient of −2.0 dB at the center frequency of 250 GHz. Furthermore, the measured result shows a bandwidth of transmission coefficient higher than −3 dB, measuring 63.0 GHz. The measured performance confirmed the feasibility of the multi-layer waveguide-to-differential-line transition. It is suitable for applications in practical terahertz systems.

References

[1] C. Chokchai, H. A. Diawuo, Y. Sugimoto, K. Sakakibara and N. Kikuma, "Bandwidth Extension of GSCPW-to-Waveguide Transition in Multi-Layer Dielectric Substrate by Corrugation Structures in THz Band," *2022 Int. Symp. Antennas Propag. (ISAP)*, Sydney, Australia, 2022, pp. 559-560, doi: 10.1109/ISAP53582.2022.9998582.

[2] MITSUBISHI GAS CHEMICAL, "Non-haloganated Low CTE BT Resin Laminate for IC Plastic Packages", https://www.mgc.co.jp/eng/prod-ucts/sc/btprint/lineup/hfbt.html, (2022-07-18).

[3] HFSS. 2021 R1, Ansoft Corporation, Pittsburgh, PA, 2021.

[4] C. Chokchai, M. Yamazaki, H. A. Diawuo, K. Sakakibara, Y. Sugimoto, and N. Kikuma, "Design of GCPW-to-Waveguide Transition in Multi-Layer Dielectric Substrate with Single Patch and Corrugated Structures in 275 GHz Band," *IEICE Conferences Archives*, 2022.

[5] C. Chokchai, Y. Sugimoto, K. Sakakibara and N. Kikuma, "Broadband GCPW-to-Waveguide Transition in Multi-Layer Dielectric Substrate with Double Patch and Corrugation Structures in 275 GHz Band," *2023 IEEE Int. Symp. Antennas Propag. (ISAP)*, Kuala Lumpur, Malaysia, 2023, pp. 1-2, doi: 10.1109/ISAP57493.2023.10389096.

[6] C. Chokchai, Y. Sugimoto, K. Sakakibara, H. A. Diawuo and N. Kikuma, "Broadband Waveguide-to-Differential-Line Transition in Multi-Layer Substrates With Triple Stacked Patch in 300 GHz Band," *in IEEE Access*, vol. 12, pp. 49804-49816, 2024, doi: 10.1109/ACCESS.2024.3384606.

[7] S. Hara, R. Dong, S. Lee, K. Takano, N. Toshida, A. Kasamatsu, K Sakakibara, T. Yoshida, S. Amakawa, and M. Fujishima, "A 76-Gbit/s 265-GHz CMOS Receiver With WR-3.4 Waveguide Interface," *IEEE J. Solid-State Circuits*, vol. 57, no. 10, pp. 2988-2998, Oct. 2022, doi: 10.1109/JSSC.2022.3179560.

[8] K. Feng, T. Spencer and J. Watkowski, “Integrated metallization system for high density interconnects and modified semi additive processing,” *2013 8th Int. Microsystems Packag. Assem. Circuits Techn. Conf. (IMPACT)*, Taipei, Taiwan, 2013, pp. 241-244, doi: 10.1109/IMPACT.2013.6706700.

[9] Anritsu Company. Calibration and Measurement Guide VectorStarTM MS464xB Series Microwave Vector Network Analyzer. Accessed: Nov. 18, 2022, Chap. 14. [Online.] Available: https://dl.cdn-anritsu.com/en-us/test-measurement/files/Manuals/Measurement-Guide/10410-00318AE.pdf.

[10] Y. Morishita K. Takahashi, R. Hasaba, T. Murata, K. Takinami, H. Kitamura, U. Sangawa, T. Tomura, and I. Watanabe, “Comparison between Microstrip-line and Substrate Integrated Waveguide on Package Substrate in 170 GHz and 300 GHz Bands,” *2022 Asia-Pacific Microw. Conf. (APMC)*, Yokohama, Japan, 2022, pp. 196-198, doi: 10.23919/APMC55665.2022.9999775.

[11] S. Groiss, I. Bardi, O. Biro, K. Preis and K. R. Richter, “Parameters of lossy cavity resonators calculated by the finite element method,” *IEEE Trans. Magn*., vol. 32, no. 3, pp. 894-897, May 1996, doi: 10.1109/20.497385.

[12] Y. Zhao, J. Dong, F. Yin, X. Fang, and K. Xiao, “Broadband Coplanar Waveguide to Air-Filled Rectangular Waveguide Transition,” *Electron*., vol. 11, no. 7, Mar. 2022, doi: 10.3390/electronics11071057.

[13] J. Dong, H. Peng, Y. Liu, H. Lin, and T. Yang, “Broadband Suspended Stripline to Air-Filled Rectangular Waveguide Transition,” *Electron. Lett*., vol. 51, no. 23 pp. 1886-1888, Nov. 2015, doi:10.1049/el.2015.2743.

[14] Y. Chen, K. Ma and Y. Wang, “A Ka-Band Substrate Integrated Suspended Line to Rectangular Waveguide Transition,” *in IEEE Microw. Wireless Compon. Lett*., vol. 28, no. 9, pp. 744-746, Sept. 2018, doi: 10.1109/LMWC.2018.2849203.

[15] Z. Yang, T. Yang, Y. Liu, and H. Peng., "A compact and broadband differential microstrip line to rectangular waveguide transition using dipole antenna," *J. Infrared Milli Terahz Waves*, vol 37, pp. 582–591, 2016, doi: 10.1007/s10762-016-0253-1.

[16] T. Yuasa, T. Oba, Y. Tahara, Y. Morimoto, T. Owada and M. Miyazaki, "A millimeter wave wideband differential line to waveguide transition using short ended slot line," *in Proc. IEEE 44th Eur. Microw. Conf.*, pp. 1004-1007, 2014, doi: 10.1109/EuMC.2014.6986607.

[17] R. Hasan, W. A. Ahmed, J. Lu, H. J. Ng, and D. Kissinger, "F -band differential microstrip patch antenna array and waveguide to differential microstrip line transition for FMCW radar sensor," *in IEEE Sensors J.*, vol. 19, no. 15, pp. 6486-6496, Aug., 2019, doi: 10.1109/JSEN.2019.2909935.

[18] P. Hügler, T. Chaloun and C. Waldschmidt, "A wideband differential microstrip-to-waveguide transition for multilayer PCBs at 120 GHz," *in IEEE Microw. Wireless Compon. Lett.*, vol. 30, no. 2, pp. 170-172, Feb. 2020, doi: 10.1109/LMWC.2019.2958208.

[19] S. Churkin, A. Mozharovskiy, A. Myskov, A. Artemenko, and R. Maslennikov, "Top-layer wideband transition from waveguide to planar differential line for 60 GHz applications," *in Proc. IEEE 48th Eur. Microw. Conf. (EuMC)*, pp. 663-666, 2018, doi: 10.23919/EuMC.2018.8541701.

[20] M. Yamazaki, Y. Sugimoto, K. Sakakibara, and N. Kikuma, "Broadband differential-line-to-waveguide transition in multi-layer dielectric substrates with an X-shaped patch element in 280 GHz band," *in IEEE Trans. Microw. Theory Techn.*, vol. 71, no. 6, pp. 2616-2624, Jan. 2023, doi: 10.1109/TMTT.2022.3232501.

Chapter 4

Narrow-Wall-Inserted Planar-Line-to-Waveguide Transition in Multi-layer Substrates

This chapter employed a V-shaped patch element to efficiently couple the microstrip line currents along a narrow waveguide wall, building upon previous study [1]. However, that design was tailored for a single substrate operating at 76.5 GHz with a narrow bandwidth. Therefore, this study presents a broadband tapered GCPW-to-waveguide transition for the 270 GHz band in multi-layer substrates. The transition was designed within the fabrication constraints of the metal pattern and via-hole arrangement at the 270 GHz band. Broadband operation is achieved by combining stacked patches and multiple resonance techniques within the cavity. The modified V-shaped and double-stacked rectangular patches facilitate multiple resonances, while the arrangement of apertures and via-holes contributes to cavity formation. Notably, the design effectively addresses fabrication limitations in the terahertz frequency band [2].

4.1 Configuration of the Narrow-Wall-Inserted Planar-Line-to-Waveguide Transition

This section describes the configuration and principles of the narrow-wall-inserted planar-line-to-waveguide transition method. In the conventional planar-line-to-waveguide transition employing a rectangular patch, the microstrip line typically resides on the broad wall of the waveguide [3], [4], [5]. In this setup, the current on the rectangular patch element aligns solely with the E-plane of the waveguide, running parallel to the microstrip line and facilitating effective coupling. However, achieving effective coupling between the patch and the microstrip line on the narrow wall of the waveguide poses challenges. The current in the patch element is stimulated by the electromagnetic field within the waveguide, necessitating both x and y components. To meet this requirement, a V-shaped patch was used to feed from the narrow-wall side of the waveguide [1]. The current on the V-shaped patch element bifurcates in two directions along the side edge. Consequently, the current on the V-shaped patch element generates a component parallel to the microstrip line, thereby achieving effective coupling.

Multi-layer substrates were selected for this transition design due to their capacity to provide broadband performance across a wide frequency range while ensuring low insertion loss. Multi-layer substrates offer versatility for integrating various passive and active components, enhancing the overall functionality and efficiency of the design. Furthermore, the core materials employed in the substrate allow for intricate circuit modifications, often requiring multiple routing layers. This transition was developed to establish a connection between the 265 GHz CMOS circuit receiver and the WR-3.4 waveguide interface in multi-layer substrates [6]. The multi-layer substrates comprise eight copper plates separated by seven dielectric plates, with three prepreg layers on each side of the core layer. It is manufactured through a high-pressure heating process. The modified semi-additive process (MSAP) is employed to produce micropatterns with fine pitch [7]. Following the application of a 4 μm nickel layer onto the copper plate interface, the metal patterns undergo a plating process resulting in a 0.05 μm gold layer. MSAP forms rounded corners at the edges of the metal patterns, and the corner's radius is 10 μm. The accuracy of the metal patterns on the same layer is maintained at 10 μm, while on different layers, it is 25 μm.

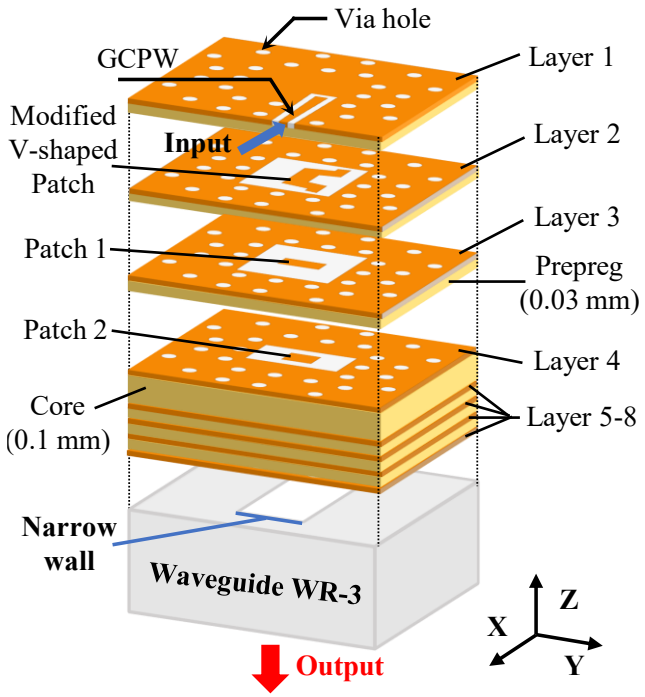

Figure 4.1 Configuration of the narrow-wall-inserted planar-line-to-waveguide transition.

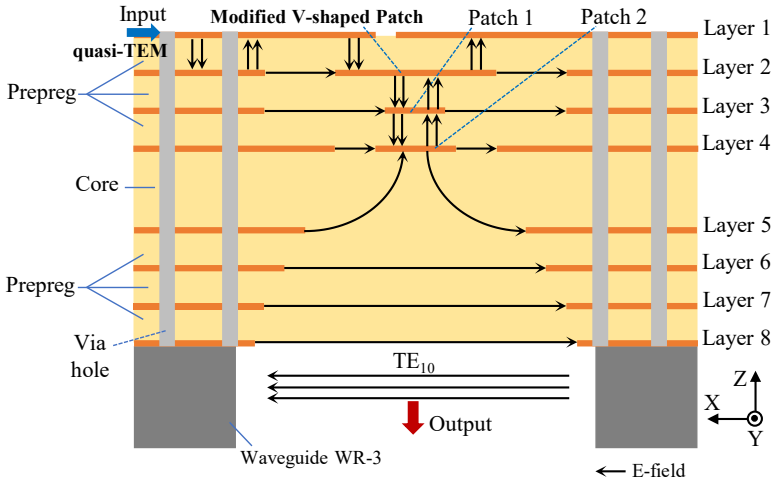

Figure 4.2 Cross-sectional view and mode transformation of the transition.

The transition features a single-ended line placed on the top layer of multi-layer dielectric substrates, with a modified V-shaped patch element located in Layer 2. Rectangular patches 1 and 2 were mounted on layers 3 and 4, respectively, as shown in Fig. 4.1. A via-hole arrangement surrounds a tapered grounded coplanar waveguide. Moreover, double lines of via-hole are strategically arranged to prevent leakage of the parallel plate mode within the substrates. The multi-layer substrates are aligned over the aperture of a metal waveguide (WR-3, 0.864 × 0.432 mm^2). The excitation of the electric field from the quasi-TEM mode to the TE_{10} mode demonstrates the principle of the planar-line-to-waveguide transition. Fig. 4.2 illustrates the mode conversion mechanism of the electric field through the transition, visualized by the electric field lines. The GCPW operating in the quasi-TEM mode, is inserted into the waveguide region from its narrow wall. A modified V-shaped patch on the second layer near the signal line is electromagnetically excited. Subsequently, the electric field couples from the modified V-shaped patch to Patch 1, and then to Patch 2. Consequently, Patch 2 radiates the TE_{10} mode into the waveguide.

The configuration of the modified V-shaped patch is adopted from a standard rectangular patch with width W and length L, located at the waveguide's center on Layer 2. Initially, orthogonal triangles with a vertex angle θ = 10 deg. are removed from both lengths L of the original rectangular patch. Subsequently, trapezoids with length W_C, height L_C (perpendicular distance between these sides), and angle θ are subtracted from the top of the patch's width W sides, forming the V-shaped patch element. This V-shaped patch undergoes further modification by subtracting a parallelogram with length W_P, height L_P, and angle θ at both

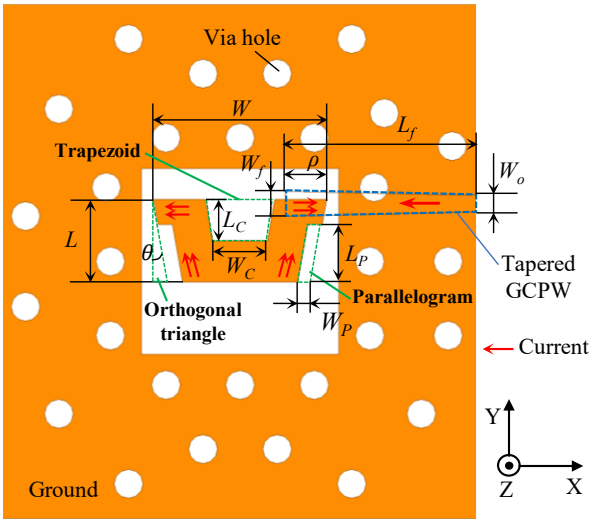

Figure 4.3 Current distribution on the modified V-shaped patch and tapered GCPW.

length L sides of the V-shaped patch to achieve a wideband transition, as shown in Fig. 4.3. To enhance the coupling between the modified V-shaped patch and the microstrip line, a tapered GCPW is used. The configuration ensures that the sides of the modified V-shaped patch overlap with the wider side W_f and the narrower side connecting to the port Wo, facilitating a seamless connection with the IC chip.

The geometric parameters of the proposed transition, shown in Fig. 4.4, demonstrate symmetry across the waveguide's center in the XZ-plane. The optimization of all transition parameters was optimized through electromagnetic simulations. To prevent parallel-plate mode leakage across all-metal planes, via-holes with a diameter of 70 μm were strategically arranged around the waveguides, spaced at a center-to-center distance of 180 μm. The manufacturing tolerance for the via-hole positioning is ±25 μm, while the diameter variation is ±20 μm. The substrate utilized in this design employs HL972LF-LD [8] (Mitsubishi Gas Chemical Company, Inc.), which has a dielectric constant (ε_r) of 3.5 and a loss tangent (tan δ) of 0.003. This multi-layer configuration comprises a core layer with a 100 μm thickness and prepreg layers each 30 μm thick. Thickness variances for the core and prepreg layers are ±15 μm and ±10 μm, respectively. The copper plate used in the substrate has a thickness of 15 μm, with a conductivity (σ) of 5.8×10^7 S/m and a thickness variation of ±7 μm. The substrate production was undertaken by CONNECTEC JAPAN Corporation.

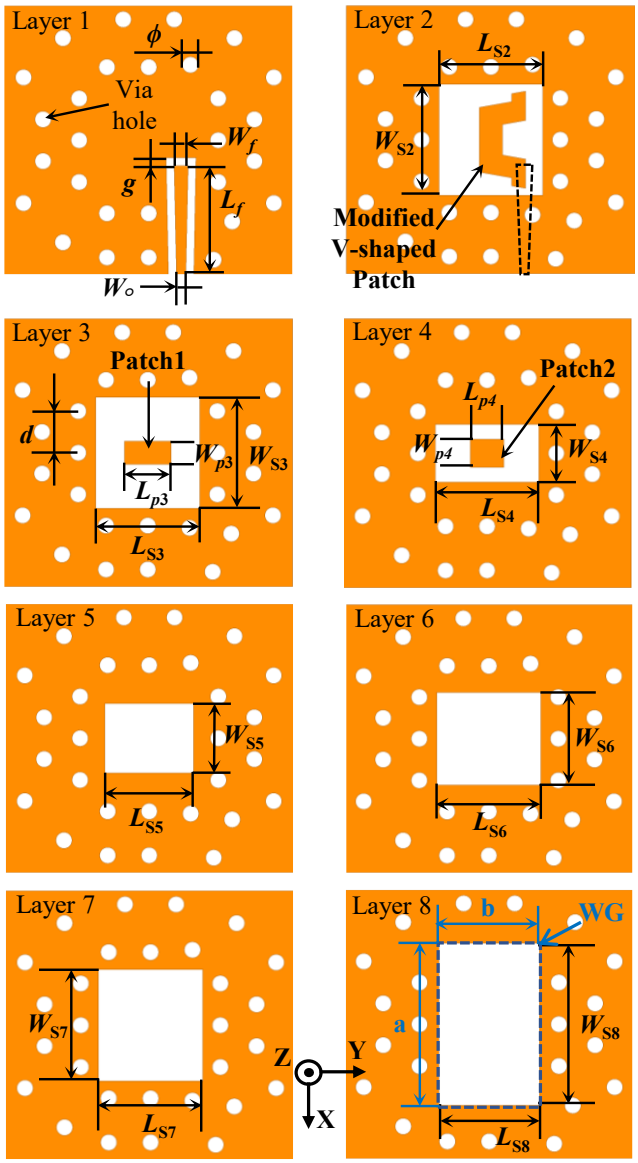

Figure 4.4 Top views of each layer with the parameters for the narrow-wall-inserted planar-line-to-waveguide transition.

To ensure wideband matching, the design strategy combines a modified V-shaped patch, stacked patches, tapered GCPW, and multiple resonances of the cavity. Also, all geometrical parameters were optimized. The dimensions of the modified V-shaped patch are key to regulating the coupling between the signal line and the resonant frequencies. A critical aspect of this design is the cutting angle θ of the modified V-shaped patch, which significantly affects the coupling intensity and orientation of the patch's corners. Optimizing θ is essential for achieving an equilibrium between effective coupling and targeting specific resonant frequencies.

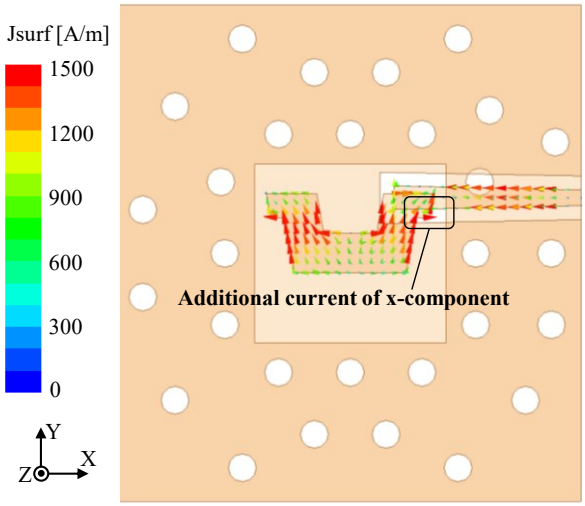

Figure 4.5 Simulated current vector distribution on the GCPW feed line and modified V-shaped patch at 275 GHz.

Furthermore, this parameter plays a pivotal role in determining the polarization of the radiated signal in the TE_{10} mode, underscoring its impact on the transition's overall performance. Incorporating double-stacked rectangular patches plays a crucial role in expanding the bandwidth. The patch dimensions directly affect the transition's capacitance and how effectively the electric field couples from the modified V-shaped patch into the waveguide. Fine-tuning the sizes of patches 1 and 2 is a key strategy for improving impedance matching. Moreover, the design of the apertures across all metal layers aims to create a cavity around the patch, promoting low-Q resonance and enabling a broader bandwidth. The extensions of layers from 5 to 8 are tapered fashion resembling a horn antenna, facilitating the generation of multiple resonances and ensuring smooth radiation into the waveguide. Based on these principles, the transition was designed to cover a wideband range of 248–308 GHz.

The simulated current vector distributions on the tapered GCPW and modified V-shaped patch element at 275 GHz, as illustrated in Fig. 4.5, reveal effective excitation of the current vector distributions on the modified V-shaped patch through coupling with the signal line. Consequently, a significant x-component of current was observed to flow prominently from the patch corners, underscoring the presence of an additional x-component current at the cut portions of the modified V-shaped patch element, alongside the current flowing along the top edge. Fig. 4.6 illustrates the electric field distributions across layers 1–4, providing valuable insights into the structure's behavior. The visualization highlights the robust excitation of the

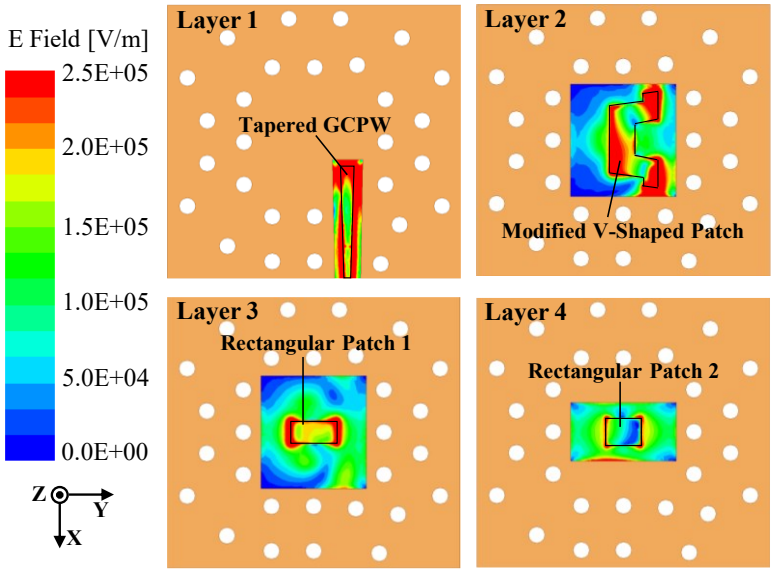

Figure 4.6 Simulated electric field distribution on Layer 1 to Layer 4 of the transition at 275 GHz.

modified V-shaped patch through coupling from the signal line and subsequent coupling to patches 1 and 2. This process facilitates the mode conversion from the signal line to the waveguide, achieved through the resonance of the modified V-shaped and double-stacked rectangular patches. Specifically, the quasi-TEM mode of the signal line undergoes conversion to the TE_{10} mode, enabling its propagation within the waveguide.

4.2 Simulation Results and Discussion

This section examines the reflection characteristics of the proposed transitions relying on simulated parameters. The electromagnetic simulator ANSYS HFSS [9], employing the finite element method, was utilized for the simulation. A wide bandwidth, controllable via multiple resonant frequencies, is deemed essential. The objective was to enhance the resonance bandwidth to achieve less than −10 dB for a center frequency of 275 GHz. Section 4.1 elaborates on the fundamental principles of this transition. Herein, a parameter simulation was conducted to explore the critical aspects of the wideband design of the transition.

The dimensions *Wo* and *g* of the tapered grounded coplanar waveguide were designed for a characteristic impedance of 50 Ω. Furthermore, to achieve a wide bandwidth, the width of the tapered grounded coplanar waveguide W_f and the length of the tapered grounded coplanar waveguide L_f are also inserted into the waveguide. Figure 4.7 compares the reflection coefficients from simulation results between with and without tapered GCPW. The results demonstrate that tapered GCPW enhances the impedance matching of transitions. This improvement is attributed to the increased overlap area between the modified V-shaped patch and the transmission line when enlarging the size of W_f, leading to a more robust coupling from the transmission line to the modified V-shaped patch.

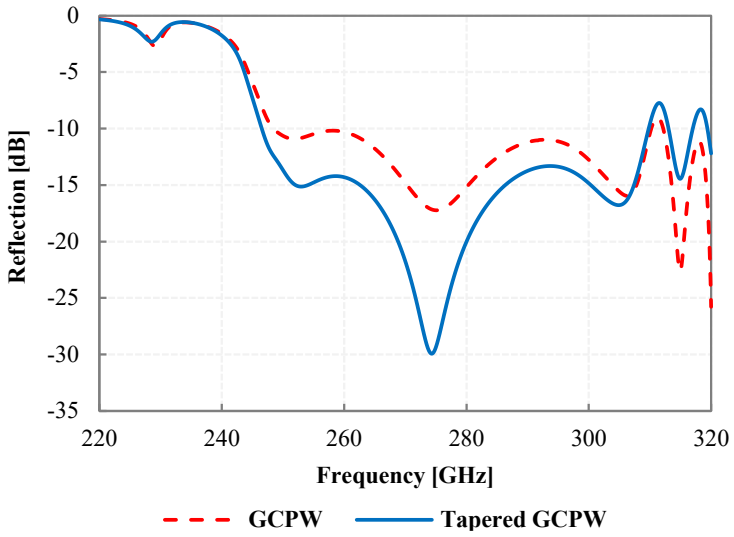

Figure 4.7 Comparison of reflection characteristics of the transition with and without tapered GCPW.

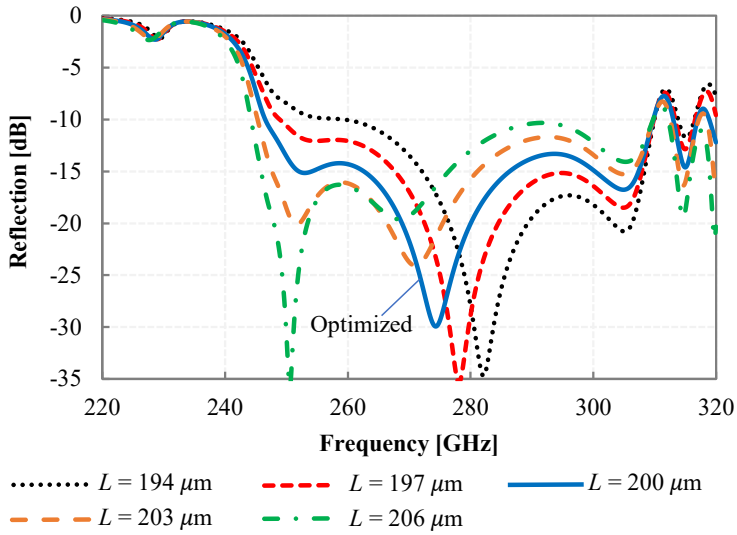

Figure 4.8 Reflection characteristics of the narrow-wall-inserted planar-line-to-waveguide transition depending on L.

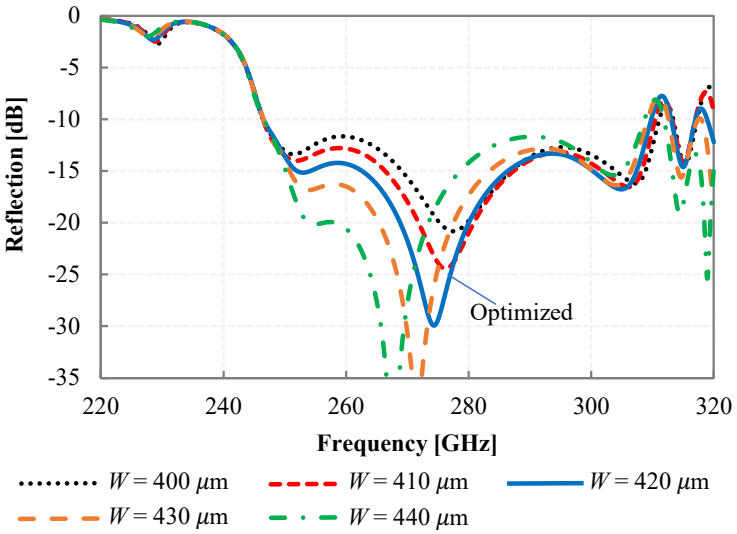

Figure 4.9 Reflection characteristics of the narrow-wall-inserted planar-line-to-waveguide transition depending on W.

The critical parameters of the modified V-shaped patch were analyzed to achieve wideband operation. An important parameter for controlling the resonant frequencies is the length of the modified V-shaped patch length, denoted as L, representing the overall length of the V-shaped patch. As shown in Fig. 4.8, the center resonant frequency decreases with an increase in the value of L. This phenomenon occurs because the path length of the current flowing through the patch exceeds half the wavelength of the design frequency. Furthermore, parameter L significantly influences the degree of overlap between the modified V-shaped patch and the

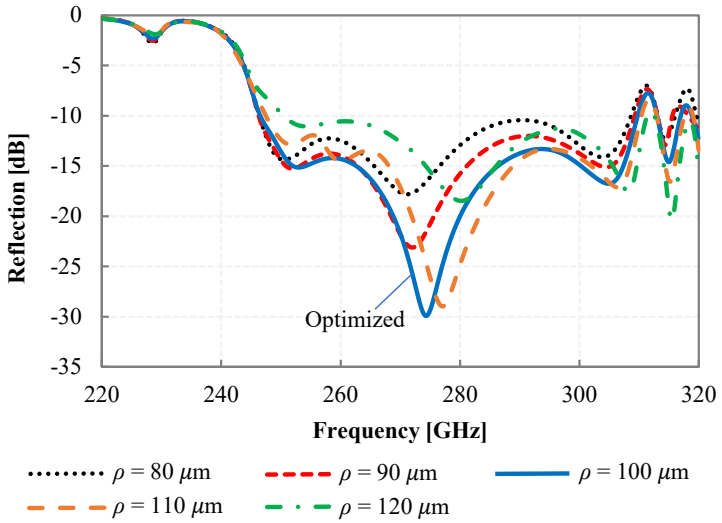

Figure 4.10 Reflection characteristics of the narrow-wall-inserted planar-line-to-waveguide transition depending on ρ.

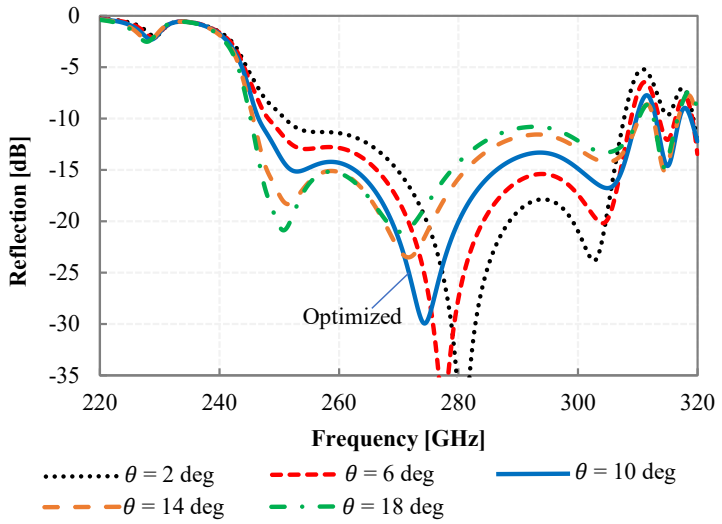

Figure 4.11 Reflection characteristics of the narrow-wall-inserted planar-line-to-waveguide transition depending on θ.

transmission line, thereby exerting a pronounced effect on impedance matching. The reflection coefficient level at higher frequencies increases with an increase in L. Therefore, the optimal value for L was determined to be 200 μm.

Furthermore, the width W, overlap length ρ, and cut angle θ of the modified V-shaped patch significantly influence the coupling between the signal lines and the patch. Fig 4.9 shows the dependency of the reflection coefficient on the width W of the modified V-shaped patch. It was observed that reducing W decreased the reflection coefficient level at a lower resonant

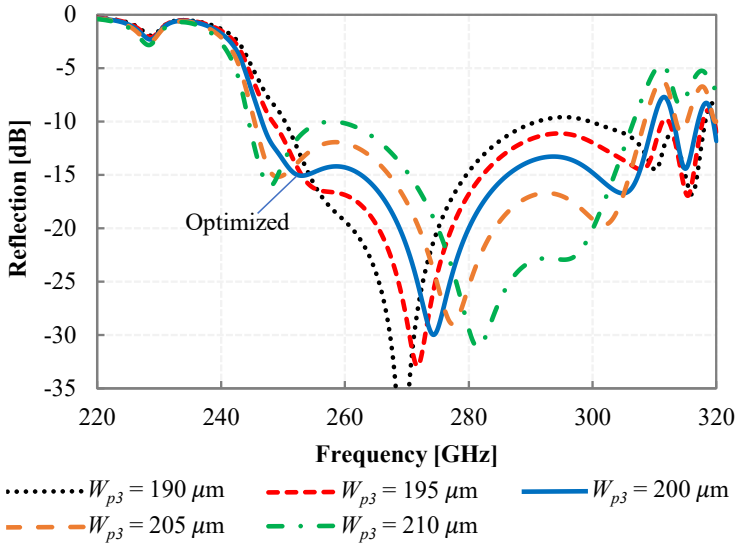

Figure 4.12 Reflection characteristics of the narrow-wall-inserted planar-line-to-waveguide transition depending on W_{p3}.

frequency. The overlap length ρ was optimized at 100 μm for appropriate coupling. Fig. 4.10 shows the reflection characteristics of the transition depending on ρ. As ρ increases, the reflection coefficient level improves, attributed to the increased overlap length ρ and strengthened coupling. This improvement can be attributed to the intensified coupling between the transmission line and the modified V-shaped patch. Therefore, the cut angle θ of the modified V-shaped patch is crucial as it affects the direction of the corner and the coupling strength. Fig. 4.11 indicates that θ influences the reflection coefficient level at the resonant frequency. Increasing θ weakens the coupling and elevates the reflection coefficient level. Although multiple resonances contribute to expanding the bandwidth of reflections below −10 dB, slight shifts in the resonant frequency may occur with changes in θ. Therefore, precise control of the resonant frequencies is necessary for achieving a wide bandwidth.

Double-stacked rectangular patches were incorporated to enhance the bandwidth. The dimensions of these patches are pivotal for facilitating the coupling of the electric field from the modified V-shaped patch into the waveguide. Patch 1 was mounted on Layer 3 below the modified V-shaped patch, playing a role in impedance matching. Patch 1 provides electric field coupling from the modified V-shaped patch to Patch 2 in Layer 4. The width of Patch 1 (W_{p3}), which influences both the center and high resonance frequencies, as well as the transition impedance matching of the transition, is shown in Fig. 4.12. When W_{p3} is increased, the center resonant frequency shifts towards higher frequencies, and the reflection coefficient level at lower frequencies increases. The optimum value for W_{p3} is 200 μm. Furthermore, Patch 2,

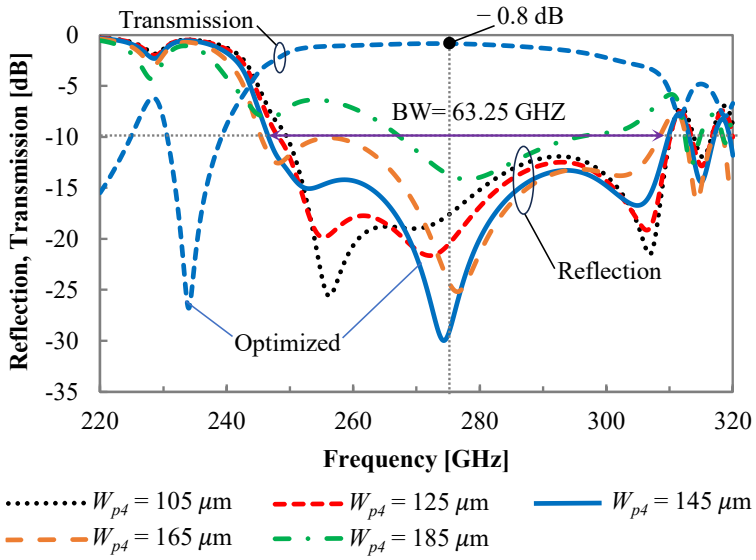

Figure 4.13 Reflection characteristics of the narrow-wall-inserted planar-line-to-waveguide transition depending on W_{p4}.

situated on Layer 4, plays a significant role in coupling the electric field received from Patch 1 to propagate into the waveguide. Patch 2 affects the impedance matching of the transitions because its position parallel to Patch 1 affects capacitance when adjusting the patch size. The width of Patch 2 (W_{p4}) impacts the reflection coefficient level of the resonant frequency band. As depicted in Fig. 4.13, decreasing W_{p4} results in an improvement in the reflection coefficient level. Additionally, the center resonant frequency exhibits a slight shift with W_{p4} variations. Therefore, the optimum value for W_{p4} was determined to be 145 μm.

The following conclusions can be drawn from the study of the parameters: The center frequency can be effectively controlled by adjusting the values of L, θ, and W_{p4}. The low frequency can be controlled by adjusting the value of W. High-frequency performance can be controlled by adjusting the value of W_{p3}. Control of impedance matching with minimal impact on resonance frequency can be achieved by varying ρ. The optimal design parameters obtained through electromagnetic simulation are presented in Table 4.1, and the transmission and reflection characteristics of these parameters are shown in Fig. 4.13. Consequently, the combination of modified V-shaped and double-stacked rectangle patches with multiple resonances exhibits broadband characteristics. Furthermore, the bandwidth of the reflections less than −10 dB was 63.25 GHz. At the design frequency of 275 GHz, the transmission loss was 0.8 dB.

Table 4.1 Optimized parameters of the narrow-wall-inserted planar-line-to-waveguide transition

Name	Description	Value
ϕ	Diameter of via	70 μm
d	Space between vias	180 μm
W_f	Width of the tapered signal line	60 μm
L_f	Length of the tapered signal line	47 μm
W_o	Width of the signal line	40 μm
G	Gap between signal line and coplanar ground	35 μm
W	Width of the V- shaped patch element	420 μm
L	Length of the V- shaped patch element	200 μm
W_c	Width of the cut patch element	132.5 μm
L_c	Length of the cut patch element	100 μm
W_p	Width of the cut V-shaped patch element	35 μm
L_p	Length of the cut V-shaped patch element	140 μm
θ	Patch cut angle	10 deg
W_{P3}	Width of rectangular patch 1	100 μm
W_{P4}	Width of rectangular patch 2	120 μm
L_{P3}	Length of rectangular patch 1	200 μm
L_{P4}	Length of rectangular patch 2	145 μm
W_{S2}, W_{S3}, W_{S7}	Width of layer 2, 3, and 7's window	480 μm
W_{S4}	Width of layer 4's window	250 μm
W_{S5}	Width of layer 5's window	300 μm
W_{S6}	Width of layer 6's window	400 μm
W_{S8}	Width of layer 8's window	700 μm
L_{S2}, L_{S3}, L_{S4}, L_{S6}, L_{S7}	Length of layer 2, 3, 4, 6, and 7's window	450 μm
L_{S5}	Length of layer 5's window	385 μm
L_{S8}	Length of layer 8's window	432 μm

4.3 Experimental Performances

The accuracy of the proposed transition simulation was validated by measuring the transmission losses and reflection characteristics of the fabricated transitions. The measurement setup is shown in Fig. 4.14. For the waveguide measurements, a back-to-back configuration was established on the substrate. Consequently, two identical transitions with the same geometric parameters were connected to the fabricated substrate (device under test: DUT) via a single-ended line. To facilitate connection to the flange of the standard waveguide for measurement, the DUT was securely mounted on a metal jig with waveguides at both terminals. A choke structure was implemented around the waveguide on the surface of the jig to minimize leakage from the gap between the DUT and the jig. The DUT was meticulously positioned using 1 mm diameter microscrews to ensure precise alignment. The measurement accuracy was validated by repeating the assembly and measurement procedures. Millimeter-wave extension modules (VDI WR-3.4- VNAX) were interfaced with an ANRITSU MS4647B vector network analyzer. The two ports of the standard waveguides extending from the millimeter-wave modules underwent calibration using the WR-3 waveguide Anritsu Calibration Kit Model SM6567 at the planes connected to the waveguide in the metal jig. The reflection and transmission characteristics were measured, covering the waveguide within the jig and the transmission lines between the two transitions.

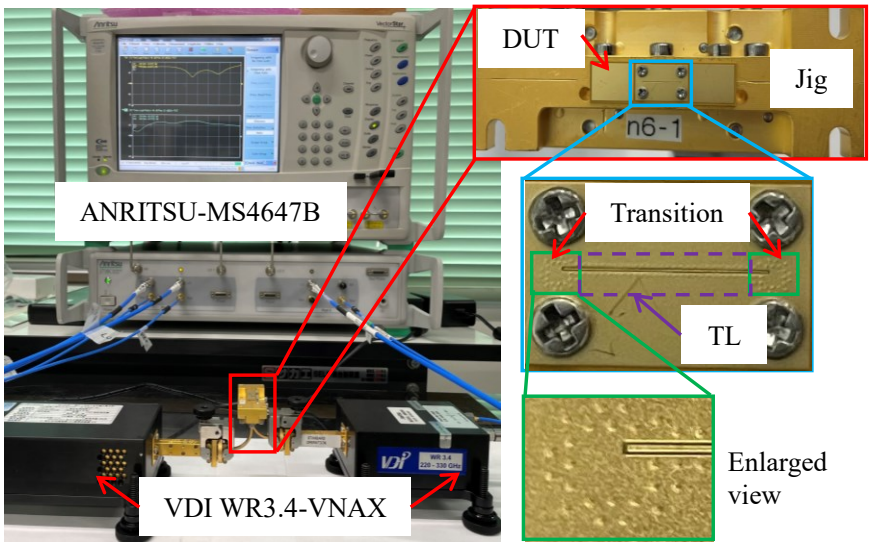

Figure 4.14 Experimental setup of the narrow-wall-inserted planar-line-to-waveguide transition with the waveguide jig in the WR-3 band.

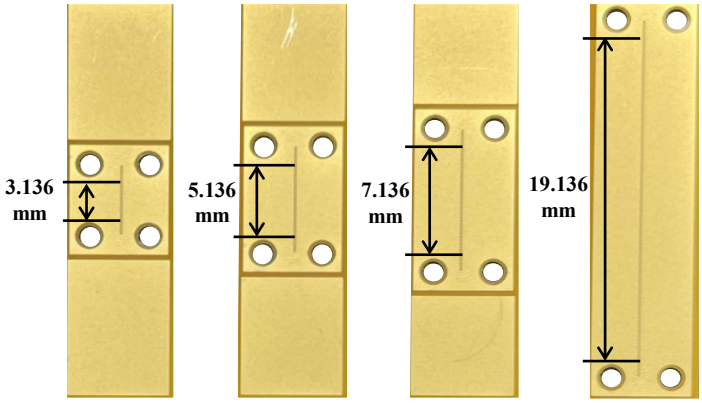

Figure 4.15 Fabricated substrates (DUT) for different lengths of the transmission line.

To mitigate the effects of multiple reflections, a gating function in the time domain integrated into the vector network analyzer was used to measure the scattering parameters [10]. The entire frequency band of WR-3, spanning 220–320 GHz, was utilized to ensure a high time resolution.

To accurately assess the insertion loss of each transition, the losses of the single-ended line between the transitions and the waveguide in the jig were measured to obtain compensation. DUT of the transitions, connected by single-ended lines of varying lengths, as depicted in Fig. 4.15, were fabricated for different parameter combinations. Two transitions were connected via a transmission line, and four different lengths (3.136, 5.136, 7.136, and 19.136 mm) were utilized to measure the transmission loss of the line. The length of the transmission line was defined as the distance between the narrow waveguide walls of the two transitions. Fig. 4.16 shows the transmission using single-ended lines of 3.136, 5.136, 7.136, and 19.136 mm at 260, 275, and 290 GHz, respectively. By examining the slopes of the curves, the transmission loss at 275 GHz was estimated to be 0.85 dB/mm. The metal jig loss was measured and calculated following the techniques implemented in [11]. Fig. 4.17 shows the individual losses of each part for estimating the insertion loss of a single transition. The measured transmission of the back-to-back transition with a transmission line of 3.136 mm, including all the losses from Port 1 to Port 2, is indicated by the blue dashed line. The purple solid line represents the loss in the 3.136 mm transmission line, estimated from the difference in the measured transmissions for back-to-back transitions of varying lengths. The black dashed line represents the transmission with waveguide loss in the jig obtained via jig measurements. To determine the jig loss, two identical jigs were interconnected, and their losses were measured, resulting in 1.8 dB at 275 GHz. By dividing the measured transmission of the two jigs by two, the loss of a single jig was

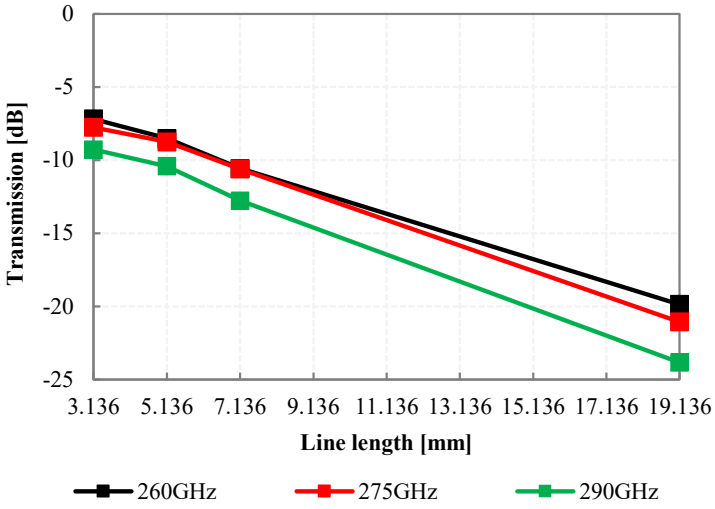

Figure 4.16 Measured transmission coefficients of the fabricated transition with four different line lengths.

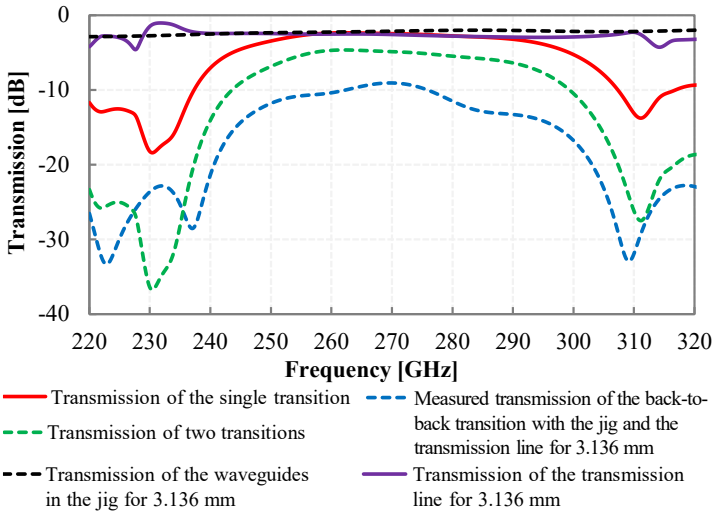

Figure 4.17 Loss and transmission characteristics at each correction process of the fabricated transition.

estimated to be 0.9 dB. Finally, the transmission coefficient of a single transition was evaluated from the transmission of the entire structure with a transmission line of 3.136 mm, by de-embedding the jig and transmission line losses.

A comparison between the measured results of the transmittance and reflection coefficients, estimated by compensating for the total losses, and the simulated results is shown in Fig. 4.18. The red solid lines represent the measured results, while the black dashed lines represent the simulated results. The simulation of the proposed transition showed a bandwidth of the reflection

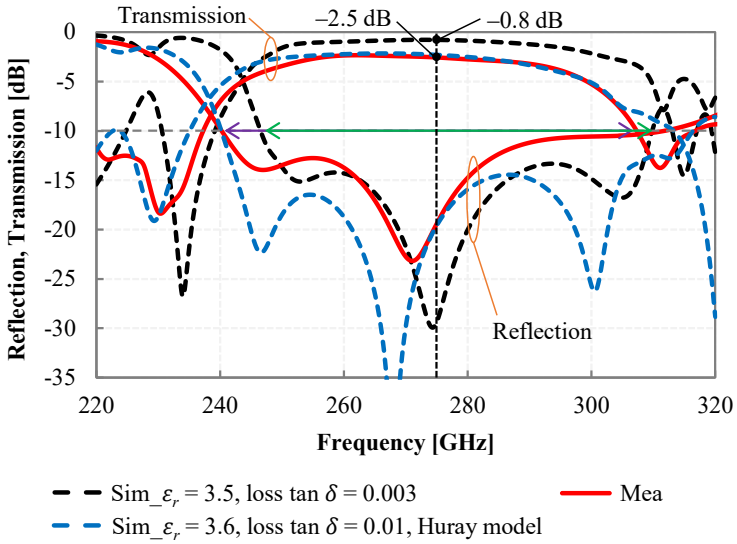

Figure 4.18 Measured and simulated reflection and transmission coefficients of the narrow-wall-inserted planar-line-to-waveguide transition.

coefficient below –10 dB of 63.25 GHz (22.7%). At a center frequency of 275 GHz, the simulated transmission coefficient is –0.8 dB. In contrast, the measured results demonstrate a bandwidth of the reflection coefficient below –10 dB with a frequency range of 71.50 GHz (26.1%). The measured transmission coefficient at the center frequency of 275 GHz was –2.5 dB. It is noteworthy that the measured lower resonant frequency is 8.25 GHz lower than the simulation. This frequency shift resulted in an increase of approximately 3 dB in the reflection level near the middle frequency, contributing to an expanded bandwidth.

The graph clearly shows that transitions measured reflection coefficient results exhibit a shift toward lower frequencies, and the level of reflection coefficient defers. These frequency shifts and reductions in the reflection coefficient can be attributed to imperfections in the size and position of the via-hole and irregular substrate thickness. Furthermore, the measured dielectric constant of the fabricated substrate exceeded the reference value provided in the datasheet, registering approximately 3.6 at 275 GHz.

The measured transmission coefficient results differ from the simulation results primarily due to the surface roughness of the copper adhered to the substrate. Surface roughness profiles are commonly characterized by a 10-point mean roughness (R_Z) on both sides. The R_Z from the fabrication company was approximately 1.4 μm. At 275 GHz, theoretical calculations indicate a skin depth of 0.12 μm on the copper surface attached to the substrate, almost the same as the surface roughness dimension. Therefore, it was suggested that surface roughness significantly influences conductor loss. Furthermore, the measured loss tangent of the fabricated substrate exceeded the reference value provided in the datasheet, with a value of approximately 0.01 at

275 GHz. The dielectric constant and loss tangent of the substrate (HL972LF-LD) were determined using the Fabry-Perot resonator method within the frequency range of 220 GHz to 320 GHz.

ANSYS HFSS employs the Huray model for surface roughness analysis, renowned for its high accuracy in modeling surface irregularities [12]. This model is based on a random distribution of spheres, resembling "snowballs," arranged pyramid-like over a flat plane area [13]. Two critical input parameters required by ANSYS HFSS tools are the nodule radius (r) and Hall-Huray surface ratio (S_r). In [14], the nodule radius is calculated using the formula $r = 0.06R_Z$, yielding a value of 0.084 μm. The Hall–Huray surface ratio was defined as the surface area of the spheres divided by the base area. In the Cannonball model, N was consistently set to 14 spheres, and the base area (A_{flat}) was invariably $36r^2$. Since r^2 cancels out, S_r can be simplified to $1.56\pi = 4.9$. The simulation results incorporate a Huray model with a nodule radius of 0.084 μm and a Hall-Huray surface ratio of 4.9. Complemented by the measured dielectric constant of 3.6 and a loss tangent of 0.01, these results are represented by the blue dashed line in Fig. 4.18. Notably, the influence of surface roughness and loss tangent on transmission is evident, particularly at higher frequencies. Furthermore, an increase in the dielectric constant is observed to shift the reflection coefficient towards lower frequencies.

Table 4.2 presents a performance comparison between the proposed planar-line-to-waveguide transition and the previously published works. It is important to note that the design frequencies and techniques used in each work varied, making direct comparison challenging. To evaluate the effectiveness of this paper, particular attention was given to narrow-wall-inserted transitions. These can be classified into two substrate types based on their design: single-layer and multi-layer. For single-layer substrates, a V-shaped patch was proposed [1] with an operating frequency of 76.5 GHz and a bandwidth of 4.1%. Other techniques, such as overlapped patches [15], a feed technique developed at the non-radiating edge of the coplanar patch [16], and a short-end parasitic patch [17], have also been proposed. However, these techniques often suffer from narrow bandwidths and operate at lower frequencies. In contrast, for multi-layer substrates, an X-shaped patch has been proposed [18], exhibiting a bandwidth of 20.6% and a transmission coefficient of –2.6 dB at 275 GHz. Notably, the proposed transition achieved a commendable frequency bandwidth of 71.50 GHz (26.1%) at the reflection coefficient below –10 dB, showcasing superior performance compared to other designs. Additionally, the measured transmission coefficient of a single transition at 275 GHz was –2.5 dB, further highlighting its effectiveness.

Table 4.2 Comparison of the planar-line-to-waveguide transition

Ref.	f_C (GHz)	BW_{rel} [%]	S_{21} (dB)	Structure
[1]	76.5	4.1%@ −15dB	− 0.6	Single
[15]	26.5	21.2%@ −10dB	− 0.6	Back-to-Back
[16]	77.0	15.0%@ −10dB	− 0.6	Single
[17]	96.0	15.1%@ −10dB	− 0.5	Single
[18]	275	20.6%@ −10dB	− 2.6	Single
This work	275	26.1%@ −10dB	− 2.5	Single

4.4 Summary

The broadband multi-layer narrow-wall-inserted planar-line-to-waveguide transition was designed using modified V-shaped and double-stacked rectangular patches. Excitation of the modified V-shaped patch was achieved through a tapered GCPW feed line inserted from the narrow wall of the waveguide. This design transforms the mode from a single-end line to a waveguide by fostering strong coupling between the signal line and the radiating patch. The proposed transition is designed to be broadband due to the multiple resonances of the modified V-shaped patch, the double-stacked rectangular patch, and the cavity in the multi-layer substrates. The simulation indicates the bandwidth of the reflections below –10 dB is 63.25 GHz (22.7%). However, the measured bandwidth of the reflections below –10 dB is 71.50 GHz (26.1%). In addition, the measured insertion loss remains at 2.5 dB at the design frequency of 275 GHz. Furthermore, the measured result shows a bandwidth of transmission coefficient higher than −3 dB, measuring 48.60 GHz. These measured performances confirm the multi-layer single-ended-line-to-waveguide transition was feasible and suitable for practical sub-terahertz systems.

References

[1] K. Seo, K. Sakakibara, and N. Kikuma, "Narrow-Wall-Connected Microstrip-to-Waveguide Transition Using V-Shaped Patch Element in Millimeter-Wave Band," *IEICE Trans. Commun*., vol. 93-B, no. 10, 2010, pp. 2523-2530, doi: 10.1587/transcom.E93.B.2523.

[2] C. Chokchai, Y. Sugimoto, K. Sakakibara, M. Yamazaki, H. A. Diawuo and N. Kikuma, "Broadband GCPW-to-Waveguide Transition in Multi-layer Dielectric Substrates with Modified V-shaped and Double Patch in 270 GHz Band," *in IEEE Journal of microwave*.

[3] H. Iizuka, T. Watanabe, K. Sato, and K. Nishikawa, "Millimeter-wave Microstrip Line to Waveguide Transition Fabricated on a Single Layer Dielectric Substrate," *IEICE Trans. Commu.*, vol. E85-B, no.6, 2002, pp.1169-1177.

[4] K. Seo, K. Sakakibara, and N. Kikuma, "Microstrip-to-waveguide transition using waveguide with large broad-wall in millimeter-wave band," *2010 IEEE Int. Conf. Ultra-Wideband*, Nanjing, China, 2010, pp. 1-4, doi: 10.1109/ICUWB.2010.5614169.

[5] N. Thanh Tuan, K. Sakakibara, and N. Kikuma, "Bandwidth Extension of Planar Microstrip-to-Waveguide Transition by Controlling Transmission Modes Through Via-Hole Positioning in Millimeter-Wave Band," *IEEE Access*, vol. 7, pp. 161385-161393, 2019, doi: 10.1109/ACCESS.2019.2952073.

[6] S. Hara, R. Dong, S. Lee, K. Takano, N. Toshida, A. Kasamatsu, K. Sakakibara, T. Yoshida, S. Amakawa, and M. Fujishima, "A 76-Gbit/s 265-GHz CMOS Receiver With WR-3.4 Waveguide Interface," *IEEE J. of Solid-State Circuits*, vol. 57, no. 10, pp. 2988-2998, Oct. 2022, doi: 10.1109/JSSC.2022.3179560.

[7] K. Feng, T. Spencer, and J. Watkowski, "Integrated metallization system for high density interconnects and modified semi additive processing," *2013 8th Int. Microsystems Packag. Assem. Circuits Techn. Conf. (IMPACT)*, Taipei, Taiwan, 2013, pp. 241-244, doi: 10.1109/IMPACT.2013.6706700.

[8] MITSUBISHI GAS CHEMICAL, “Non-haloganated Low CTE BT Resin Laminate for IC Plastic Packages”, https://www.mgc.co.jp/eng/prod-ucts/sc/btprint/lineup/hfbt.html, (2022-07-18).

[9] HFSS. 2021 R1, Ansoft Corporation, Pittsburgh, PA, 2021.

[10] Anritsu Company. Calibration and Measurement Guide VectorStarTM MS464xB Series Microwave Vector Network Analyzer. Accessed: Nov. 18, 2022, Chap. 14. [Online.] Available: https://dl.cdn-anritsu.com/en-us/test-measurement/files/Manuals/Measurement-Guide/10410-00318AE.pdf.

[11] Y. Morishita K. Takahashi, R. Hasaba, T. Murata, K. Takinami, H. Kitamura, U. Sangawa, T. Tomura, and I. Watanabe, “Comparison between Microstrip-line and Substrate Integrated Waveguide on Package Substrate in 170 GHz and 300 GHz Bands,” *2022 Asia-Pacific Microw. Conf. (APMC)*, Yokohama, Japan, 2022, pp. 196-198, doi: 10.23919/APMC55665.2022.9999775.

[12] J. Eric Bracken, ANSYS, Inc., “A Causal Huray Model for Surface Roughness”, *DesignCon 2012*, Jan. 2012.

[13] P. G. Huray, “Surface Roughness,” in *The Foundations of Signal Integrity*, Hoboken, NJ, USA: John Wiley & Sons, Inc., 2010, ch. 6, pp. 217-275.

[14] L. Simonovich, “Practical method for modeling conductor roughness using cubic close-packing of equal spheres,” *2016 IEEE Int. Symp. Electromagn. Compat. (EMC)*, Ottawa, ON, Canada, 2016, pp. 917-920, doi: 10.1109/ISEMC.2016.7571773.

[15] Z. Tong and A. Stelzer, “A Vertical Transition Between Rectangular Waveguide and Coupled Microstrip Lines,” *IEEE Microw. Wireless Compon. Lett*., vol. 22, no. 5, pp. 251-253, May 2012, doi: 10.1109/LMWC.2012.2192719.

[16] E. Topak, J. Hasch, and T. Zwick, “Compact Topside Millimeter-Wave Waveguide-to-Microstrip Transitions,” *IEEE Microw. Wireless Compon. Lett.*, vol. 23, no. 12, pp. 641-643, Dec. 2013, doi: 10.1109/LMWC.2013.2284824.

[17] I. Zhou, and J. R. Robert, “Ultra-Wideband Narrow Wall Waveguide-to-Microstrip Transition Using Overlapped Patches,” *J. Sensors*, vol. 22, no. 8, 2022, doi: 10.3390/s22082964.

[18] M. Yamazaki, Y. Sugimoto, K. Sakakibara, and N. Kikuma, “Broadband differential-line-to-waveguide transition in multi-layer dielectric substrates with an X-shaped patch element in 280 GHz band,” *IEEE Trans. Microw. Theory Techn*., Jan. 2023. doi: 10.1109/TMTT.2022.3232501.

Chapter 5

SIW-to-SIW Transition in Multi-layer Substrates

This chapter presents a broadband transition between two SIW formed in different layers of a multi-layer substrate at the 270 GHz band. The transition design was constrained by the fabrication limitations of the metal pattern and via-hole arrangement in the sub-terahertz frequency band. The broadband operation achieved by combining techniques was coupled patch, aperture coupling, and a back-short structure. The proposed transition's principle was investigated through parameter studies conducted via electromagnetic simulations using the finite element method. Performance evaluations of the transition were conducted through both simulations and measurements, with waveguide measurements employed for evaluation. A WG-to-SIW-to-SIW transition with a back-to-back structure was designed, fabricated, and measured. Especially, the design effectively achieves the fabrication constraints in the sub-terahertz band.

5.1 SIW-to-SIW Transition

This section details the configuration and parameter study of the proposed SIW-to-SIW transition. The design concept of the transition aims to facilitate connections between the SIW-fed Rotman lens and the SIW slot antenna in a multi-layer substrate. Here, a parameter simulation was conducted to investigate the crucial aspects of the transition's wideband design. Additionally, the transition geometries were optimized using the electromagnetic field simulator ANSYS HFSS.

5.1.1 Configuration of SIW-to-SIW Transition

The proposed SIW-to-SIW transition in a multilayer substrate consists of two SIW formed in different layers. The multi-layer substrates comprise eight copper plates separated by seven dielectric plates, with three prepreg layers on each side of the core layer. The width of both SIW (W_S) is set to 570 μm to facilitate connection to an SIW-fed Rotman lens [1]. Where the width is determined by the center-to-center distance of the via-holes. The narrow-wall width of SIW 1 (W_{N1}) is 235 μm, and SIW 2 (W_{N2}) is 120 μm, as illustrated in Fig. 5.1. The thickness

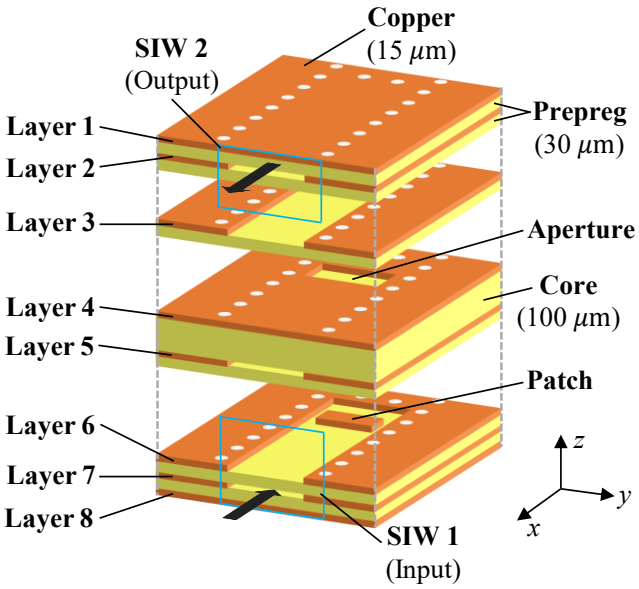

Figure 5.1 The geometry of the SIW-to-SIW transition.

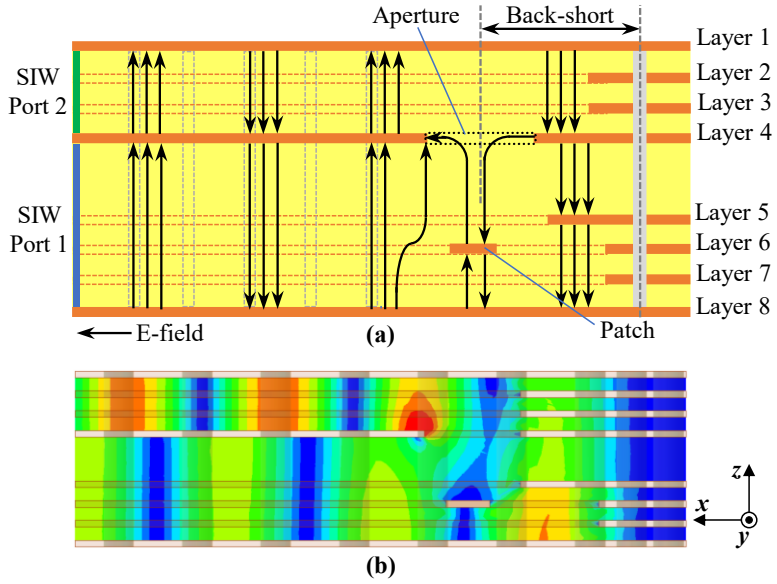

Figure 5.2 Cross-sectional view (a) mode transformation of the transition (b) simulated electric field distribution of the transition on the *xz*-plane at 270 GHz.

of the copper layer is 15 μm, with a conductivity of 5.7×10^7 S/m. The core layer has a thickness of 100 μm, and the prepreg layers are each 30 μm thick. The dielectric material is HL972LF-LD (Mitsubishi Gas Chemical Company, Inc.) [2], with a relative permittivity of 3.5 and a loss tangent (tan δ) of 0.003. From the measurement of the substrate using a Fabry-Perot resonator at 220–330 GHz, the relative permittivity is 3.6. The loss tangent is 0.009 at 220 GHz and 0.011 at 320 GHz, increasing linearly at frequencies in between.

An SIW 1 is formed at the bottom of the multi-layer substrate between Layer 4 and Layer 8, while an SIW 2 is formed at the top of the multi-layer substrate between Layer 1 and Layer 4. Rectangular aperture coupling is mounted on Layer 4, and the rectangular patch is positioned on the top metal plane of the SIW on Layer 6. The back-short structure is positioned at a distance from the back-short via-holes to the center of the rectangular aperture, approximately half the guide wavelength. In Fig. 5.2 (a), a cross-sectional view through the center of the SIW's wide wall in the proposed transition is depicted. The electromagnetic waves supplied from SIW 1 pass through the apertures in Layer 4 to the cavity by rectangular patch coupling, and then they are reflected by the back-short structure. The reflected and incident waves from SIW 1 are synthesized in phase, and the electromagnetic waves are output to SIW 2. Simulated electric field distribution in the cross-section at 270 GHz is shown in Fig. 5.2 (b), verifying the principle of the transition.

The metal patterns of each layer with their respective parameters are depicted in Fig. 5.3. The transition exhibits symmetry in plane AA', which passes through the center of the wide wall of the SIW. The via-holes have a diameter (ϕ) of 70 μm and a space between vias (d) of 180 μm, with a clearance (d_C) of 40 μm between the conductor pattern and the via-holes. To minimize electromagnetic wave leakage, the via-holes surrounding the cavity should be positioned as closely as possible. Plane BB' is defined through the center of the narrow wall of the rectangular aperture on Layer 4. Among the via holes surrounding the cavity, the position of the back-short via-holes (d_1), located on the negative side of the x-axis, is 345 μm. This parameter plays a crucial role in controlling the resonant frequency due to the back-short structure. Moreover, the dimensions of the aperture on Layer 4 significantly influence frequency and impedance matching. The aperture width (W_{S4}) is set to 420 μm, while the aperture length (L_{S4}) is designed to be approximately one-quarter of the guide wavelength (λg/4) at the center frequency of 270 GHz.

The stub length of SIW 2 ($D_{L2,3}$) is determined by the distance between the back-short via-holes and the opening edges on Layer 2 and Layer 3, with $D_{L2,3}$ adjusted to improve impedance matching. Similarly, the stub length of SIW 1 ($D_{L6,7}$) is set to 75 μm, determined by the distance between the back-short via-holes and the opening edges on Layer 6 and Layer 7. Additionally, the stub length of SIW 1 at Layer 5 (D_{L5}) is adjusted to regulate the frequency and enhance the bandwidth. A rectangular patch is positioned at Layer 6 to enhance coupling from SIW 1 to SIW 2. The position of the rectangular patch (D_P), set to 375 μm, determines the distance

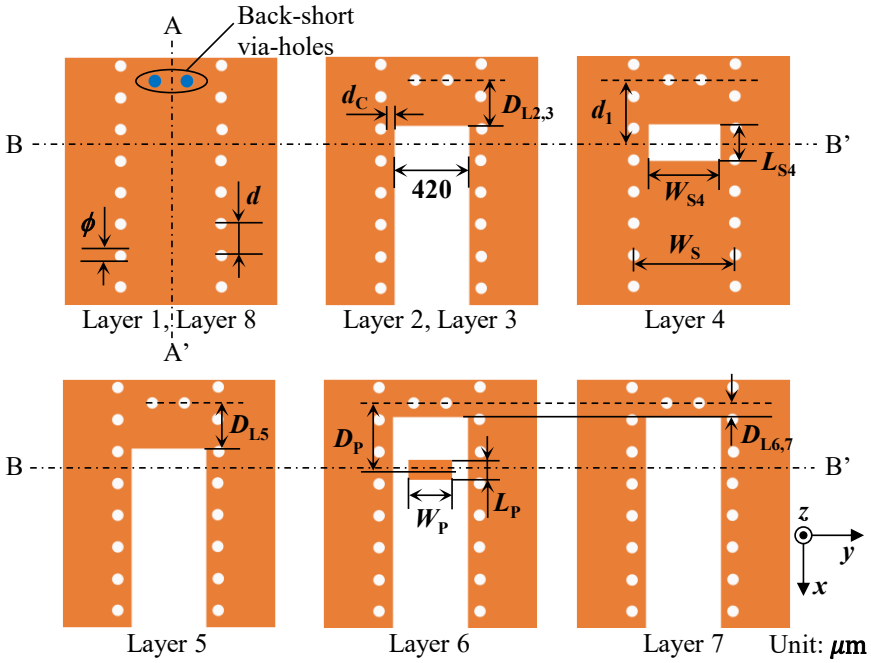

Figure 5.3 Top views of each layer with the parameters for the SIW-to-SIW transition.

between the back-short via-holes and the center of the rectangular patch. Moreover, the width of the rectangular patch (W_P), set to 240 μm, influences impedance matching, while the length of the rectangular patch (L_P) affects the frequency. The default length is one-quarter of the guide wavelength at 270 GHz. This design optimizes the structural parameters to maximize the frequency bandwidth, ensuring that the reflection coefficient remains below −10 dB.

5.1.2 Study Parameters of SIW-to-SIW Transition

This subsection scrutinizes the reflection characteristics of the SIW-to-SIW transition based on simulated parameters. The aim was to broaden the resonance bandwidth to achieve less than −10 dB for a center frequency of 270 GHz. Subsection A delves into the foundational principles of this transition. Within this context, a parameter simulation was conducted to investigate the pivotal elements of the wideband design of the transition.

The critical parameters of the SIW-to-SIW transition were analyzed to achieve wideband operation. An important parameter for controlling the resonant frequencies is the length of the rectangular patch (L_P) and the stub length of SIW 1 at Layer 5 (D_{L5}). These parameters govern the resonant frequency, thereby influencing the enhanced bandwidth. This is because

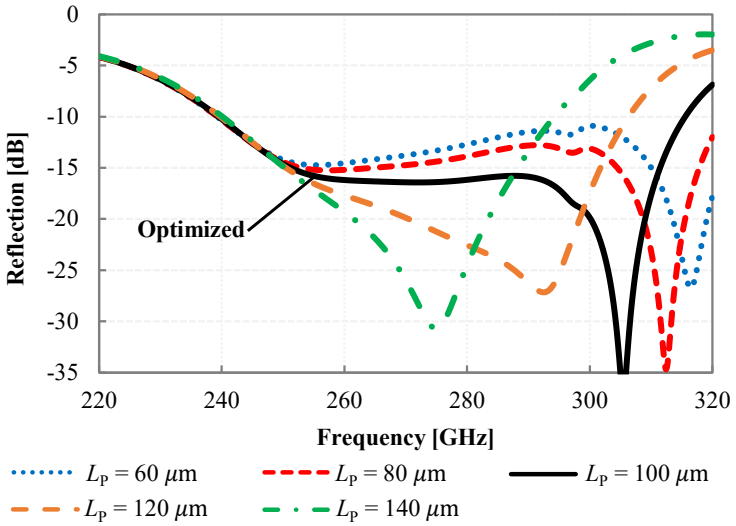

Figure 5.4 Reflection characteristics of the SIW-to-SIW transition depending on L_P.

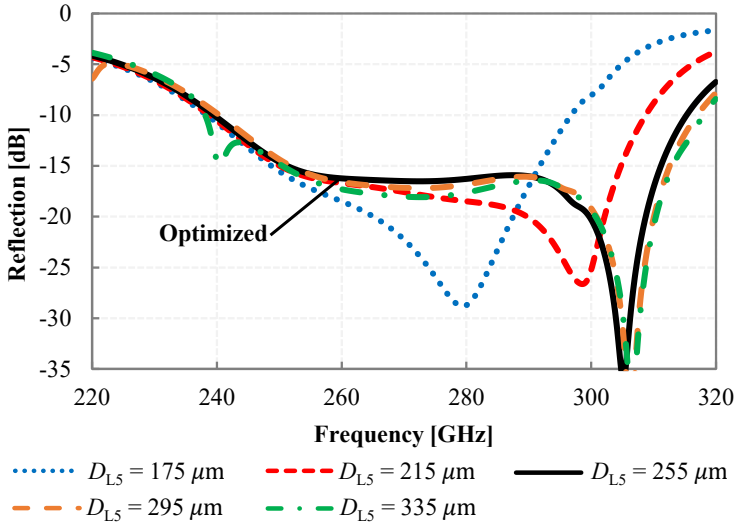

Figure 5.5 Reflection characteristics of the SIW-to-SIW transition depending on D_{L5}.

L_P and D_{L5} affect the position and distance of electromagnetic field coupling from SIW 1 through the aperture on Layer 4 to SIW 2. Fig. 5.4 illustrates the simulation of the reflection coefficient depending on L_P. It is evident that as L_P increases, the resonance frequency shifts to lower frequencies, resulting in a narrower bandwidth due to the increase in reflection coefficient levels at higher frequencies. Therefore, to achieve a wide bandwidth, the optimal value for L_P was determined to be 100 μm.

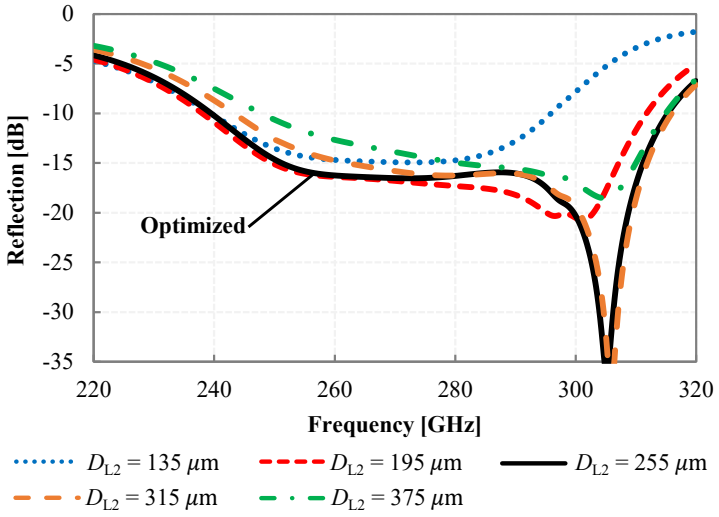

Figure 5.6 Reflection characteristics of the SIW-to-SIW transition depending on D_{L2}.

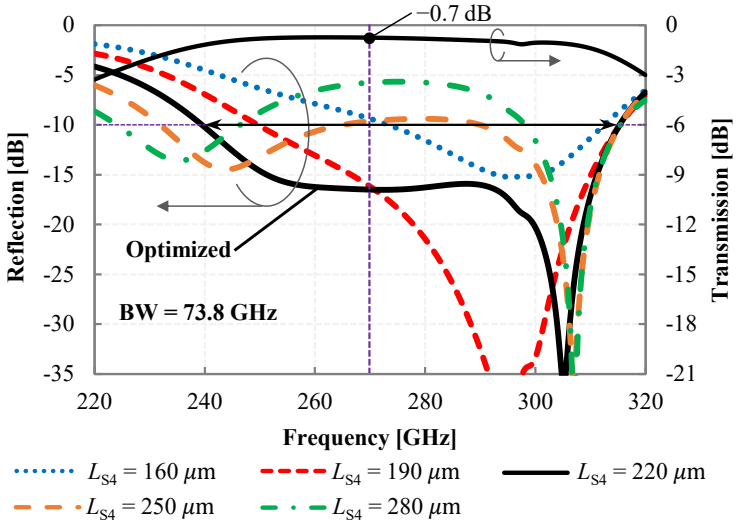

Figure 5.7 Reflection characteristics of the SIW-to-SIW transition depending on L_{S4}.

Furthermore, D_{L5} significantly influences the coupling between the rectangular patch on Layer 6 and the aperture on Layer 5. Fig. 5.5 illustrates the reflection characteristics of the transition depending on D_{L5}. As D_{L5} decreases, the resonance frequency shifts to lower frequencies, resulting in a narrower bandwidth. Conversely, increasing D_{L5} shifts the resonance frequency to higher frequencies and widens the bandwidth. Meanwhile, at low frequencies, there may be a decrease in reflection and transmission coefficients due to the patch length becoming large, leading to an overlap between D_{L5} and L_P. Therefore, to achieve a wide bandwidth, the appropriate value for D_{L5} was determined to be 255 μm.

The length of the back-short structure plays a crucial role in frequency and impedance matching. In this study, the adjustment of the stub length of SIW 2 ($D_{L2,3}$) was utilized to enhance

Table 5.1 Optimized parameters of the SIW-to-SIW transition

Description	Name	Value
Diameter of via	ϕ	70 μm
Space between vias	d	180 μm
Clearance between via-holes and edge of aperture	d_C	40 μm
Back-short distance	d_1	345 μm
Width of SIW	W_S	570 μm
Narrow-wall width of SIW 1	W_{N1}	235 μm
Narrow-wall width of SIW 2	W_{N2}	120 μm
Aperture length	L_{S4}	220 μm
Aperture width	W_{S4}	420 μm
Stub length of SIW 2 on Layer 2 and Layer 3	$D_{L2,3}$	255 μm
Stub length of SIW 1 on Layer 5	D_{L5}	255 μm
Stub length of SIW 2 on Layer 6 and Layer 7	$D_{L6.7}$	75 μm
Position of the rectangular patch	D_P	375 μm
Width of rectangular patch	W_P	240 μm
Length of rectangular patch	L_P	100 μm
Thickness of the copper layer	t	15 μm
Thickness of the core layer	t_c	100 μm
Thickness of the prepreg layer	t_P	30 μm

the bandwidth. Fig. 5.6 illustrates the simulation results of the reflection coefficient as a function of $D_{L2,3}$. Decreasing $D_{L2,3}$ leads to an increase in the reflection coefficient level at higher resonant frequencies, whereas increasing $D_{L2,3}$ results in an increase in the reflection coefficient level at lower resonant frequencies. Thus, to achieve a wide bandwidth, the optimal value for $D_{L2,3}$ was determined to be 255 μm. Moreover, the aperture length (L_{S4}) on Layer 4 emerges as a significant parameter influencing bandwidth due to its impact on electromagnetic field coupling. Fig. 5.7 demonstrates the simulation results of the reflection coefficient with varying L_{S4}. Decreasing L_{S4} leads to an increase in the reflection coefficient level at lower resonant frequencies, whereas increasing L_{S4} results in an increase in the reflection coefficient level at the resonant frequency. The suitable value for L_{S4} was found to be 220 μm.

The study of various parameters yields the following conclusions: Resonance frequency can be effectively controlled by adjusting the values of L_P and D_{L5}. Impedance matching can be achieved by varying $D_{L2,3}$ and L_{S4}. The optimal design parameters obtained through electromagnetic simulation are summarized in Table 5.1, while the transmission and reflection characteristics of these parameters are depicted in Fig. 5.7. The bandwidth of reflections less than −10 dB was 73.8 GHz (ranging from 240.4 GHz to 314.2 GHz). At the center frequency of 270 GHz, the transmission loss was observed to be 0.7 dB.

Table 5.2 provides a summary of the performance comparison between the proposed SIW-to-SIW transition and previously reported transitions. It is noteworthy that the design frequencies and methodologies employed in each study varied, rendering direct comparison challenging. However, many of these techniques exhibit limitations such as narrow bandwidths and operation at lower frequencies. In contrast, the proposed transition is designed for a higher frequency range compared to others. This paper achieved a broadband and low-loss transition with a fractional bandwidth of 26.6%, demonstrating superior performance relative to previous designs. Furthermore, the transmission coefficient of the transition at 270 GHz was –0.7 dB, further underscoring its effectiveness.

Table 5.2 Comparison of the SIW-to-SIW transition

Ref.	f_C (GHz)	BW_{rel} [%] @ −10dB	S_{21} (dB)
[3]	94.0	8.5%	− 0.2
[4]	16	45.1%	− 1.0
[5]	9.7	10.3%	− 3.0
[6]	10.0	3.0%	N/A
[7]	133	37.2%	− 0.28
This work	270	26.6%	− 0.7

5.2 Structure Design for Waveguide Measurement

This section delineates the design of the transition structure for fabrication purposes. For waveguide measurement, it is essential to devise a transition capable of connecting to the waveguide flange. Hence, this section will encompass the following subsections: the design of the WG-to-SIW transition, the WG-to-SIW-to-SIW transition, which integrates the WG-to-SIW transition with the SIW-to-SIW transition, and the configuration of the back-to-back transition.

5.2.1 WG-to-SIW Transition

The WG is WR-3.4 (0.864 × 0.432 mm). The SIW width (W_S) is 570 μm, where the width is defined by the center-to-center spacing of the via hole. The narrow-wall width of the SIW (W_N) is 120 μm. The thickness t of the copper layer is 15 μm. The dielectric and copper layers are stacked alternately, resulting in a total of eight copper layers, as depicted in Fig. 5.8 (a). The dielectric material used is HL972LF-LD. Additionally, three prepreg layers, each 30 μm thick, are incorporated on both sides of the central core layer, which has a thickness of 100 μm.

An SIW is formed at the top of the multi-layer substrate between Layer 1 and Layer 4. The waveguide is connected to the transition on the top plane of Layer 1. A rectangular aperture is opened on the top metal plane of the SIW on Layer 1, with the aperture length (L_{S1}) and aperture width (W_{S1}). The rectangular patch is mounted at this rectangular aperture, with patch length (L_P) and patch width (W_P). To prevent parallel-plate mode leakage across metal planes, the via-holes were strategically arranged around the waveguide. The matching via-holes are connected from Layer 1 to Layer 4 between the aperture and SIW.

The metal pattern of each layer with parameters is illustrated in Fig. 5.8 (b). The transition design is crafted within the fabrication constraints of the terahertz frequency band. Here, the diameter of the via-holes (ϕ) is 70 μm, and the pitch between via-holes (d) is 180 μm. Additionally, a clearance (d_C) of 40 μm is maintained between the conductor pattern and the via-holes. For the matching via-holes, the parameter determining the y-axis size of the distance is denoted as d_m, representing the center-to-center spacing of the via-holes. Due to manufacturing limitations, the via-holes cannot be opened at the edge of the metal pattern. Therefore, at Layer 2 and Layer 3 of the SIW, the edges of the metal patterns protrude (via pad) from the matching via-holes into the SIW region. All via-holes penetrate only from Layer 1 to Layer 4. From Layer 5 to Layer 8, the copper layers without pattern are stacked alternately with the dielectric.

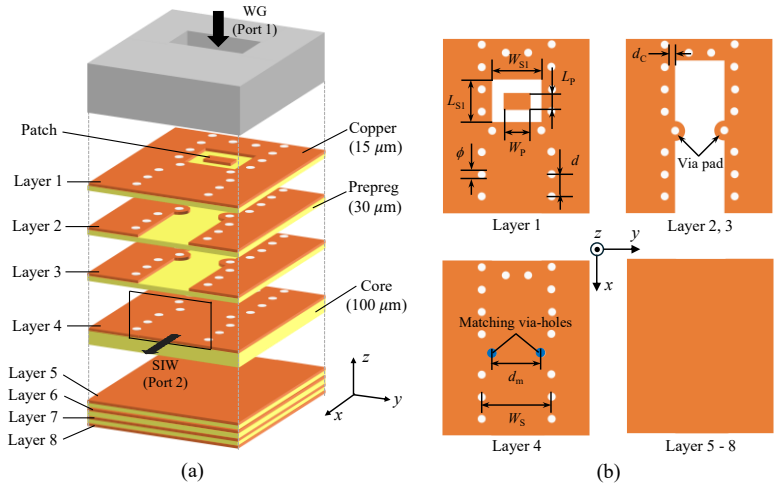

Figure 5.8 Configuration of the WG-to-SIW transition (a) 3D overview and (b) Top views of each layer with the parameters.

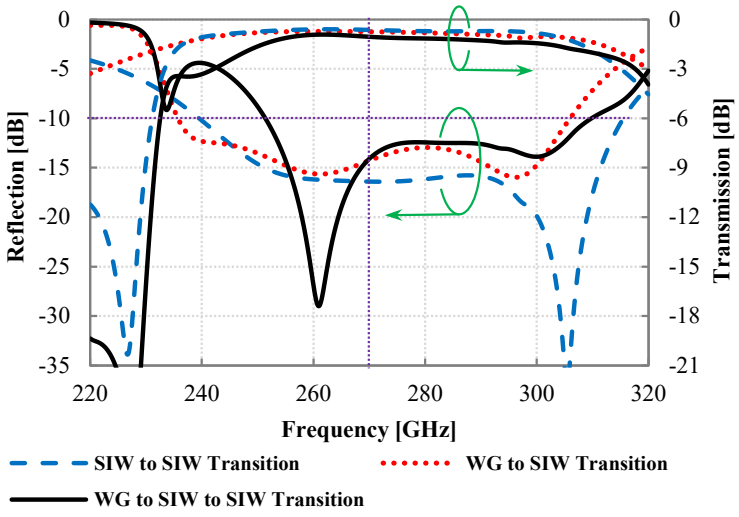

Figure 5.9 Comparison simulation results of each transition.

In this design, the structural parameters mentioned above were optimized to maximize the frequency bandwidth where the reflection coefficient is less than −10 dB. The optimized design parameters obtained through electromagnetic field analysis are summarized in Table 5.3. The simulation results of the WG-to-SIW transition using these optimized parameters are depicted by the red dotted line in Fig. 5.9. The frequency bandwidth for the reflection coefficient less than −10 dB spans from 235.7 GHz to 305.7 GHz, resulting in a bandwidth of 70.0 GHz (25.8%). Also, at the center frequency of 270 GHz, the transmission coefficient was −0.6 dB.

Table 5.3 Optimized parameters of the WG-to-SIW transition

Description	Name	Value
Diameter of via-hole	ϕ	70 μm
Space between via-holes	d	180 μm
Clearance between via-holes and edge of aperture	d_C	40 μm
Width of SIW	W_S	570 μm
Narrow-wall width of SIW	W_N	120 μm
Length of the aperture on Layer 1	L_{S1}	370 μm
Width of the aperture on Layer 1	W_{S1}	420 μm
Distance between matching via-holes	d_m	400 μm
Width of rectangular patch	W_P	200 μm
Length of rectangular patch	L_P	170 μm
Broad wall of waveguide	a	864 μm
Narrow wall of waveguide	b	432 μm

5.2.2 WG-to-SIW-to-SIW Transition

This transition is achieved through a combination of the SIW-to-SIW transition (refer to subsection 5.1.1) and the WG-to-SIW transition (refer to subsection 5.2.1). The 3D configuration of the WG-to-SIW-to-SIW transition in multi-layer substrates is depicted in Fig. 5.10 (a), while the electromagnetic flow of the transition in the cross-section view is illustrated in Fig. 5.10 (b). Initially, a magnetic current is excited from the waveguide and then coupled by Patch 1 to the SIW between Layer 1 and Layer 4. Subsequently, a magnetic field is coupled through the aperture on Layer 4. Finally, Patch 2 couples a magnetic field to the SIW between Layer 4 and Layer 8.

In this design, the optimized parameters of the SIW-to-SIW transition and WG-to-SIW transition are utilized. The metal pattern of each layer is illustrated in Fig. 5.10 (c). The distance between the two transitions was set at 0.9 mm, determined from the center-to-center distance of the two apertures of the transitions. The simulation results of the WG-to-SIW-to-SIW transition using these optimized parameters are depicted by the solid black line in Fig. 5.9. The frequency bandwidth for the reflection coefficient less than −10 dB spans from 251.5 GHz to 309.5 GHz, resulting in a bandwidth of 58.0 GHz (20.6%). Additionally, at the center frequency of 270 GHz, the transmission coefficient was −1.0 dB.

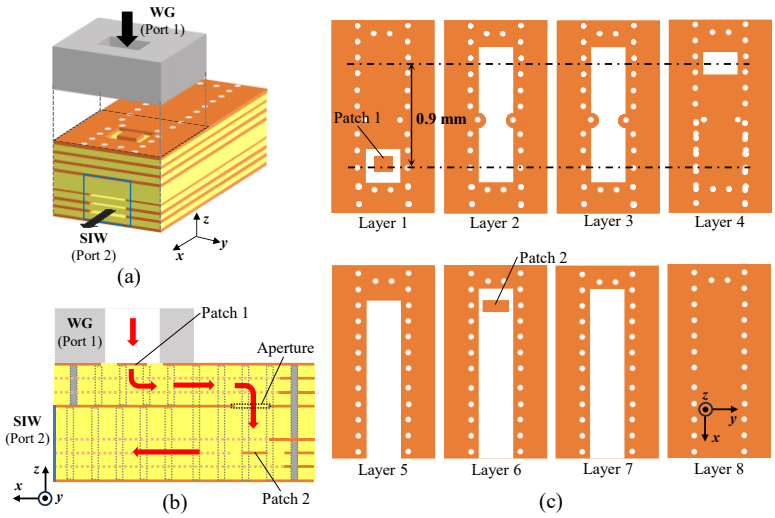

Figure 5.10 Configuration of the WG-to-SIW-to-SIW transition (a) 3D overview, (b) Cross-sectional view and (c) Top views of each layer with the parameters.

5.2.3 Back-to-Back Transition

For the waveguide measurements, a back-to-back configuration was established on the substrate. Consequently, two identical WG-to-SIW-to-SIW transitions with the same geometric parameters were connected to the fabricated substrate via an SIW (device under test: DUT). The configuration of the back-to-back transition in the cross-sectional view is shown in Fig. 5.11. The DUT is configured with four spacing lengths denoted by the variable *X*, measured from the center-to-center of the two waveguides. Specifically, *X* is set to 4 mm, 6 mm, 8 mm, and 20 mm. Similarly, the length of SIW (denoted by *x*) also varies, with *x* set to 3 mm, 5 mm, 7 mm, and 19 mm.

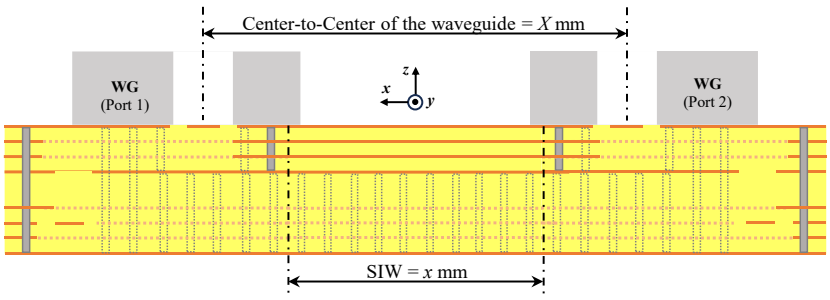

Figure 5.11 Configuration of the back-to-back transition in cross-sectional view.

5.3 Fabrication and Experimental Performances

This section presents the verification of the simulation validity of the proposed transition. Transmission loss and reflection characteristics of the fabricated transitions were measured to assess their performance. The waveguide measurement technique was employed for SIW losses, characterization, and the efficiency of the proposed transitions. Measurements were conducted using a back-to-back transition with four different lengths of SIW.

5.3.1 Fabrication

The DUT is fabricated using a high-pressure heating process, employing the modified semi-additive process (MSAP) to produce micropatterns with fine pitch [8]. Initially, a 4 μm nickel layer is applied onto the copper plate interface, followed by a plating process resulting in a 0.05 μm gold layer. MSAP ensures rounded corners at the edges of the metal patterns, with a corner radius of 10 μm. The accuracy of the metal patterns on the same layer is maintained at 10 μm, whereas on different layers, it is 25 μm. The thickness variation of the copper plate is within ±7 μm, while via-hole positions may vary by up to ±25 μm, and their diameters by up to ±20 μm. The core layer's thickness variation is less than ±15 μm, and the variations of the prepreg layers are less than ±10 μm. The DUTs were fabricated by CONNECTEC JAPAN Corporation, with fabrication accuracy detailed in Table 5.4. Configurations of the DUTs connected by SIWs of varying lengths were fabricated as depicted in Fig. 5.12. SIW lengths were chosen as 3, 5, 7, and 19 mm to evaluate SIW loss accurately.

Table 5.4 Fabrication accuracies of the multi-layer substrate

	Accuracy
Thickness of the core	±15 μm
Thickness of the prepreg	±10 μm
Thickness of the copper	±7 μm
Via diameter	±20 μm
Via position	±25 μm
Pattern width of the signal lines	±10 μm
Gap	±10 μm

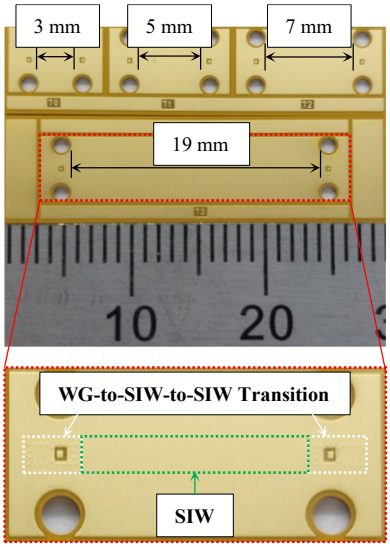

Figure 5.12 Fabricated DUTs for different lengths of the SIW and an enlarged view.

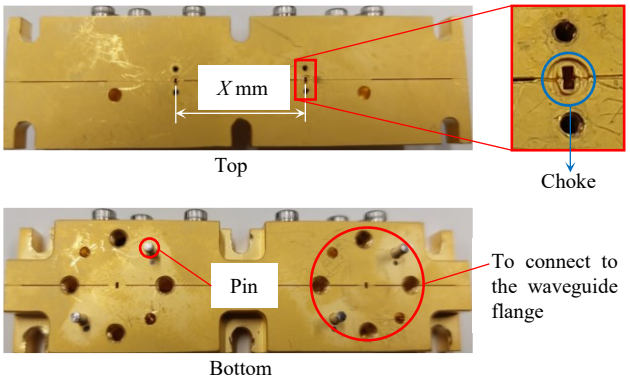

Figure 5.13 Fabricated jig and an enlarged view of the jig.

In addition, waveguide measurements necessitate a metal jig to facilitate the connection between the DUT and the waveguide. Hence, jigs were designed and fabricated in four lengths: 4 mm, 6 mm, 8 mm, and 20 mm, corresponding to the DUT lengths. A choke structure is incorporated around the waveguide on the jig's surface to minimize leakage from the gap between the DUT and the jig. Constructed of copper and coated with gold, the fabricated metal jig with the choke structure is depicted in Fig. 5.13.

5.3.2 Measurement

The measurement system setup is illustrated in Fig. 5.14, where measurements are conducted to verify the reliability of the employed technique and the characteristics of the proposed transition. The DUT for these measurements is positioned on a jig connected to the waveguide. Mounted on a metal jig, the DUT features waveguides at both terminals linked to the flange of the standard waveguide (WR-3). To ensure high precision, the DUT is securely fixed in place using a small screw with a diameter of 1 mm. Measurement accuracy is confirmed through repeated assembly and measurement processes. An ANRITSU MS4647B vector network analyzer is connected to the VDI WR3.4-VNAX millimeter-wave extension module. The two ports of the standard waveguide extending from the millimeter-wave module undergo calibration using a WR-3 Anritsu waveguide calibrator model SM6567 at the plane connected to the waveguide in a metal jig. Reflection and transmission characteristics are measured, encompassing the waveguide in the jig and the SIW between the two transitions. A vector network analyzer equipped with a time-gate domain function is utilized to measure the scattering parameters, mitigating the impact of multiple reflections [9].

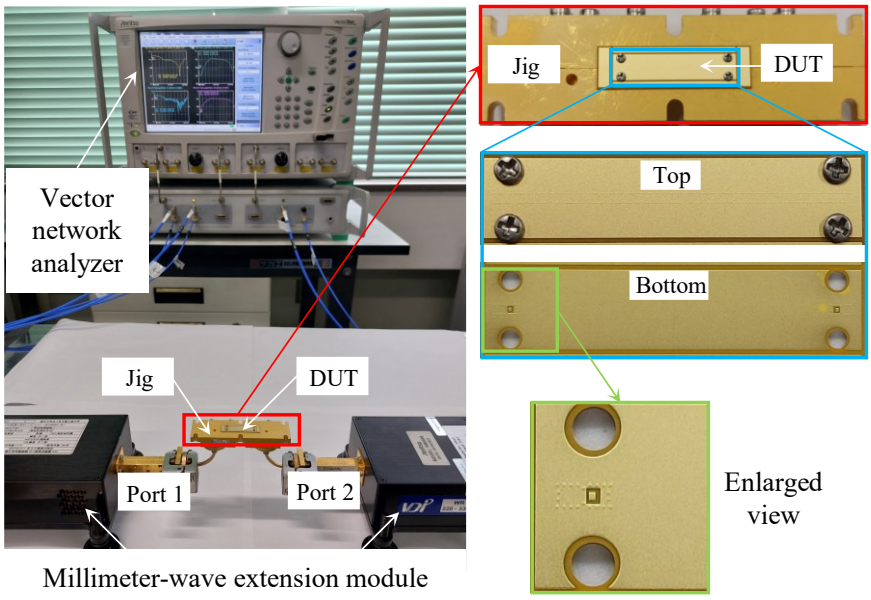

Figure 5.14 Experimental setup of the proposed transition with the waveguide jig in the WR-3 band (220–330 GHz).

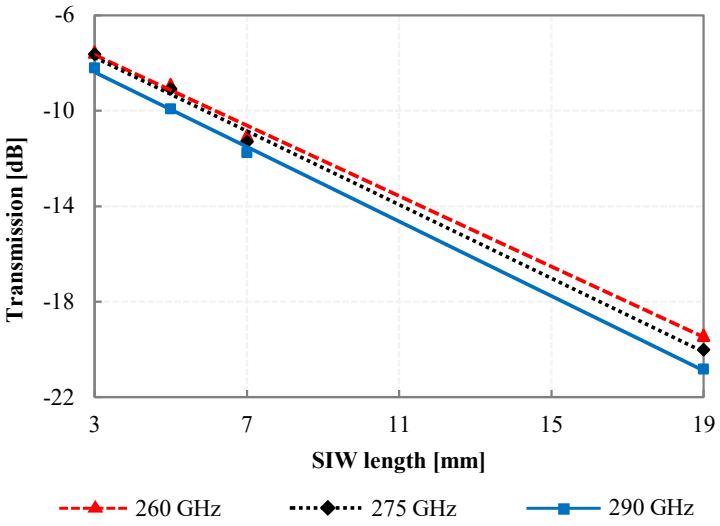

Figure 5.15 Measured transmission coefficients of the DUTs with four different SIW lengths.

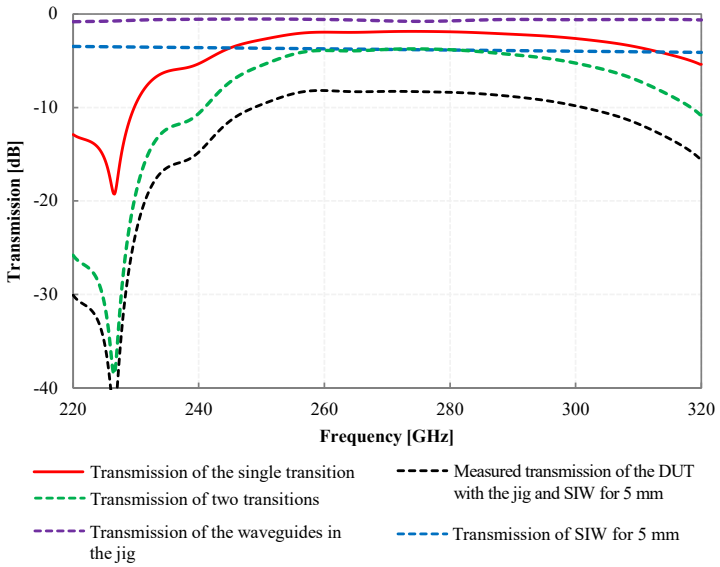

Figure 5.16 Loss and transmission characteristics at each correction process of the fabricated transition.

To accurately assess each transition's insertion loss, the SIW losses between the transitions and the waveguides within the jig were measured to determine the necessary compensation. The loss in the metal jig is determined by connecting two identical jigs face-to-face. The performance of these SIW was evaluated using a combination of analytical and experimental methods across the frequency range of 100 GHz to 300 GHz, as implemented in [10]. The SIW loss between the two transitions is derived from the difference in insertion loss observed in DUTs with four different SIW lengths (refer to Fig. 5.12). The SIW loss is approximated based on the measured transmission coefficient of DUTs of each length. The estimation process is

exemplified using frequencies of 260 GHz, 275 GHz, and 290 GHz. Fig. 5.15 displays the measured transmission coefficient of the DUTs with varying lengths and their respective approximated linear trends, adjusted for jig loss. At each frequency, the slope of the linear trend represents the estimated transmission loss per millimeter of the SIW. The estimated SIW losses at 260 GHz, 275 GHz, and 290 GHz were 0.59 dB/mm, 0.68 dB/mm, and 0.78 dB/mm, respectively.

Fig. 5.16 illustrates the individual losses of each component used to estimate the insertion loss of a single transition. The black dashed line represents the measured transmission of the device under test (DUT), including the SIW and waveguide in the jig from Port 1 to Port 2. The blue dashed line indicates the 5 mm SIW loss, estimated from the difference in measured SIWs for DUTs of four different lengths. Additionally, the transmission with waveguide losses in the jig, shown by the purple dashed line, was obtained through jig measurement. The waveguide loss in the jig was measured by connecting two identical jigs and the losses of the single waveguide in the jig was found to be 0.7 dB at 270 GHz. Finally, the transmission coefficient of the single transition was evaluated from the transmission of the entire structure with a 5 mm SIW by de-embedding the waveguide and SIW losses at each frequency point across the entire frequency band, represented by the red solid line.

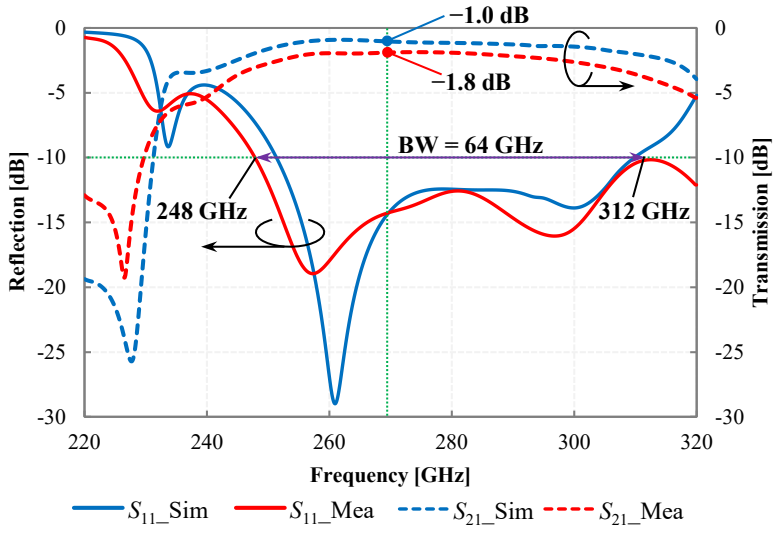

Figure 5.17 Measured and simulated reflection and transmission coefficients of the WG-to-SIW-to-SIW transition.

Fig. 5.17 shows the measurement and simulation of the scattering parameters of the WG-to-SIW-to-SIW transition. The simulation results indicate a reflection coefficient bandwidth below −10 dB of 58.0 GHz (20.6%), spanning from 251.5 GHz to 309.5 GHz, with a simulated transmission coefficient of −1.0 dB at the center frequency of 270 GHz. The measured results reveal a reflection coefficient bandwidth below −10 dB of 64.0 GHz (22.8%), spanning from 248.0 GHz to 312.0 GHz, represented by the red solid line. The measured transmission coefficient at the center frequency of 270 GHz was −1.8 dB. Notably, the measured lower resonant frequency is 3.5 GHz lower than the simulation.

It can be observed from the graph that the measured reflection coefficient results of the WG-to-SIW-to-SIW transitions are shifted to lower frequencies due to imperfections in the size and position of via holes, thickness variations, layer misalignments, and the dielectric constant of the substrate. Differences between the measured and simulated transmission coefficients are attributed to copper surface roughness and conductivity defects, which significantly affect conductor loss, including the tangent of the fabricated substrate. The copper skin effect depth and the surface roughness used in fabrication were 0.12 μm and 0.3 μm, respectively. Additionally, factors such as fabrication tolerances and mechanical assembly errors, which are critical in the THz bands, especially with multilayered structures, may contribute to the decrease in the transmission coefficient.

5.4 Summary

A broadband SIW-to-SIW transition in multi-layer substrates with a back-short structure and patch element for the 270 GHz band is proposed. The broadband operation combines techniques including coupled patch, aperture coupling, and a back-short structure. The transition principle was investigated through parameter studies conducted via electromagnetic simulations using the finite element method. The transition design has been successful within fabrication limitations in the terahertz band. Simulations of the multi-layer SIW-to-SIW transition showed a reflection coefficient bandwidth of less than −10 dB at 73.8 GHz, with a transmission loss of 0.7 dB at the center frequency of 270 GHz. A WG-to-SIW-to-SIW transition with a back-to-back configuration was designed, fabricated, and measured in the sub-terahertz band. The measured results transmission coefficient for a single multi-layer WG-to-SIW-to-SIW transition was −1.8 dB at 270 GHz. Furthermore, the measured result shows a bandwidth of transmission coefficient higher than −3 dB, measuring 57.4 GHz. The measured results revealed a reflection coefficient bandwidth below −10 dB of 64.0 GHz (22.8%), spanning from 248.0 GHz to 312.0 GHz. These performances confirmed the feasibility of the multi-layer WG-to-SIW-to-SIW transition, making it suitable for practical sub-terahertz systems.

References

[1] S. Kishi, T. Morioka, K. Sakakibara, J. Kim, Y. Sugimoto, and N. Kikuma, "274-GHz Substrate-Integrated-Waveguide Fed Rotman-Lens Multibeam Antenna Integrated in Multi-Layer Substrate," *2023 IEEE Int. Symp. Antennas Propag. (ISAP)*, Kuala Lumpur, Malaysia, 2023, pp. 1-2, doi: 10.1109/ISAP57493.2023.10388800.

[2] MITSUBISHI GAS CHEMICAL, "Non-haloganated Low CTE BT Resin Laminate for IC Plastic Packages", https://www.mgc.co.jp/eng/prod-ucts/sc/btprint/lineup/hfbt.html, (2022-07-18).

[3] D. Wang, Y. Fan, and Y. J. Cheng, "A W-Band, Low-Cost and High-Efficiency Antenna Array Using Multilayer SIW-to-SIW Transition With Leakage-Suppressing Scheme," *in IEEE Trans. Antennas Propag.*, vol. 71, no. 12, pp. 10014-10019, Dec. 2023, doi: 10.1109/TAP.2023.3320903.

[4] K. Song, Y. Fan, Guiqin Yue, and Bo Zhang, "Novel substrate integrated waveguide layer-to-layer transitions," *2008 Asia-Pacific Microw. Conf.*, Macau, 2008, pp. 1-4, doi: 10.1109/APMC.2008.4958215.

[5] M. N. Hafiz, M. Rafiee, and M. S. Aftanasar, "Design of a rectangular slot coupling for effective transition between two layers of SIW," *2015 IEEE Int. RF Microw. Conf. (RFM)*, Kuching, Malaysia, 2015, pp. 40-44, doi: 10.1109/RFM.2015.7587708.

[6] M. S. Aftanasar, and M. N. Hafiz, "Fabricated multilayer SIW system using PCB manufacturing process," *2016 IEEE Asia-Pacific Conf. Appl. Electromagn. (APACE)*, Langkawi, Malaysia, 2016, pp. 100-104, doi: 10.1109/APACE.2016.7915861.

[7] T. -Y. Lin, S. -G. Lin, Y. -C. Chang, C. Hsieh, and D. -C. Chang, "A Broadband Sub-THz Band Stacked Transition of SIW-to-SIW," *2023 IEEE 27th Workshop Signal Power Integrity (SPI)*, Aveiro, Portugal, 2023, pp. 1-2, doi: 10.1109/SPI57109.2023.10145570.

[8] K. Feng, T. Spencer, and J. Watkowski, “Integrated metallization system for high density interconnects and modified semi additive processing,” *2013 8th Int. Microsystems Packag. Assem. Circuits Techn. Conf. (IMPACT)*, Taipei, Taiwan, 2013, pp. 241-244, doi: 10.1109/IMPACT.2013.6706700.

[9] Anritsu Company. Calibration and Measurement Guide VectorStarTM MS464xB Series Microwave Vector Network Analyzer. Accessed: Apr. 04, 2024, Chap. 14. [Online.] Available: https://dl.cdn-anritsu.com/en-us/test-measurement/files/Manuals/Operation-Manual/10410-00317W.pdf.

[10] Y. Morishita K. Takahashi, R. Hasaba, T. Murata, K. Takinami, H. Kitamura, U. Sangawa, T. Tomura, and I. Watanabe, “Comparison between Microstrip-line and Substrate Integrated Waveguide on Package Substrate in 170 GHz and 300 GHz Bands,” *2022 Asia-Pacific Microw. Conf. (APMC)*, Yokohama, Japan, 2022, pp. 196-198, doi: 10.23919/APMC55665.2022.9999775.

Chapter 6

Conclusion and Contribution

This dissertation primarily presents a design technique for wideband and low-loss planar line-to-waveguide transitions in multi-layer substrates within the sub-terahertz band. The study offers a comprehensive solution for addressing the feeding circuit from the IC chip to the array antenna. Three main objectives were identified and developed, including broad-wall-inserted planar-line-to-waveguide transitions in multi-layer substrates comprising single-end line and differential-line-to-waveguide transitions, narrow-wall-inserted planar-line-to-waveguide transition in multi-layer substrates, and SIW-to-SIW transition in multi-layer substrates.

In Chapter 3, a broadband broad-wall-inserted planar-line-to-waveguide transition is designed for sub-terahertz frequencies within multi-layer substrates. This Chapter encompasses both single-end line-to-waveguide and differential-line-to-waveguide transition configurations. The single-end line-to-waveguide transition utilizes grounded suspended coplanar waveguide (GSCPW) and grounded coplanar waveguide (GCPW) configurations for feeding, while the differential-line-to-waveguide transition employs GCPW. The characteristics of these transitions are analyzed through electromagnetic simulations using the finite element method and validated through experimental measurements within the WR-3 band (220 GHz-320 GHz). To extend the bandwidth of the grounded suspended coplanar waveguide (GSCPW)-to-waveguide transition in a multi-layer dielectric substrate, corrugation structures are introduced in the sub-terahertz band. A rectangular patch element is utilized to transmit to the waveguide, while corrugation structures are applied at the edges of the aperture on the middle layer to enhance transmission characteristics and extend the bandwidth. The proposed multi-layer GSCPW-to-waveguide transition achieves bandwidths of S_{11} below −10 dB and S_{21} higher than -3 dB, measuring 58.9 GHz and 52.8 GHz, respectively. The inclusion of corrugation structures extends the bandwidth by up to 12.2% compared to transitions without corrugation. Additionally, a broadband grounded coplanar waveguide (GCPW)-to-waveguide transition, covering the 250-290 GHz band, is developed. This transition features a GCPW line inserted from the broad wall of the waveguide, exciting a double rectangular stacked patch located at the waveguide center. Corrugation structures are applied at the edges of the aperture on the middle layer. Broadband operation is achieved through the utilization of a double patch, corrugation structures, and a cavity formed by the via-hole arrangement surrounding apertures

patterned in a multi-layer substrate. The proposed transition demonstrates a bandwidth of S_{11} below −10 dB of 49.0 GHz. Moreover, a broadband waveguide-to-differential-line transition with a triple-stacked patch is proposed for use in the 300 GHz band. This transition involves differential signal lines inserted into the waveguide region from both broad walls, with a triple circular stacked patch element facilitating broadband transmission from the waveguide to the planar differential line formed in a multi-layer substrate. Additionally, an optimized arrangement of via-holes prevents electric field leakage effectively and enhances transmission characteristics in the high-frequency band. The measured result shows a bandwidth of S_{11} below −10 dB exceeding 100 GHz and bandwidths of S_{21} higher than −3 dB, measuring 63 GHz. Overall, the measured performances substantiate the feasibility of the multi-layer broad-wall-inserted planar-line-to-waveguide transition, affirming its suitability for practical sub-terahertz systems.

Chapter 4 introduced a broadband tapered GCPW-to-waveguide transition designed for the 270 GHz band within multi-layer substrates. The transition was meticulously crafted within the fabrication constraints of the metal pattern and via-hole arrangement specific to the sub-terahertz band. The broadband operation was achieved through a combination of stacked patches and multiple resonance techniques within the cavity. The utilization of modified V-shaped and double-stacked rectangular patches facilitated multiple resonances, while the strategic arrangement of apertures and via-holes contributed to cavity formation. Excitation of the modified V-shaped patch was realized through a tapered GCPW feed line inserted from the narrow wall of the waveguide. This design facilitated the transformation of the mode from a single-end line to a waveguide, fostering strong coupling between the signal line and the radiating patch. Simulation results indicate a bandwidth of reflections below –10 dB measuring 63.25 GHz (22.7%). Notably, the design effectively addressed fabrication limitations in the sub-terahertz frequency band. However, the measured bandwidth of reflections below –10 dB extended to 71.50 GHz (26.1%). Additionally, the measured insertion loss remained at 2.5 dB at the design frequency of 270 GHz. Furthermore, the measured result shows a bandwidth of transmission coefficient higher than −3 dB, measuring 48.60 GHz. These measured performances confirm the feasibility of the multi-layer single-ended-line-to-waveguide transition and its suitability for practical sub-terahertz systems.

In addition, Chapter 5 presents a broadband transition between two SIW formed in different layers of a multi-layer substrate at the 270 GHz band. The transition design was constrained by the fabrication limitations of the metal pattern and via-hole arrangement in the sub-terahertz frequency band. The broadband operation achieved by combining techniques was coupled

patch, aperture coupling, and a back-short structure. The proposed transition's principle was investigated through parameter studies conducted via electromagnetic simulations using the finite element method. The transition design has been successful within fabrication limitations in the terahertz band. Simulations of the multi-layer SIW-to-SIW transition showed a reflection coefficient bandwidth of less than −10 dB at 73.8 GHz, with a transmission loss of 0.7 dB at the center frequency of 270 GHz. Performance evaluations of the transition were conducted through both simulations and measurements, with waveguide measurements employed for evaluation. A WG-to-SIW-to-SIW transition with a back-to-back configuration was designed, fabricated, and measured in the sub-terahertz band. The measured results transmission coefficient for a single multi-layer WG-to-SIW-to-SIW transition was −1.8 dB at 270 GHz. Furthermore, the measured result shows a bandwidth of transmission coefficient higher than −3 dB, measuring 57.4 GHz. The measured results revealed a reflection coefficient bandwidth below −10 dB of 64.0 GHz (22.8%), spanning from 248.0 GHz to 312.0 GHz. Especially, the design effectively achieves the fabrication constraints in the sub-terahertz band.

With the proposed techniques, this study has opened up a new research direction for effective transmission systems and RF circuits by exploring novel transmission lines and transition technologies. It focuses on enhancing the bandwidth and performance of multi-layer transitions. Additionally, the work in this thesis investigates the transition of various transmission lines to waveguides, addressing multiple applications. The comprehensive understanding of multi-layer substrate transitions can contribute to special features that enable high transmission performance of millimeter-wave and terahertz-wave systems, thereby reducing costs and enhancing device performance in future communication systems.

Acknowledgment

This thesis could be not completed without the invaluable help from many persons to whom I would like to express my appreciation.

First, I would like to express my deepest gratitude to my supervisor, Prof. Kunio Sakakibara, who led me to the appropriate improvement. I could not have undertaken this journey without his support and kindness. Next, I would like to thank Dr. Yoshiki Sugimoto, who provided me with support and additional comments throughout my doctoral studies journey.

For invaluable comments, I would like to express my gratitude to all committees during my doctoral mid-term and final examination, including Prof. Nobuyoshi Kikuma, from the Department of Electrical and Mechanical Engineering, Nagoya Institute of Technology. Their insightful comments and questions for assessing my work helped improve my dissertation.

I would like to express my exceptional thanks and gratitude to all members of Prof. Sakakibara Laboratory, past or present, for their kind support in my study since I came to Japan. Especially, I would like to express my gratitude to the team members Takafumi Morioka, Makoto Yamazaki, and Bazilah Baharom, and not to forget Dr. Henry Abu Diawuo, and Shumpei Kishi for all their thoughtful support in the lab and life in Japan.

Next, I wish to thank the Rajamangala University of Technology Thanyaburi and Thai Government Scholarship for providing me with a scholarship during the 3 years of the PhD course. I sincerely appreciate your support.

Lastly, I want to express my deepest gratitude to my family and my friend whose belief in my abilities and support. Your encouragement played an integral role in my accomplishments. Thank you for everything. I dedicate this PhD thesis to you.

Chatchai, June 2024.

Publication List

Journal paper:

- **C. Chokchai**, Y. Sugimoto, K. Sakakibara, H. A. Diawuo and N. Kikuma, "Broadband Waveguide-to-Differential-Line Transition in Multi-Layer Substrates With Triple Stacked Patch in 300 GHz Band," in IEEE Access, vol. 12, pp. 49804-49816, 2024, doi: 10.1109/ACCESS.2024.3384606.

- **C. Chokchai**, Y. Sugimoto, K. Sakakibara, M. Yamazaki, H. A. Diawuo and N. Kikuma, "Broadband GCPW-to-Waveguide Transition in Multi-layer Dielectric Substrates with Modified V-shaped and Double Patch in 270 GHz Band," in IEEE Journal of microwave.

International Conference:

- **C. Chokchai,** H. A. Diawuo, Y. Sugimoto, K. Sakakibara and N. Kikuma, "Bandwidth Extension of GSCPW-to-Waveguide Transition in Multi-Layer Dielectric Substrate by Corrugation Structures in THz Band," 2022 International Symposium on Antennas and Propagation (ISAP), Sydney, Australia, 2022, pp. 559-560, doi: 10.1109/ISAP53582.2022.9998582.

- **C. Chokchai**, Y. Sugimoto, K. Sakakibara and N. Kikuma, "Broadband GCPW-to-Waveguide Transition in Multi-Layer Dielectric Substrate with Double Patch and Corrugation Structures in 275 GHz Band," 2023 IEEE International Symposium on Antennas And Propagation (ISAP), Kuala Lumpur, Malaysia, 2023, pp. 1-2, doi: 10.1109/ISAP57493.2023.10389096.

National Conference:

- **C. Chokchai**, M. Yamazaki, H. A. Diawuo, K. Sakakibara, Y. Sugimoto, and N. Kikuma, "Design of GCPW-to-Waveguide Transition in Multi-Layer Dielectric Substrate with Single Patch and Corrugated Structures in 275 GHz Band," IEICE Conferences Archives, 2022.

- M. Yamazaki, H. A. Diawuo, **C. Chokchai**, K. Sakakibara, Y. Sugimoto, and N. Kikuma, "Design of Broadband Differential-Line-to-Waveguide Transition in Multi-layer Dielectric Substrates Exciting X-shaped Patch Element," IEICE Conferences Archives, 2022.

- M. Yamazaki, H. A. Diawuo, **C. Chokchai**, K. Sakakibara, Y. Sugimoto, N. Kikuma, "Design of Broadband Differential-Line-to-Waveguide Transition in Multi-layer Dielectric Substrates Exciting X-shaped Patch Element in 280GHz band," IEICE Technical Report; IEICE Tech. Rep., vol. 121, no. 361, pp. 12-15, 2022.

- M. Yamazaki, H. A. Diawuo, **C. Chokchai**, K. Sakakibara, Y. Sugimoto, N. Kikuma, "Design of Differential Line to Waveguide Transition in Multi-layer Dielectric Substrates Exciting X-shaped Patch Element in 280GHz band," IEICE Technical Report; IEICE Tech. Rep., 2022.

- 榊原　久二男，杉本　義喜，バカル　ロハニ，キム　ジフン，坂本　資子，成田　貴則，バハロム　バジラ，チョックチャイ　チャッチャイ，岸　峻平，杉山　拓矢，土田　偉千，岩本　彩月，山崎　敦也，富山　真帆，菊間　信良，"サブテラヘルツ帯ビーム走査アンテナとその実装技術および課題,"
電子情報通信学会　短距離無線通信研究会　技術報告，SRW-2023-25, pp. 72-77, 2023年7月，新潟大学.

- 榊原　久二男，杉本　義喜，バカル　ロハニ，成田貴則、坂本　資子，バハロム　バジラ，チョックチャイ チャッチャイ，岸 峻平，杉山 拓矢，土田 偉千，岩本 彩月，山崎　敦也，植村　太亮，菊間　信良，"サブテラヘルツ帯におけるアンテナ実装技術とその課題,"電子情報通信学会
アンテナ・伝搬研究会　技術報告, 2023年11月，熊本県労働者福祉会館.